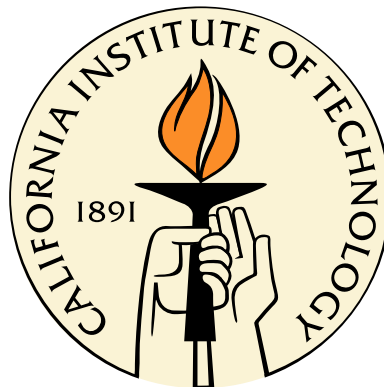# Observation of Cosmic Microwave Background Polarization with BICEP

Thesis by

Hsin Cynthia Chiang

In Partial Fulfillment of the Requirements

for the Degree of

Doctor of Philosophy

California Institute of Technology

Pasadena, California

2009

(Defended September 9, 2008)

For my parents.

Acknowledgments

It has been a pleasure working on BICEP for the past six years, and I thank my advisor, Andrew Lange, for allowing me to join his research group and for providing an intellectually stimulating work environment. To Kathy Deniston, Bryanne Fidler, and Barbara Wertz, thank you all for your organizational support and for keeping us financially worry-free.

This thesis would not have been possible without the efforts of the entire BICEP team and the collective wisdom of local group members. I thank Denis Barkats, Jamie Bock, Brendan Crill, Darren Dowell, Eric Hivon, Bill Jones, John Kovac, Chao-Lin Kuo, Hien Nguyen, Nicolas Ponthieu, and Marcus Runyan for teaching me essentially everything that I know about experimental physics. I am especially indebted to Darren, who has helped me at the times when I needed it the most. I also thank my fellow grad students, Evan Bierman, Justus Brevik, Christian Reichardt, Ian Sullivan (and Crunchy), Yuki "sofa-surfer" Takahashi, Amy Trangsrud, and Kiwon Yoon, for making the grad office a pleasant place to be. BICEP's observing runs would not have been nearly as successful without the help of the South Pole station crew, who are truly a wonderful bunch of people. Special thanks to Steffen Richter for keeping BICEP happy during the past two winters and for good times, guaranteed, on the ice.

I am extremely fortunate to have met JoAnn Boyd, Mike Boyle, Greg Griffin, Ramon van Handel, Ilya Mandel, Jonathan Pritchard, Paige Randall, Ben Rusholme, and Sherry Suyu during my stay at Caltech; thank you for your friendship and for keeping me sane. Words are not enough to thank my family and Luc, who have always given me encouragement and have stayed with me through it all.

Abstract

Background Imaging of Cosmic Extragalactic Polarization (BICEP) is a bolometric polarimeter that has been optimized to target the B-mode of the cosmic microwave background (CMB) polarization at degree angular scales, which is a sensitive probe of the energy scale of inflation. The instrument's focal plane comprises 49 pairs of polarization-sensitive bolometers operating at 100 and 150 GHz, and the 25-cm aperture refractive optics provide degree-scale resolution over a $17°$ instantaneous field of view. The compact design enables sufficient control of instrumental polarization systematics to attain a projected final sensitivity corresponding to a tensor-to-scalar ratio of 0.1. This thesis describes the design, performance, and preliminary science results from BICEP, which has been observing the CMB from the South Pole since January 2006. After the first two seasons of operation, the EE, TE, and TT power spectra are measured with high precision at $30 < \ell < 300$, and BB is consistent with zero. BICEP has also observed the Galactic plane, and polarized emission is mapped with high signal-to-noise.

The BICEP collaboration

California Institute of Technology D. Barkats, H. C. Chiang, G. S. Griffin, V. V. Hristov, W. C. Jones, J. M. Kovac, A. E. Lange, P. V. Mason, T. Matsumura, S. Richter, G. M. Rocha

Jet Propulsion Laboratory J. O. Battle, J. J. Bock, C. D. Dowell, E. M. Leitch, H. T. Nguyen

University of California, Berkeley W. L. Holzapfel, Y. D. Takahashi

University of California, San Diego E. M. Bierman, B. G. Keating

University of Chicago C. Pryke, C. Sheehy

NIST, Boulder K. W. Yoon

Stanford University C. L. Kuo

Institut d'Astrophysique de Paris E. F. Hivon

Institut d'Astrophysique Spatiale, Orsay N. Ponthieu

Cardiff University P. A. Ade

CEA Grenoble L. Duband

Contents

List of Figures

List of Tables

Chapter 1

Introduction and background

1.1 Probing the early universe with the CMB

Cosmology, the study of the origins, evolution, and large-scale structure of the universe, has rapidly evolved from speculation to a precision science. An impressive collection of observational evidence now supports the Big Bang model and the history of the universe, as outlined in Figure 1.1. One of the cornerstones in our current understanding of cosmology is the theory of inflation—accelerated expansion of the universe that took place 10^{-35} s after the Big Bang. Inflation has enjoyed the success of solving several major shortcomings of the standard Big Bang model, namely the flatness and horizon problems; however, the theory has yet to be confirmed by any direct observational evidence.

Fortunately, the universe has given cosmologists a remarkable tool to shed light on its beginnings. The cosmic microwave background (CMB) is the "afterglow" of the Big Bang and is thus a direct snapshot of the universe in its infancy. Cosmology has been revolutionized by precision measurements of the CMB over the past 40 years—after the initial detection in 1965, the sensitivity of experiments has followed a Moore's Law trend so that, today, it is standard to measure CMB temperature fluctuations of one part in 100,000. Recently, the WMAP satellite mapped the CMB temperature fluctuations over the entire sky (Figure 1.2), and the combined temperature power spectrum from WMAP [1], BOOMERANG [2], CBI [3], and ACBAR [4] data shows resolved peak structure up to $\ell \sim 1600$.
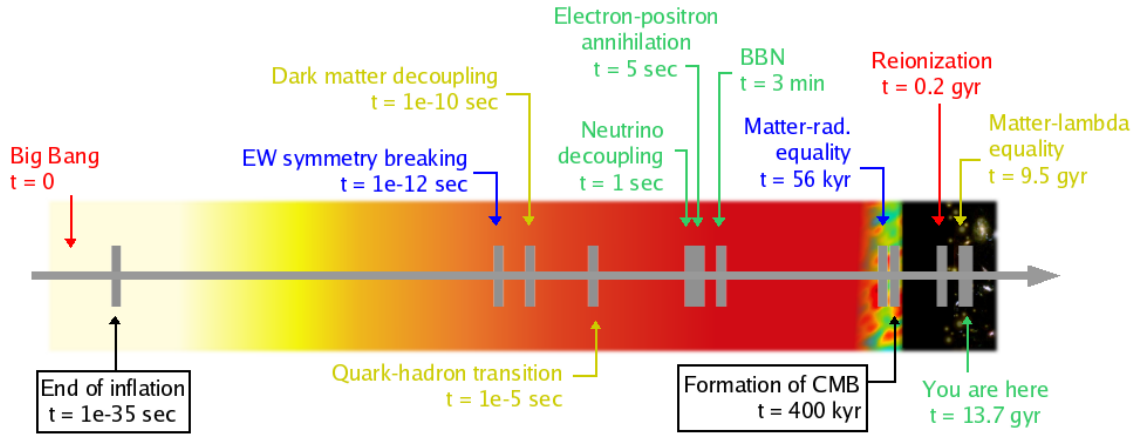
Figure 1.1: An abbreviated history of the universe (to scale on a logarithmic axis). Shortly after the Big Bang, it is believed that the universe experienced a brief period of accelerated expansion, known as inflation. Although the exact physics of the early universe is unknown until electroweak symmetry breaking at $t = 10^{-12}$ s, one of the robust predictions of inflationary theory is the presence of a stochastic gravitational wave background. As the universe expanded and cooled, various forces and particles decoupled until, finally, matter and radiation separated, forming the cosmic microwave background that is visible today. This last scattering surface at $t = 400$ kyr is the limit of direct observations. However, by examining the faint polarized signal that the gravitational wave background imprints on the CMB, it is possible to look (indirectly) beyond the surface of last scattering to even earlier times in the universe's history.

(a)

(b)
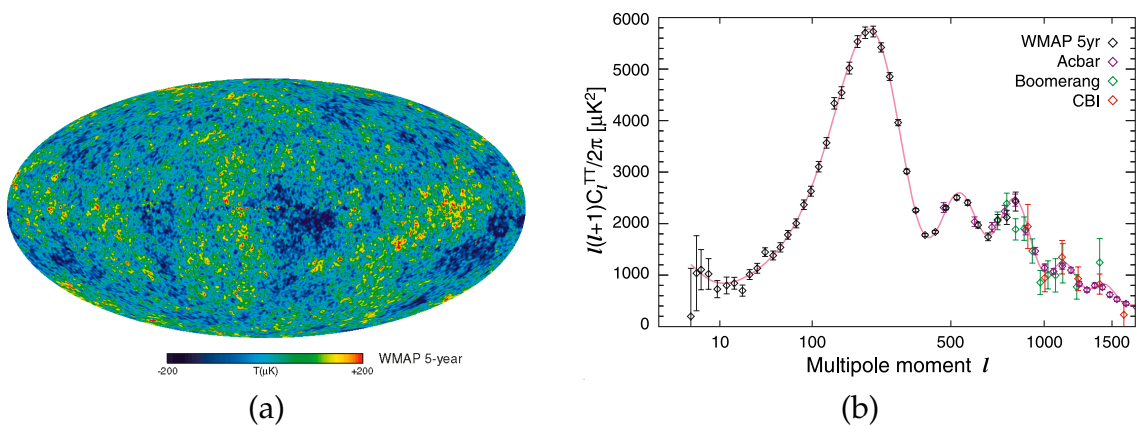
Figure 1.2: The CMB temperature anisotropies have been measured over the entire sky by WMAP (a). The combined temperature power spectrum (b) from WMAP, BOOMERANG, CBI, and ACBAR shows resolved peak structure up to $\ell \sim 1600$. Figures courtesy of the WMAP science team [1; 5].

Experiments are now actively pursuing the CMB *polarization* anisotropies, which encode information about the universe's history long before the moment of matter–radiation decoupling. The polarization of the CMB arises from two cosmological sources. First, the CMB is intrinsically polarized at the few-percent level due to scattering processes that are correlated with the underlying temperature fluctuations. The resulting polarization, which has no handedness, is known as the "gradient" or "E-mode," in analogy to curl-free electric fields. The E-mode polarization was first detected in 2002 by the DASI telescope [6] and has since been measured by several other experiments [7–11], thus confirming our basic understanding of CMB physics. The second, more exotic, source of CMB polarization is a gravitational wave background, the existence of which is a robust prediction of inflation models. Gravitational waves impart a unique imprint on the CMB by introducing a curl or "B-mode" to the polarization field. The elusive B-mode, which is currently undetected, is expected to have an amplitude that is at least 100 times smaller than that of the CMB temperature anisotropies. Measuring the weak polarized signal presents a formidable challenge to experimentalists; however, the detection of the B-mode would be the first definitive piece of evidence confirming inflationary theory and would truly solidify the modern cosmological paradigm.

1.2 Cosmology in a nutshell

The purpose of this section is to highlight the physics of the early universe that generates the CMB temperature and polarization fluctuations that we observe today. References [12], [13], and Sterl Phinney's lecture notes have been invaluable resources for compiling this brief review.

1.2.1 Dynamics of the universe

Modern cosmology is based on the assumption that the universe is spatially homogeneous and isotropic to all observers (the "cosmological principle"). Early

cosmological theories also extended this Copernican idea to the time dimension and modeled the universe as a steady-state system. However, in 1929, Edwin Hubble presented observational evidence showing that galaxies in all directions appear to be receding and that, furthermore, the recession velocity is proportional to the distance of the galaxy. The distance-velocity relation is a natural consequence of a metric whose spatial components are uniformly expanding. As a result, Hubble's discovery sparked a global shift away from steady-state theories, and cosmologists adopted the expanding universe model that is still used today. From the assumptions of homogeneity and isotropy alone, along with the observation of the universe's expansion, the line element

$$ds^2 = -c^2 dt^2 + a^2(t) \left(\frac{dr^2}{1 - Kr^2} + r^2 d\theta^2 + r^2 \sin^2 \theta d\phi^2 \right) \tag{1.1}$$

uniquely follows. In this expression, which is known as the Friedmann–Robertson–Walker (FRW) metric, K is a constant that describes the curvature of the universe, and $a(t)$ is the scale factor, which evolves as a function of time. The matter and energy in the universe are coupled to its geometry through the Einstein field equations $G_{\mu\nu} = 8\pi G T_{\mu\nu}$, where $G_{\mu\nu} \equiv R_{\mu\nu} - g_{\mu\nu} R/2$. In the case of the FRW metric, $G_{\mu\nu}$ vanishes except for its diagonal elements, of which the spatial components $\mu, \nu \in \{1, 2, 3\}$ are identical. If we treat the universe's constituents as a perfect, isotropic fluid, then the off-diagonal elements of the stress-energy tensor $T_{\mu\nu}$ also vanish, and the time and spatial components are simply the energy density $-\rho c^2$ and pressure P, respectively. The time and spatial components of $G_{\mu\nu}$ and $T_{\mu\nu}$ yield two equations

$$\frac{8\pi G}{3} \rho + \frac{Kc^2}{a^2} = \left(\frac{1}{a} \frac{da}{dt} \right)^2 \tag{1.2}$$

$$-\frac{8\pi G}{c^2} P + \frac{Kc^2}{a^2} = \left(\frac{1}{a} \frac{da}{dt} \right)^2 + \frac{2}{a} \frac{d^2 a}{dt^2} \tag{1.3}$$

that can be combined to form

$$\frac{1}{a}\frac{d^2a}{dt^2} = -\frac{4\pi G}{3}\left(\rho + \frac{3P}{c^2}\right),$$ (1.4)

which describes the time evolution of the scale factor. The exact dynamics depend on the constituents of the universe, each of which is described by an equation of state $P = w\rho c^2$. From the statement of energy conservation, $\nabla_\mu T^\mu_\nu = 0$ or $d(\rho c^2 a^3)/dt = -P d(a^3)/dt$ for a perfect fluid, we obtain $\rho \propto a^{-3(1+w)}$. Matter (both baryonic and dark) has $w \approx 0$, so the density scales as a^{-3}. Relativistic particles like photons and neutrinos, on the other hand, have $w = 1/3$, and the density scales as a^{-4}. It is useful to recast Equation 1.2 into the form

$$\frac{H^2(t)}{H_0^2} = \Omega_m\left(\frac{a_0}{a(t)}\right)^3 + \Omega_r\left(\frac{a_0}{a(t)}\right)^4 + \Omega_K\left(\frac{a_0}{a(t)}\right)^2 + \Omega_\Lambda\left(\frac{a_0}{a(t)}\right)^{3(1+w_\Lambda)},$$ (1.5)

where the right-hand side has been separated into different components according to their w parameters. Here $H(t) \equiv (da/dt)/a$, and Ω denotes the present-day density of each component expressed as a fraction of of the critical density

$$\rho_c \equiv \frac{3H_0^2}{8\pi G}.$$ (1.6)

The subscripts m and r correspond to matter and radiation, and K is the curvature of the universe. The Λ denotes a mysterious component, sometimes called "dark energy," and appears in the equation because of recent observational evidence that suggests that the universe is not only expanding, but also that the expansion rate is *increasing*. Although Λ is currently just a name that we assign to a phenomenon that is not understood at all, we can still give it an equation of state; the condition for acceleration is then $-1 < w_\Lambda < -1/3$. Current evidence favors an uncomfortably high dark energy density, $\Omega_\Lambda \sim 0.7$, and numerous research efforts are being made towards understanding this large component of the universe's energy budget.

Given values of Ω_m, Ω_r, Ω_K, and Ω_Λ, Equation 1.5 can be used to calculate the

evolution of each component. Each density scales differently with a, so different components dominate the universe at various epochs. The universe's timeline is often described in terms of redshift z, which is defined as $1 + z = a_0/a$. Using Ω parameters that are the current fashion in cosmology, we find that radiation dominates at early times, $z > 3300$. Matter dominates afterwards, $0.4 < z < 3300$, and Λ has just recently ($z < 0.4$) taken over. The universe was hot and dense at early times, and as it expanded and cooled, interacting particles fell out of thermal equilibrium as the temperature dropped below the energy scale of the reactions. In the case of recombination, electrons and protons were coupled through Coulomb scattering, and electrons and photons were coupled through Compton scattering. Recombination occurred at an energy scale of approximately 1 eV ($z \sim 1100$), which is somewhat lower than the characteristic 13.7-eV binding energy of hydrogen. The reason for this decreased energy scale is that the photons outnumber the baryons by a factor of $\sim 10^9$, and neutral hydrogen is therefore instantly ionized by the small fraction of photons in the high-energy tail of the blackbody spectrum. Because electron-proton recombination to the ground state emits an ionizing photon, the most relevant reaction is recombination to an excited state that then decays via two-photon emission. Recombination occurs in a narrow window of about $\Delta z = 100$, and the photons from the "last scattering surface" make up the CMB that we observe today.

1.2.2 Inflation

The standard Big Bang model has three main shortcomings, which are often called the flatness, horizon, and monopole problems. The flatness problem is apparent from Equation 1.2, which can be rewritten as

$$\Omega(t) - 1 = \frac{c^2 K}{H^2(t)a^2(t)}. \tag{1.7}$$

Here $\Omega(t) = \rho(t)/\rho_c(t)$, the total density of the universe's constituents. In the radiation-dominated era, $H^2 \propto a^{-4}$, so the right-hand side of Equation 1.7 scales

as a^2; in the matter-dominated era, the right-hand side scales as a. Therefore, small deviations from flatness grow quickly with time. The present-day value of $|\Omega - 1|$ is measured to be less than 0.02, which means that the density parameter must be fine-tuned at early times in order to remain so small. For example, extrapolating back to $\sim 10^{-35}$ s after the Big Bang, the typical energy scale for grand unified theories (GUTs), $|\Omega - 1|$ would need to be less than 10^{-51}. Any small deviation from this number would have resulted in the universe experiencing a "big crunch" or a "big rip" shortly after the Big Bang. This instability of a nearly flat universe is sometimes called the age problem—how did our universe grow to be so old?

The horizon problem arises from the homogeneity of the universe on large angular scales. A prime example is the temperature of the CMB, which is uniform to about one part in 10^5 over the entire sky. The horizon size at the surface of last scattering is about $2°$, so areas with greater separation had no causal contact and therefore had no reason to arrive at the same temperature. Furthermore, after last scattering, the CMB photons free-stream and have virtually no interactions with each other, so there is no mechanism for their temperatures to equilibrate. The lack of an explanation for the uniformity in CMB temperature is a severe problem in the standard Big Bang model.

The monopole problem comes from the GUT prediction that as the universe cools and passes through the GUT energy scale, the phase transition gives rise to topological defects in the form of magnetic monopoles. About one defect is expected per horizon volume, so the universe should be overflowing with monopoles today. However, a magnetic monopole has yet to be detected, so we are left wondering where they all went.

The theory of inflation was developed as a patch for these holes in the standard Big Bang model, and the proposed solution is exponential growth of the scale factor at GUT energy scales. The hypothesis is that for a brief period around $t \sim 10^{-35}$ s, the universe was dominated by some sort of cosmological constant that caused accelerated expansion. Note that this particular cosmological constant is unlikely to be related to the Λ that is causing accelerated expansion today. At the

GUT time, the particle horizon size was $\sim 10^{-24}$ cm. The particle horizon today is about 4×10^{28} cm, which extrapolates back to ~ 10 cm at the GUT time. Inflation boosts the horizon size by a factor of at least 10^{25}, or 60 e-folds, which instantly resolves the horizon problem because the entire last scattering surface would have been in causal contact prior to inflation. Along similar lines, the monopole problem is also solved because the number density is diluted during the accelerated expansion so that, today, we should expect the presence of at most one monopole in the entire visible universe. If the universe is briefly dominated by a cosmological constant with $-1 < w < -1/3$, then $a \propto t^{2/(3+3w)}$ and $H \propto t^{-1}$ during that period. Substituting these relations into Equation 1.7, we find that

$$|\Omega(t) - 1| \propto t^{2(1+3w)/(3+3w)}, \tag{1.8}$$

so deviations from flatness are highly suppressed. Inflation therefore solves the flatness, monopole, and horizon problems at the same time.

Although inflation appears to be a somewhat contrived solution, it is relatively easy to achieve accelerated expansion by invoking a scalar "inflaton" field that briefly dominates the energy content of the universe. (Particle physicists invent scalar fields regularly, so grant cosmologists this one liberty.) Unfortunately, the catch is that scalar fields and their associated particles have never been observed, and the most familiar candidate, the Higgs, has been ruled out as a possible driver of inflation. Nevertheless, we proceed forwards and leave the interpretation of the scalar field as an open problem for the time being. From the stress-energy tensor of a homogeneous scalar field $\phi(t)$, the energy density and pressure are

$$\rho c^2 = \frac{1}{2}\left(\frac{d\phi}{dt}\right)^2 + V(\phi) \tag{1.9}$$

$$P = \frac{1}{2}\left(\frac{d\phi}{dt}\right)^2 - V(\phi), \tag{1.10}$$

where $V(\phi)$ is the potential energy. The condition for acceleration is negative pres-

sure ($-1 < w < -1/3$), which occurs[1] if the field "slowly rolls" with a small amount of kinetic energy down a shallow potential. Slow roll inflation is typically quantified with the parameters

$$\epsilon \equiv \frac{d}{dt}\left(\frac{1}{H}\right) = -\frac{1}{aH^2}\frac{dH}{d\eta} \tag{1.11}$$

and

$$\begin{aligned}
\delta &\equiv \frac{1}{H}\frac{d^2\phi/dt^2}{d\phi/dt} \\
&= -\frac{1}{aH d\phi/d\eta}\left[3aH\frac{d\phi}{d\eta} + a^2\frac{dV}{d\phi}\right],
\end{aligned} \tag{1.12}$$

where η is the conformal time

$$\eta \equiv \int_0^t \frac{dt'}{a(t')}. \tag{1.13}$$

The parameters ϵ and δ describe how slowly the field evolves towards the potential minimum and are much less than unity in most models of inflation.

1.2.3 Metric perturbations

Theorists are creative and have invented a myriad of ways to implement inflation. Given the abundant creativity of our theorist friends, we experimentalists must identify generic, robust, and testable predictions of inflation. As in a game of James Brown bingo, we have already marked off the middle square for free: inflation solves the horizon, flatness, and monopole problems. Fortunately, that's not all. Inflation also predicts that quantum mechanical fluctuations perturb the FRW metric and, through the Einstein field equations, create small levels of inhomogeneity and anisotropy that are visible today. By the decomposition theorem, perturbations to the metric can be separated into scalar, vector, and tensor components that evolve independently of each other.

---

[1]The pressure can also be negative if ϕ is trapped in a false vacuum where the potential energy is greater than the kinetic energy. However, this scenario has been ruled out.

First-order scalar perturbations to the metric take the form of

$$
\begin{pmatrix}
-2\Psi & 0 & 0 & 0 \\
0 & 2a^2\Phi & 0 & 0 \\
0 & 0 & 2a^2\Phi & 0 \\
0 & 0 & 0 & 2a^2\Phi
\end{pmatrix},
\tag{1.14}
$$

where Ψ and Φ are perturbations to the gravitational potential and spatial curvature, respectively, and both are functions of time and position. We are interested in expressing Ψ and Φ in terms of fluctuations $\delta\phi(\vec{x}, t)$ of the inflaton field about its zeroth-order homogeneous part: $\phi(\vec{x}, t) = \phi^{(0)}(t) + \delta\phi(\vec{x}, t)$. These fluctuations are created at early times and are pushed outside the horizon during inflation. Upon re-entry of the horizon after inflation, the perturbations source density fluctuations that evolve into the present-day large-scale structure of the universe. The perturbations are described by power spectra as a function of wave number k, and it is common to assume that the power spectrum amplitude of Ψ and Φ are the same. The end result is the nearly scale-invariant spectrum

$$
\begin{aligned}
P_\Psi(k) = P_\Phi(k) \ \ &= \ \ \frac{8\pi G}{9k^3} \left. \frac{H^2}{\epsilon} \right|_{aH=k} \tag{1.15} \\
&\equiv \ \ \frac{50\pi^2}{9k^3} \left(\frac{k}{H_0}\right)^{n_s - 1} \delta_H^2 \left(\frac{\Omega_m}{D_1(a=1)}\right)^2, \tag{1.16}
\end{aligned}
$$

where δ_H is the scalar amplitude at the horizon crossing and D_1 is the growth function. Scale invariance is not a unique prediction of inflation, but a measured deviation of the scalar spectral index n_s from unity would constrain inflation models via the relationship of n_s to the slow roll parameters,

$$
n_s = 1 - 4\epsilon - 2\delta. \tag{1.17}
$$

Vector perturbations can be expressed in terms of two functions in the spatial components of the metric, and these functions describe the evolution of vorticity

in the universe,

$$
\begin{pmatrix}
0 & 0 & 0 & 0 \\
0 & 0 & 0 & a^2 h_{xz} \\
0 & 0 & 0 & a^2 h_{yz} \\
0 & a^2 h_{xz} & a^2 h_{yz} & 0
\end{pmatrix}.
\tag{1.18}
$$

Unlike scalar and tensor perturbations, vector perturbations are not commonly predicted by inflation models, although they do appear in some theories based on topological defects. In addition, because of angular momentum conservation, vector perturbations tend to decay quickly with time; the rotation rate decreases as the universe expands. For these reasons, experimentalists generally ignore vector perturbations.

Tensor perturbations to the metric can be written as

$$
\begin{pmatrix}
0 & 0 & 0 & 0 \\
0 & a^2 h_+ & a^2 h_\times & 0 \\
0 & a^2 h_\times & -a^2 h_+ & 0 \\
0 & 0 & 0 & 0
\end{pmatrix},
\tag{1.19}
$$

where h_+ and $h_\times$ are the two components of a traceless and symmetric tensor describing gravitational waves. These perturbations do not couple to density fluctuations, but they do induce fluctuations in the CMB and are uniquely predicted by inflation. It can be shown that h_+ and $h_\times$ satisfy the wave equation

$$
\frac{d^2 h}{d\eta^2} + \frac{2}{a} \frac{da}{d\eta} \frac{dh}{d\eta} + k^2 h = 0,
\tag{1.20}
$$

where the middle damping term describes the decay of gravitational waves as the universe expands. Large-scale modes remain constant until the horizon size is comparable to the wavelength, and modes that are smaller than the horizon size rapidly drop in amplitude. If Equation 1.20 is rewritten in the form of a harmonic oscillator and h is quantized, then the power spectrum of the primordial tensor

perturbations is

$$P_h(k) = \left.\frac{8\pi G H^2}{k^3}\right|_{aH=k} \tag{1.21}$$

$$\equiv A_T k^{n_T-3}, \tag{1.22}$$

where A_T is the tensor amplitude. Rather than using A_T directly, it is more common to quote the ratio r (or T/S) of the tensor and scalar primordial power spectra at a pivot point $k = 0.002\,\mathrm{Mpc}^{-1}$. The tensor spectral index n_T describes the deviation from scale invariance and can be expressed as

$$n_T = -2\epsilon. \tag{1.23}$$

The tensor amplitude is a powerful test of inflation because $H^2 \propto \rho/m_{pl}^2$, and therefore $P_h(k) \propto \rho/m_{pl}^4$, where m_{pl} is the Planck mass. In slow roll inflation, $V(\phi)$ dominates the energy density, so a detection of $P_h(k)$ would also be a direct measurement of the energy scale of inflation. Considering that typical inflation models operate at 10^{15} GeV or greater, the possibility of probing these energy scales is exciting, to say the least—the largest particle accelerators achieve energies of $\sim 10^3$ GeV, which is 12 orders of magnitude lower!

1.2.4 Particle distributions

Given the perturbations to the FRW metric, the next task is to calculate the corresponding perturbations to particle distributions, which come from applying the Boltzmann equation to the relevant particle species. We are primarily interested in photons, neutrinos, dark matter, and baryonic[2] matter, which couple to scalar perturbations in the metric (Equation 1.14). The Boltzmann equation states that the time derivative of a particle distribution function is equal to the sum of all possible collision terms, and it is a method of describing the complex couplings between

---

[2]Cosmologists classify both protons and electrons as "baryons," which is a blatant misuse of terminology.

particle distributions, particle interactions, and the metric.

Photons are described by the Bose-Einstein distribution, and the first-order perturbation to this distribution is expressed in terms of $\Theta(\vec{x}, \hat{p}, t) = \delta T / T$, the fluctuation of the temperature about its zero-order value. Photons are coupled to electrons through Compton scattering, which has a cross-section that depends on the angle and polarization of the incoming and outgoing photon. In the linear regime, when the perturbations are small, each Fourier mode with wave number k evolves independently, and the Boltzmann equation can be written as

$$\dot{\tilde{\Theta}} + ik\mu\tilde{\Theta} = -\dot{\tilde{\Phi}} - ik\mu\tilde{\Psi} - \dot{\tau}\left[\tilde{\Theta}_0 - \tilde{\Theta} + \mu v_b - \frac{1}{2}\mathcal{P}_2(\mu)\tilde{\Pi}\right]. \tag{1.24}$$

The overdot denotes a derivative with respect to conformal time, tilde denotes the Fourier transform, μ is the photon propagation direction $\hat{k} \cdot \hat{p}$, $\tilde{\Theta}_0$ is the monopole moment of $\tilde{\Theta}$, v_b is the electron velocity, $\mathcal{P}_2$ is the second Legendre polynomial, and τ is the optical depth, the time derivative of which is proportional to the electron density and the Thomson cross-section. The temperature and polarization coupling $\tilde{\Pi}$ is defined as

$$\tilde{\Pi} = \tilde{\Theta}_2 + \tilde{\Theta}_{P2} + \tilde{\Theta}_{P0}. \tag{1.25}$$

The polarization strength $\tilde{\Theta}_P$ obeys the equation

$$\dot{\tilde{\Theta}}_P + ik\mu\tilde{\Theta}_P = -\dot{\tau}\left[-\tilde{\Theta}_P + \frac{1}{2}(1 - \mathcal{P}_2(\mu))\tilde{\Pi}\right] \tag{1.26}$$

and is sourced by only the quadrupole moment $\tilde{\Theta}_2$ of the temperature field. Like photons, neutrinos are relativistic particles and are governed by a similar evolution equation:

$$\dot{\tilde{\mathcal{N}}} + ik\mu\tilde{\mathcal{N}} = -\dot{\tilde{\Phi}} - ik\mu\tilde{\Psi}. \tag{1.27}$$

Here $\mathcal{N}$ is the fractional fluctuation of the neutrino temperature, and the neutrinos are assumed to be massless.

The Boltzmann equation for cold dark matter yields two evolution equations

$$\dot{\tilde{\delta}} + ik\tilde{v} = -3\dot{\tilde{\Phi}} \tag{1.28}$$

$$\dot{\tilde{v}} + \frac{\dot{a}}{a}\tilde{v} = -ik\tilde{\Psi}, \tag{1.29}$$

where δ is fractional overdensity and v is the velocity. Note that there are no collision terms because dark matter does not interact with any other particles. The electrons and protons that comprise baryonic matter are tightly coupled by Coulomb scattering at all epochs, so the fractional densities arrive at the same value δ_b (and the same is true for the velocity v_b). The evolution equations for baryonic matter are

$$\dot{\tilde{\delta}}_b + ik\tilde{v}_b = -3\dot{\tilde{\Phi}} \tag{1.30}$$

$$\dot{\tilde{v}}_b + \frac{\dot{a}}{a}\tilde{v}_b = -ik\tilde{\Psi} + \dot{\tau}\frac{4\rho_\gamma}{3\rho_b}[\tilde{v}_b + 3i\tilde{\Theta}_1] \tag{1.31}$$

and are the same as the dark matter case except for two extra terms in the velocity equation. The photon-to-baryon ratio is ρ_γ/ρ_b, and $\tilde{\Theta}_1$ is the first moment of the temperature field.

Perturbations in the particle distributions affect the gravitational field and feed back into the metric. By expanding the Einstein field equation about the zero-order solution, we obtain two more evolution equations that relate the metric perturbations to matter and radiation fluctuations:

$$k^2\tilde{\Phi} + 3\frac{\dot{a}}{a}\left(\dot{\tilde{\Phi}} - \tilde{\Psi}\frac{\dot{a}}{a}\right) = 4\pi Ga^2[\rho_m\tilde{\delta}_m + 4\rho_r\tilde{\Theta}_{r,0}] \tag{1.32}$$

$$k^2(\tilde{\Phi} + \tilde{\Psi}) = -32\pi Ga^2\rho_r\tilde{\Theta}_{r,2}. \tag{1.33}$$

Here the subscript m includes both baryonic and dark matter, and the subscript r includes photons and neutrinos.

The set of Equations 1.24–1.33 provide a complete description of the nine perturbation variables that affect matter and radiation fluctuations. Tensor pertur-

bations to the metric do not couple to density fluctuations, but they create gravitational waves described by Equation 1.20. The initial conditions for matter and radiation can be reduced to

$$\tilde{\delta} = 3\tilde{\Theta}_0 + \text{constant} \tag{1.34}$$

for both dark and baryonic matter. It is common to choose adiabatic initial conditions, where the additive constant is zero and the matter-to-radiation ratio is constant everywhere. (The other scenario, with a non-zero constant, is called isocurvature perturbations.) Given initial conditions, the evolution equations can be solved numerically with codes such as CMBFAST [14] or CAMB [15].

1.2.5 From primordial to present-day spectra

We would like to understand the evolution of the photon perturbations that result in the present-day CMB anisotropies. Solving the Boltzmann equations is a hairy task, but some analytical insight can be gained by examining different length scales separately. Photons and baryons are tightly coupled as a single "photon–baryon fluid" before and during recombination, and the behavior of the fluid can be characterized on three length scales: (1) large scales that are greater than the horizon size, (2) scales within the horizon, and (3) the smallest scales defined by the photon diffusion length. After decoupling, the photons free-stream with essentially no interactions, so if we understand the photon fluctuations at the moment of decoupling, then we basically understand the present-day fluctuations of the CMB.

On the largest scales at recombination, the Boltzmann equations reduce to the following two expressions for the observed anisotropies:

$$(\tilde{\Theta}_0 + \tilde{\Psi})(k, \eta_{\text{rec}}) = \frac{1}{3}\tilde{\Psi}(k, \eta_{\text{rec}}) \tag{1.35}$$

$$(\tilde{\Theta}_0 + \tilde{\Psi})(k, \eta_{\text{rec}}) = -\frac{1}{6}\tilde{\delta}(\eta_{\text{rec}}). \tag{1.36}$$

The effective temperature is the sum $\tilde{\Theta}_0 + \tilde{\Psi}$ in order to account for the redshifting

of photons as they move out of gravitational potential wells. According to Equation 1.36, the effective temperature fluctuates downwards for matter overdensities and upwards for underdensities. The reason for this surprising result is that although overdense regions contain hotter photons at recombination, the photons lose energy while climbing out of the potential wells, and the energy loss overcompensates for the initial energy excess. The large-scale modes are unaffected by causal physics and thus directly probe the primordial perturbations generated by inflation. The portion of the CMB temperature power spectrum at these scales is called the Sachs-Wolfe plateau and is approximately flat.

At scales within the horizon, fluctuations in the photon–baryon fluid are influenced by two competing forces: gravitational attraction causes overdense regions to collapse, but radiation pressure pushes in the opposite direction. The Boltzmann equations reduce to an expression for a driven, damped harmonic oscillator

$$\left[\frac{d^2}{d\eta^2} + \frac{\dot{R}}{1+R}\frac{d}{d\eta} + k^2 c_s^2 \right] (\tilde{\Theta}_0 + \tilde{\Phi}) = \frac{k^2}{3} \left(\frac{1}{1+R}\tilde{\Phi} - \tilde{\Psi} \right), \qquad (1.37)$$

where R is the baryon-to-photon ratio $(3\rho_b)/(4\rho_\gamma)$ and $c_s = 1/\sqrt{3(1+R)}$ is the sound speed in the fluid. In practice, the damping term is much smaller than the radiation pressure term and can be ignored to obtain an approximate solution. The photon perturbations oscillate as a function of $k\eta_{\rm rec}$, producing the characteristic peaks and troughs that we measure in the temperature power spectrum today (Figure 1.2). The first peak corresponds to the largest mode that enters the horizon and reaches a compression maximum at the time of recombination. At these scales, the density contrast across the surface of last scattering is high, so the power spectrum is also maximized. The subsequent peaks and troughs correspond to smaller modes that have gone through more oscillation cycles. The acoustic oscillations are also sensitive to the baryon density in two different ways. First, as the baryon density increases, the sound speed decreases; therefore, the oscillation frequency decreases and the spacing between the peaks grows. Second, the height difference between odd-numbered and even-numbered peaks increases because the former

correspond to maximally compressed regions, which collapse even farther if the baryon density is high. The even-numbered peaks correspond to regions of maximum rarefaction, which are less underdense if the gravitational force is increased with respect to the radiation pressure.

After recombination, the photon fluctuations are slightly modified by the integrated Sachs-Wolfe (ISW) effect, which is a term in the power spectrum expression that depends on the time derivative of the gravitational potentials. The early ISW effect, which occurs because of residual radiation that is present at recombination, results in excess power at the horizon scale. The height of the first power spectrum peak is therefore enhanced above the others. At later times, when Λ begins to dominate the universe, the temperature power spectrum is also enhanced by the ISW effect at the very largest scales.

At the smallest scales during recombination, the acoustic oscillations are washed away by photon diffusion. The photon mean free path is $1/(n_e \sigma_T)$, where n_e is the electron density and σ_T is the Thomson cross-section, so the average distance that a photon travels in a Hubble time is approximately $1/\sqrt{n_e \sigma_T H}$. Photon perturbations smaller than the diffusion scale are quickly damped out (this process is known as Silk damping). In addition, the diffusion length depends on n_e, so the baryon density determines the angular scale at which damping effects begin to dominate.

1.2.6 Polarization

The equations describing photon fluctuations at the surface of last scattering primarily result in temperature anisotropies, which have been well studied and characterized. However, Equation 1.24 also contains a polarization-dependent term that has become the subject of one of the most active areas of CMB research today. The polarization of the CMB arises from Thomson scattering of photons off electrons surrounded by a local quadrupole moment in intensity, as illustrated in Figure 1.3. Although the incident radiation on the electron is unpolarized, the light
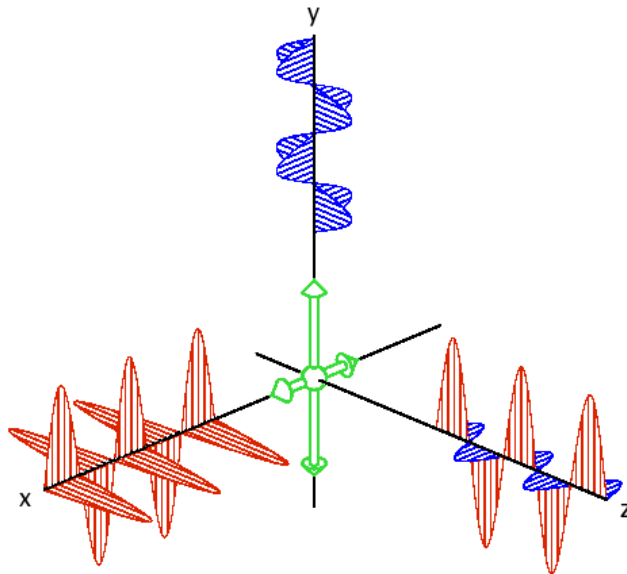
Figure 1.3: The CMB is polarized by Thomson scattering of photons off electrons surrounded by a quadrupole moment in intensity. In this picture, x and y correspond to hot and cold spots that emit unpolarized radiation. The (green) electron in the center scatters some of the radiation in the z direction towards the observer, who sees a small degree of polarization. This figure is adapted from reference [16].

that is scattered to the observer is slightly polarized. A quantitative description of the polarization anisotropies comes from solving the Boltzmann equations, but once again, we can gain some qualitative insight by examining simple cases.

Temperature fluctuations cause photons to flow from hot to cold regions, and these velocity gradients are the source of quadrupole moments in the frame of an electron scatterer. Only the quadrupole moment generates polarization, and it is suppressed by the high Thomson scattering rate until the final stages of recombination; these combined restrictions result in a polarization power spectrum amplitude that is greatly suppressed with respect to the temperature spectrum. For a single plane wave in density propagating perpendicular to the line of sight (Figure 1.4), the polarization directions in the cold troughs and hot peaks are perpendicular and parallel to the wave vector, respectively. A superposition of these plane waves yields polarization patterns that are radial around cold spots and cir-
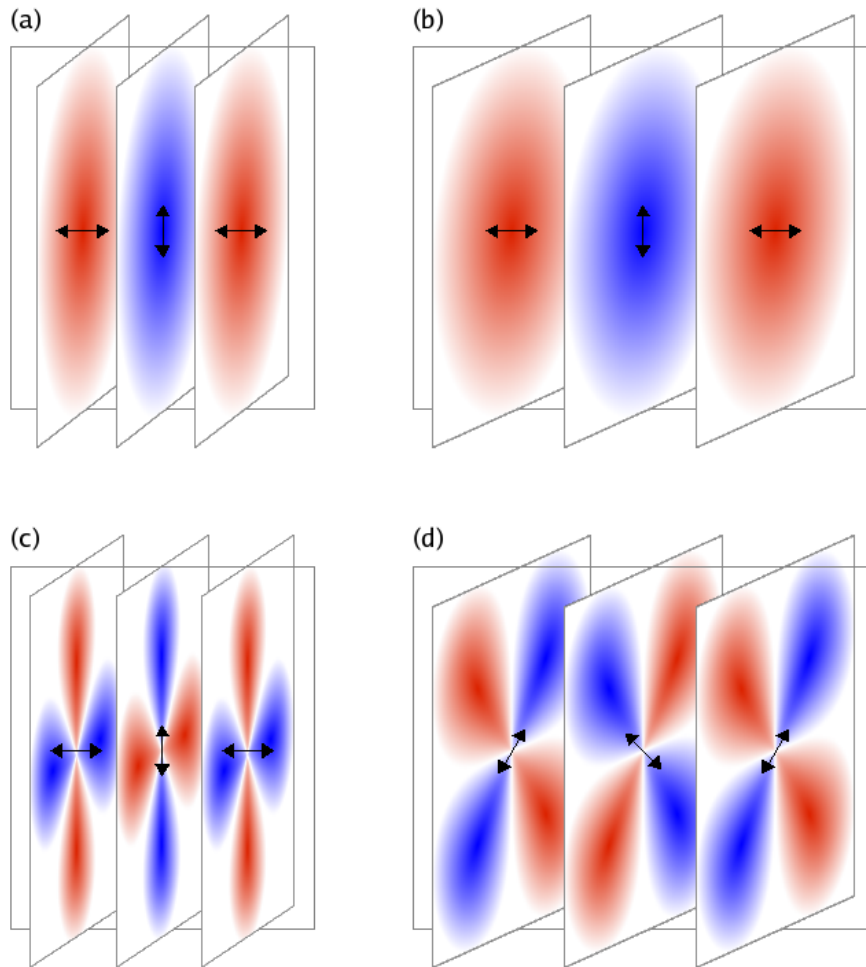
Figure 1.4: In panels (a) and (b), a density wave propagates at a zero and non-zero angle with respect to the plane of the page. Red and blue correspond to hot and cold regions, respectively. An electron sitting in a cold trough sees a quadrupole moment consisting of hot spots on either side and cold spots above and below. The polarized emission is therefore in the vertical direction, and by similar arguments, the hot crests emit horizontally polarized light. Regardless of the propagation angle, polarization from density waves always follows an E-mode pattern. In panels (c) and (d), a "plus" and "cross" gravitational wave propagate at two different angles. A quadrupole moment is generated in each crest and trough because the metric stretches and compresses. In these particular examples, (c) creates an E-mode pattern, while (d) creates a B-mode pattern. This figure is adapted from reference [17].

cular around hot spots. Like electric fields, the polarization patterns created by scalar perturbations have zero curl and are thus called E-modes. Figure 1.4 shows a cartoon illustration of how density perturbations create E-mode patterns, and a more detailed discussion is available in reference [18].

Gravitational waves from tensor perturbations to the metric also generate local quadrupole moments and leave a polarization imprint on the CMB. Unlike density waves, which are rotationally symmetric about the direction of propagation, gravitational waves have an azimuthal dependence that ultimately results in the creation of not only E-mode polarization, but also B-mode. Figure 1.4 illustrates two example gravitational waves and the polarization patterns induced by the quadrupole moments. In panel (c), a "plus" type gravitational wave propagates perpendicular to the line of sight, and a quadrupole moment is generated within each crest and trough. The resulting polarization forms an E-mode pattern like those from density waves in panels (a) and (b). In panel (d), a "cross" type gravitational wave propagates at a non-zero angle with respect to the plane of the page. In this scenario, the projected polarization has a handedness and forms a B-mode pattern. B-mode polarization is created *only* by tensor perturbations and is therefore an extremely powerful test of inflation (some even call it the "holy grail of cosmology").

One advantage of polarization over temperature anisotropies is that there is no equivalent of the ISW effect for the former. That is, polarized emission created at the surface of last scattering is unaffected by time-varying gravitational potentials, and in some sense, it is a purer method of looking at the early universe. However, CMB polarization is affected by several other factors following recombination. First, at a redshift of $z \sim 10$, the first stars formed in the universe and reionized the neutral hydrogen. The same mechanisms that created polarization at recombination also produce polarized emission from the reionized electrons. The polarization power spectra are therefore enhanced at large angular scales that are determined by the expansion of the horizon size between recombination and reionization. The second post-recombination source of polarization is intervening

matter between us and the surface of last scattering. CMB photons are gravitationally lensed by matter along the line of sight, and in the process, some of the E-mode polarization is converted to B-mode at small angular scales. Finally, Galactic synchrotron and thermal dust emission potentially contaminate the cosmological CMB signal. However, these foregrounds are frequency-dependent and vary considerably over the sky, so there are ways to minimize this source of confusion.

1.3 CMB power spectra

1.3.1 Formalism

The CMB temperature and polarization anisotropies are, to a good approximation, Gaussian random fields that can be expressed in terms of power spectra. The temperature fluctuations about the mean, $T(\hat{n})/T_0$, are expanded into $Y_{\ell m}$ spherical harmonic basis functions,

$$\frac{T(\hat{n})}{T_0} = 1 + \sum_{\ell=1}^{\infty} \sum_{m=-\ell}^{\ell} a_{\ell m}^T Y_{\ell m}(\hat{n}), \tag{1.38}$$

where $\hat{n}$ is the radial unit vector on the sphere. The expansion coefficients,

$$a_{\ell m}^T = \frac{1}{T_0} \int d\hat{n} \; T(\hat{n}) Y_{\ell m}^*(\hat{n}), \tag{1.39}$$

are averaged over m to form the temperature power spectrum as a function of multipole moment ℓ,

$$C_\ell^{TT} = \frac{1}{2\ell+1} \sum_{m=-\ell}^{\ell} \left(a_{\ell m}^{T*} \, a_{\ell m}^T \right). \tag{1.40}$$

For historic and aesthetic reasons, the power spectrum is generally multiplied by $\ell(\ell+1)/(2\pi)$ so that at large angular scales, the Sachs-Wolfe plateau appears flat in multipole space.

Polarization anisotropies are expressed in terms of the Stokes Q and U param-

eters, which, under rotation by an angle ψ, transform as a spin-2 quantity:

$$(Q \pm iU)'(\hat{n}) = e^{\mp 2i\psi}(Q \pm iU)(\hat{n}). \tag{1.41}$$

Unlike temperature fluctuations, the polarization field is decomposed into spin-2 spherical harmonic functions

$$(Q \pm iU)(\hat{n}) = \sum_{\ell=1}^{\infty} \sum_{m=-\ell}^{\ell} a_{\ell m}^{(\pm 2)} \, Y_{\ell m}^{(\pm 2)}(\hat{n}), \tag{1.42}$$

and the E and B expansion coefficients and power spectra are defined as

$$a_{\ell m}^E = -\frac{1}{2}(a_{\ell m}^{(2)} + a_{\ell m}^{(-2)}) \tag{1.43}$$

$$a_{\ell m}^B = \frac{i}{2}(a_{\ell m}^{(2)} - a_{\ell m}^{(-2)}) \tag{1.44}$$

$$C_\ell^{EE} = \frac{1}{2\ell+1} \sum_{m=-\ell}^{\ell} \left(a_{\ell m}^{E*} \, a_{\ell m}^E \right) \tag{1.45}$$

$$C_\ell^{BB} = \frac{1}{2\ell+1} \sum_{m=-\ell}^{\ell} \left(a_{\ell m}^{B*} \, a_{\ell m}^B \right). \tag{1.46}$$

Because the temperature anisotropies are intrinsically polarized with an E-mode pattern, the temperature and E cross-correlation spectrum is non-zero and displays interesting features. The TB and EB cross-spectra, however, are expected to vanish because the parity of the two halves differ. A complete description of the polarization power spectra and statistics is available in references [19; 20].

1.3.2 Anatomy

The temperature and polarization power spectra of the CMB are a rich source of information about the early universe, with nearly every spectral feature illustrating a different slice of physics. Figure 1.5 illustrates the separate scalar and tensor contributions to the spectra, which are summed in Figure 1.6 to produce the total power spectra that experiments measure. These example spectra were calculated from CAMB using the best-fit parameters from five-year WMAP data to a lambda
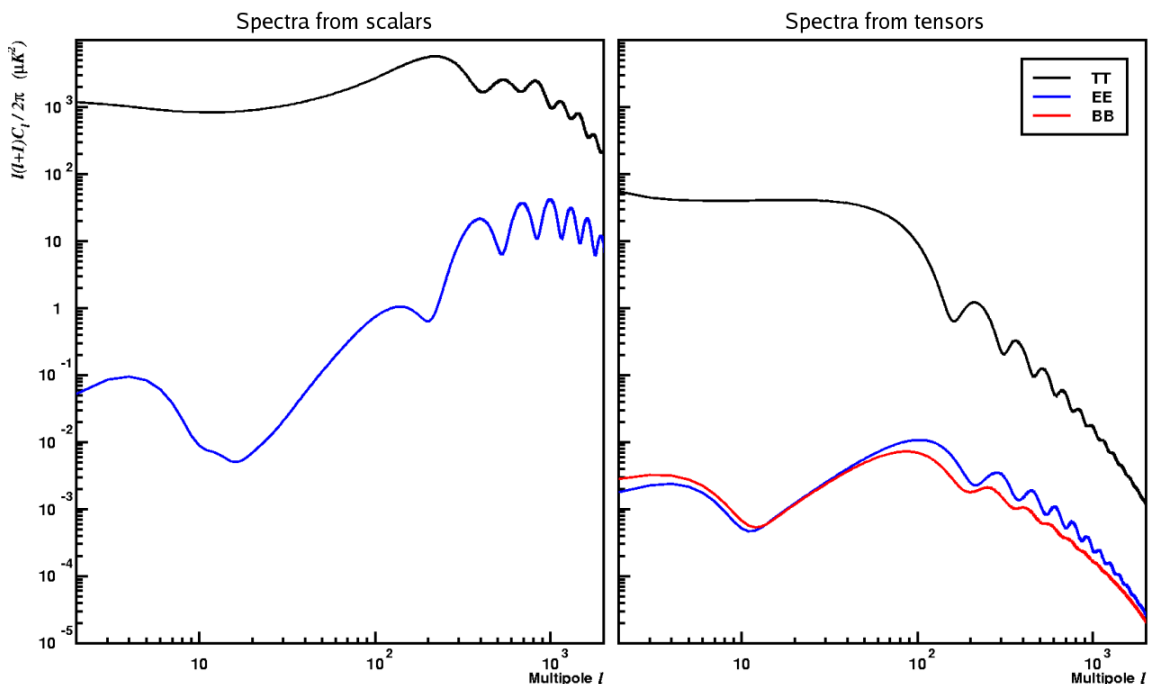
Figure 1.5: Theoretical power spectra from scalar and tensor perturbations are calculated from CAMB using a ΛCDM model. Scalar perturbations (left) produce the well-studied temperature spectrum and the bulk of the E-mode polarization, but they do not produce any B-mode polarization. Tensor perturbations (right) contribute small amounts of TT and EE and can be distinguished from scalar perturbations by the presence of a non-zero BB spectrum. In this figure, $r = 0.1$.

and cold dark matter (ΛCDM) model. The tensor-to-scalar ratio r in this example is 0.1.

At angular scales of $\ell < 100$, the temperature power spectrum is determined by large-scale anisotropies that are outside the horizon at recombination. This flat region of the spectrum, also known as the Sachs-Wolfe plateau, corresponds to primordial perturbations produced directly by inflation. At the largest angular scales, the late-time ISW effect causes a slight rise in the TT spectrum. The power spectrum peaks at $\ell \sim 200$, the acoustic horizon size at the surface of last scattering, and this first peak corresponds to the largest modes that have entered the horizon and have gravitationally collapsed to a state of maximum compression. At these scales, the density contrast is greatest across the sky. The location of the first peak is sensitive to the curvature parameter because as photons free-stream from the
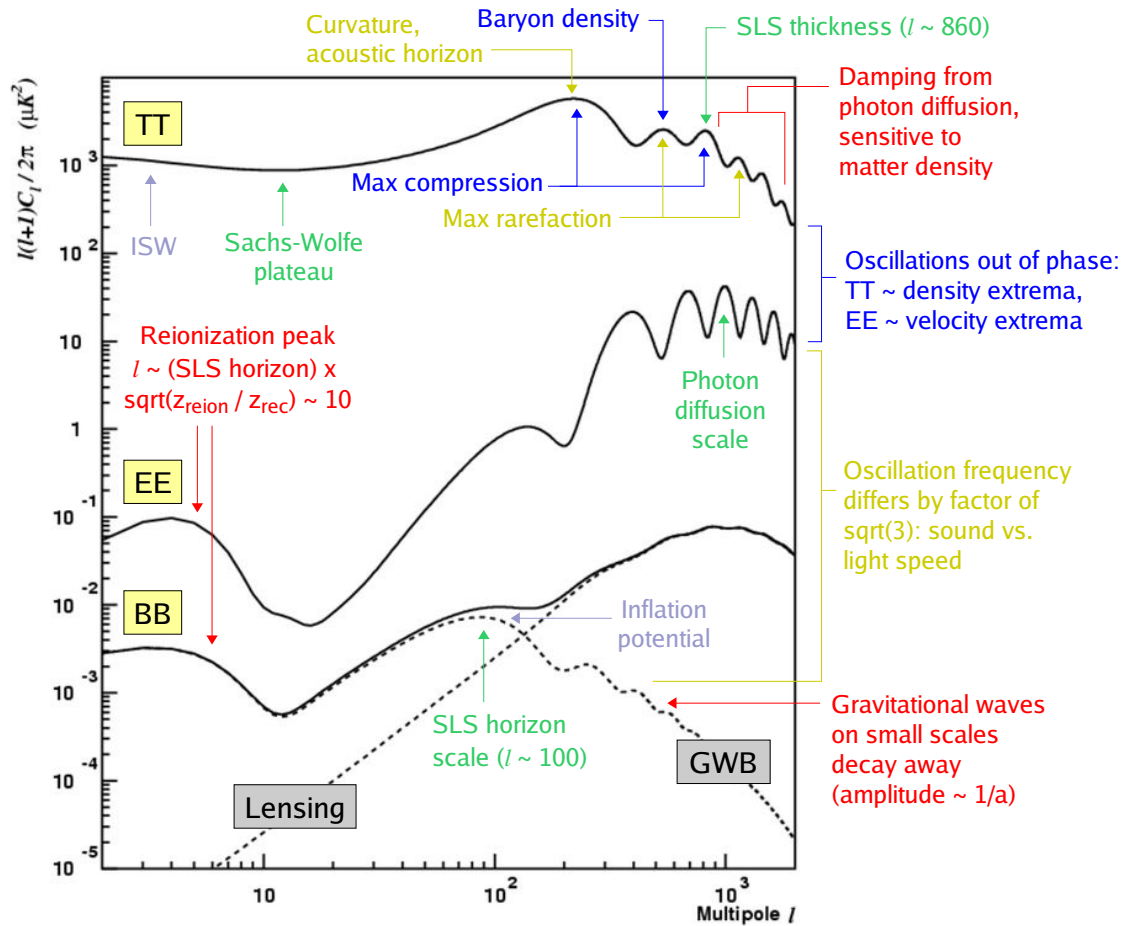
Figure 1.6: The temperature and polarization power spectra of the CMB contain a vast amount of information about the history of the universe. These spectra were calculated from CAMB using the five-year WMAP ΛCDM parameters, and the tensor-to-scalar ratio here is 0.1. See text for details.

surface of last scattering, the geometry of the universe affects the trajectories and thus the perceived size of the temperature fluctuations. An open universe shifts the peaks to higher ℓ, while a closed universe compresses the spectrum to lower ℓ. Measurements of the first peak indicate that the geometry of the universe is extremely close to flat.

The TT peaks and troughs that follow at higher ℓ correspond to smaller modes that have gone through more acoustic oscillation cycles. The second peak, for example, corresponds to modes that have bounced back from being compressed and have reached a state of maximum rarefaction. The trough between the first and second peaks corresponds to the halfway point between compression and rarefaction, where the density contrast and power spectrum amplitude are minimized. The relative amplitudes of the peaks (in particular, the first three) are sensitive to the baryon density, which shifts the zero-point of the acoustic oscillations. Increased baryon density enhances the odd-numbered peaks above the even-numbered peaks and also lowers the oscillation frequency.

At small angular scales above $\ell \sim 860$, the amplitude of the TT spectrum drops rapidly as spectral features become washed out by photon diffusion. The diffusion length depends on the electron density, and the location of the damping tail is therefore sensitive to the baryon density. The overall tilt of the spectrum constrains the scalar spectral index n_s, which is related to the slow-roll inflation parameters. There is some experimental evidence [21; 22] that n_s is slightly less than unity, and this departure implies an increase in the expected tensor-to-scalar ratio in slow-roll inflation models[3].

Given a ΛCDM model, the EE polarization spectrum is uniquely predicted from the temperature spectrum; therefore, polarization measurements provide an excellent consistency check of our understanding of CMB physics. The polarized signal is small because it is sourced only by local quadrupole moments, which are suppressed by Thomson scattering, and the peak of the EE spectrum is about a

---

[3]If n_s is about 0.95 and $\epsilon \sim \delta$, then $\epsilon \sim 0.01$ from Equation 1.17. The tensor-to-scalar ratio is obtained from dividing Equation 1.21 by 1.15 and is approximately 9ϵ, i.e. $r \sim 0.1$.

factor of 100 smaller than the TT spectrum. The quadrupole moments arise from velocity gradients in the photon–baryon fluid, so the EE peaks correspond to velocity extrema and are out of phase with the TT peaks, which correspond to density extrema. (Models with isocurvature initial conditions predict that the EE and TT relative phase is not exactly $180°$, but current data support adiabatic initial conditions.) The peak of the EE spectrum occurs at the photon diffusion scale and drops off on either side. Reionization injects extra power at large angular scales via the same Thomson scattering mechanism that creates the E-mode signal at recombination. The expansion of the horizon size between recombination and reionization determines the location of the low-ℓ bump, and its amplitude constrains the optical depth to reionization. Precision measurements of the low-ℓ EE spectrum may possibly reveal even more details of the universe's reionization history.

The BB power spectrum, which is currently undetected, has a well-defined shape in multipole space but an uncertain amplitude. The current upper limit on the tensor-to-scalar ratio is 0.2 and comes from measurements by WMAP of large-scale temperature anisotropy in combination with baryon acoustic oscillation and Type Ia supernova data [22]. (As shown in Figure 1.5, tensor perturbations generate a small amount of TT power, and the tensor contribution can be constrained by precision measurements of the low-ℓ portion of the temperature spectrum.) The BB spectrum is the sum of two components: the cosmological signal produced by the gravitational wave background, and BB produced by gravitational lensing of the EE spectrum. The cosmological component peaks at the horizon scale, $\ell \sim 100$, and quickly decays on small angular scales. The oscillation frequency depends on the speed of light rather than the sound speed, so the BB and TT/EE peak spacings differ by a factor of about $\sqrt{3}$. The relationship between the peak of the BB spectrum and the energy scale of inflation E_i is

$$\sqrt{\left.\frac{\ell(\ell+1)}{2\pi}C_\ell^B\right|_{\text{peak}}} = 0.024\left(\frac{E_i}{10^{16}\text{ GeV}}\right)^2 \ \mu\text{K},\tag{1.47}$$

where the scaling is apparent from Equation 1.21 and the coefficient is determined

from numerical calculations [23]. Like EE, the BB spectrum is also enhanced at low ℓ by reionization.

1.3.3 Observations

The temperature power spectrum of the CMB has been measured in exquisite detail by many experiments, as shown in Figure 1.2. The WMAP satellite has mapped the temperature fluctuations over the entire sky, the region around the third peak has been filled in by balloon and ground-based experiments such as BOOMERANG and CBI, and on small scales, ACBAR recently resolved the fourth and fifth acoustic peaks for the first time.

Figure 1.7 illustrates the state of the field of CMB polarization. The temperature–polarization cross-correlation (TE) has been detected by many experiments, and the most recent measurements are beginning to tightly constrain the peaks. Numerous experiments have also detected EE polarization, and the latest measurements from QUAD are the first to resolve the acoustic peak structure. The BB spectrum is still undetected, and 95% confidence upper limits are plotted along with a fiducial $r = 0.1$ theory curve. The published upper limits are plotted for DASI and CAPMAP. For CBI and BOOMERANG, the likelihood function for each band power is approximated with an offset lognormal distribution [24], and for WMAP and QUAD, the probability distribution function is assumed to be Gaussian. In these last four cases, the upper limit is calculated by integrating the positive portion of the band power probability distribution up to the 95% point. It is important to note that although the current upper limit on r is 0.2, the constraints from direct polarization measurements to date are far worse—for example, WMAP polarization data alone allow r values as large as 10 within a 68% confidence level [22]. Precision polarization measurement is a daunting task, but with sufficient sensitivity and control of systematics, this experimental approach is a promising technique for breaking past $r = 0.2$. In contrast, large-scale temperature measurements are ultimately limited by cosmic variance and cannot probe r

values much lower than the current limit.

Background Imaging of Cosmic Extragalactic Polarization (Bicep) is a ground-based microwave polarimeter designed specifically to measure the B-mode of CMB polarization at degree angular scales. The experiment is optimized for a multipole window of $30 < \ell < 300$ in order to span the expected cosmological BB peak and to map out the low-ℓ portion of the EE spectrum. The collaboration includes Caltech/JPL, UC Berkeley, UC San Diego, NIST at Boulder, Stanford, University of Chicago, IAP Paris, IAS Orsay, Cardiff University, and CEA Grenoble, and the work presented in this thesis would not have been possible without the combined efforts of the Bicep team. My specific contributions to Bicep have been instrument integration and testing, calibration, and developing one of the two data analysis pipelines.

Detection of B-mode polarization and hence the gravitational wave background would have profound consequences for cosmology and our understanding of the universe: the detection would be to inflation what the discovery of the CMB was to the Big Bang. The question "what happened in the beginning" is one that is asked by people of all ages and disciplines, and telescopes operating from the ground, balloons, and satellites have already made great strides towards answering that question. Upcoming experiments will yield even more rich data sets as we continue pushing the boundaries of precision CMB measurements.
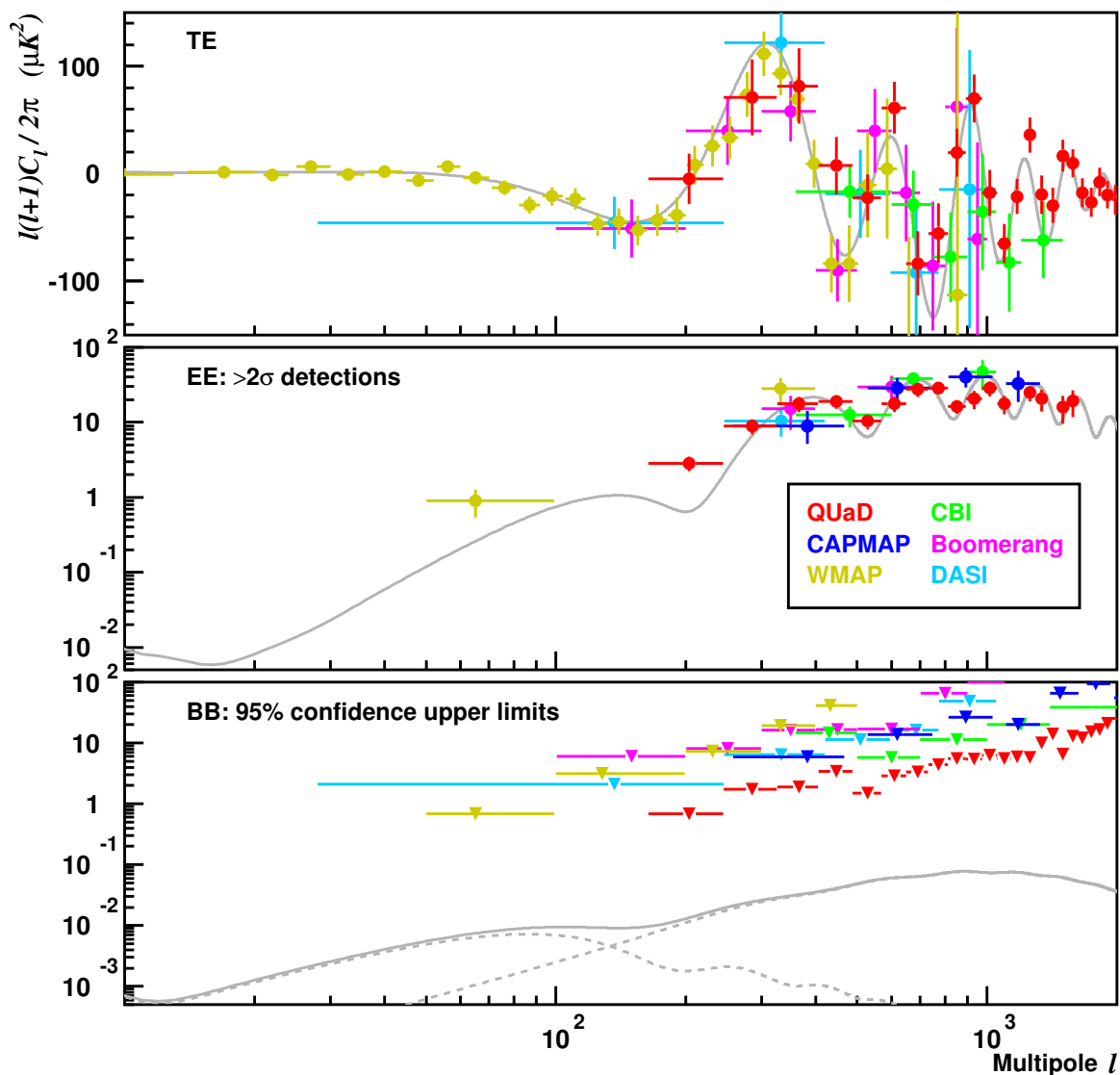
Figure 1.7: Recent measurements of the TE, EE, and BB polarization power spectra from DASI [7], BOOMERANG [9; 25], CBI [8], WMAP [1], CAPMAP [11], QUAD [10]. For the EE spectrum, only $>2\sigma$ detections are shown, and the BB points are 95% confidence upper limits. BICEP is optimized to $30 < \ell < 300$ in order to map out the low-ℓ portion of the EE spectrum and to probe BB with unprecedented sensitivity. The gray TE and EE curves are CAMB model spectra generated with the WMAP five-year best fit ΛCDM parameters. The gray BB curve is the sum of two components (dashed lines): the predicted cosmological spectrum for $r = 0.1$, and the lensing spectrum.

Chapter 2

The BICEP instrument

2.1 Experimental approach

The goal of detecting the B-mode signature in CMB polarization constrains the design philosophy and operating principles of the instrument. To optimize an experiment for the B-mode search, we consider various (and sometimes conflicting) factors that determine the field size, location, and observing frequencies. The BICEP experiment was designed to balance these factors and is the first CMB telescope that was built specifically to function as a B-mode machine.

The B-mode signal is expected to peak at degree angular scales ($\ell \sim 100$), which guides the choice of angular resolution, field of view, and observed sky fraction. In order to bracket the B-mode peak, BICEP is optimized to $30 < \ell < 300$. The upper end of the ℓ range is set by the 0.9° and 0.6° beam sizes at the two observing frequencies, and the lower end is set by the sky coverage, which is chosen to be 1000 deg^2 (corresponding to a sky fraction of 2%). With a 17-degree instantaneous field of view, BICEP can quickly map the required CMB field size.

A large survey size minimizes lensing confusion, which rises at small angular scales and is expected to dominate the B-mode signal at approximately $\ell > 200$. However, a small survey size is favored for two other reasons. First, the field size should be just large enough to capture degree scale features—the sample variance errors on the TT, TE, and EE spectra should be reasonably small—without spreading the integration time too thinly. Second, Galactic foregrounds are present
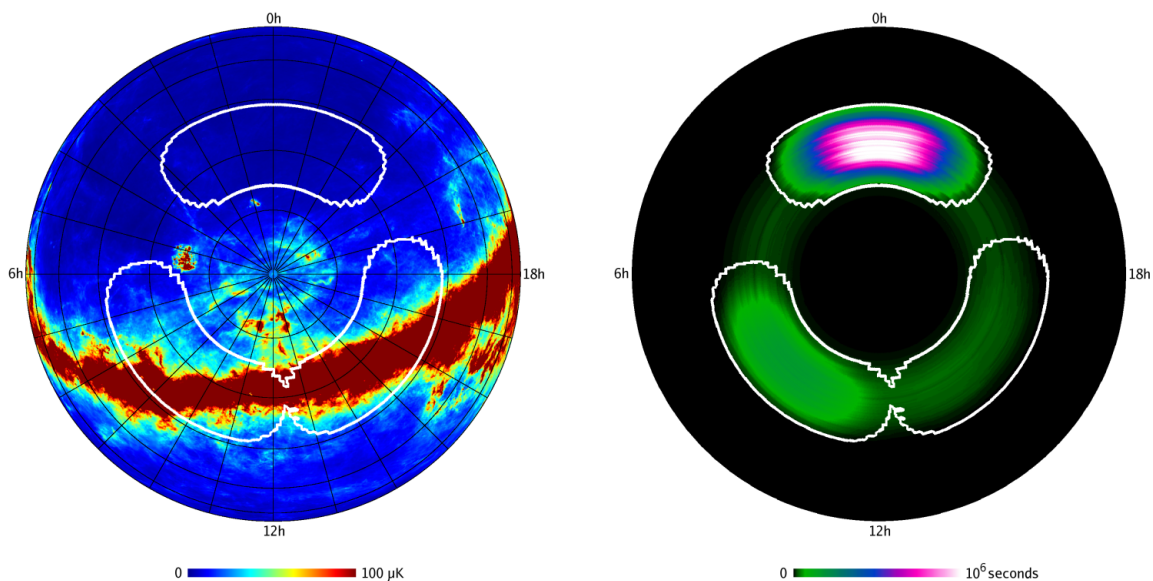
Figure 2.1: In the left image, BICEP's CMB field is outlined (uppermost region) on the 100 GHz Finkbeiner–Davis–Schlegel dust map and lies within the "Southern Hole." The lower left region is the main Galactic field, which includes Eta Carinae and dust at moderate Galactic latitudes. The secondary Galactic field, outlined on the lower right, spans a bright region of the plane. The right image illustrates BICEP's integration time on the sky, which exceeds 10^6 detector-seconds per deg^2 in the CMB field after two years of observing. The garish color scale is not Kiwon-approved but is necessary to show that BICEP has observed the entire constant-declination "donut" centered on the south celestial pole.

at large angular scales, but confusion from dust and synchrotron emission can be minimized by searching for the cleanest, small patches of sky. Figure 2.1 illustrates the dust emission in the southern sky as given by the 100 GHz Finkbeiner–Davis–Schlegel (FDS) dust model [26]. BICEP's primary CMB field, the upper outlined region, lies within the "Southern Hole," where the dust emission is more than 100 times below the median over the entire sky. The northern hemisphere also contains similarly clean regions, but the southern hemisphere has other advantages that we will now discuss.

BICEP observes from the Amundsen-Scott South Pole station, a location that has many benefits for microwave telescopes and adventure-seeking graduate students. The South Pole has a long history [27] of being home to CMB telescopes,

Band center (GHz)	Band width (GHz)	PSB pairs 2006	PSB pairs 2007	Beam FWHM (degrees)	NET ($\mu K_{CMB}\sqrt{s}$)
96.0	22.3	25	25	0.93	560
150.1	39.4	24	22	0.60	430
206.0	46.0	0	2	0.42	800

Table 2.1: BICEP instrument summary.

starting with White Dish in 1992; other experiments that have followed include PYTHON, ACBAR, DASI, QUAD, and SPT. Apart from the excellent infrastructure available at the South Pole, the humidity is lower than anywhere else in the world, which results in reduced atmospheric loading and sky noise. The six months of continuous night during the Austral winter provide extremely stable observing conditions, and the 24-hour visibility of the same part of the sky enables deep integration on contiguous target fields.

The choice of observing frequencies results from three coincidences (that we wish we could claim were all intentional, but this is one of the rare instances in which Nature gives us a free pass). The transmission spectrum of the atmosphere at microwave frequencies defines clean windows in which to place band passes, as shown in Figure 3.3. BICEP observes primarily at 100 and 150 GHz, the first of which is bordered by oxygen lines, and the latter by oxygen and water lines. In addition, the focal plane contains two experimental pixels that operate at 220 GHz. The atmospheric windows coincide with the peak of the CMB spectrum at 150 GHz. In addition, because the dust level in the Southern Hole is particularly low, the combined dust and synchrotron emission is minimized at 150 GHz instead of 65 GHz, which is the minimum on average over the entire sky [28]. With BICEP's moderate frequency coverage, it is possible to distinguish CMB signal from foreground emission.

Guided by the global constraints described above, the task of the CMB experimentalist is to construct an instrument that offers high sensitivity and exquisite control of systematic errors while staying in the parameter space defined by practical and scientific considerations. The remainder of this chapter describes the de-
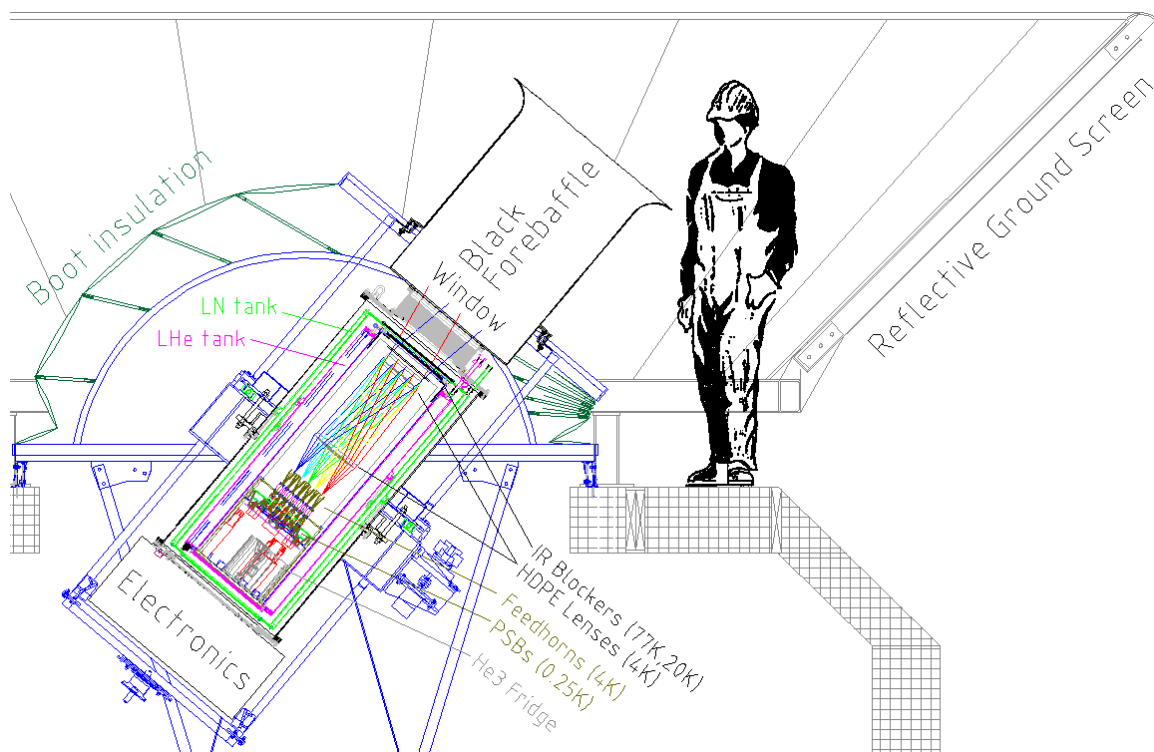
Figure 2.2: The BICEP instrument is housed inside an upwards-looking liquid nitrogen/helium cryostat. Light enters through a zotefoam window and passes through two teflon infrared-blocking filters. Two antireflection-coated polyethylene lenses focus the light onto a 4-K Faraday cage below, which contains the focal plane (feed horn stacks and polarization-sensitive bolometers), JFET readouts, and ^{4}He/^{3}He/^{3}He refrigerator. The telescope is supported by a three-axis mount and observes above the roof line of the Dark Sector Laboratory. A flexible bellows (the "boot") forms an environmental seal between the top of the telescope and the roof. Stray light from the ground is blocked by a comoving blackened forebaffle and a reflective ground screen surrounding the entire telescope.

tails of the design, construction, and operation of the BICEP instrument, which is illustrated in Figure 2.2 and summarized in Table 2.1. BICEP deployed to the South Pole station in November 2005 and achieved first light in January 2006. CMB observations began two months later, and as of this thesis submission, the telescope is in its third successful season of operation. The instrument was opened at the end of 2006 for slight focal plane modifications, but apart from this brief down time, BICEP has been continuously cold and operational for all three years.
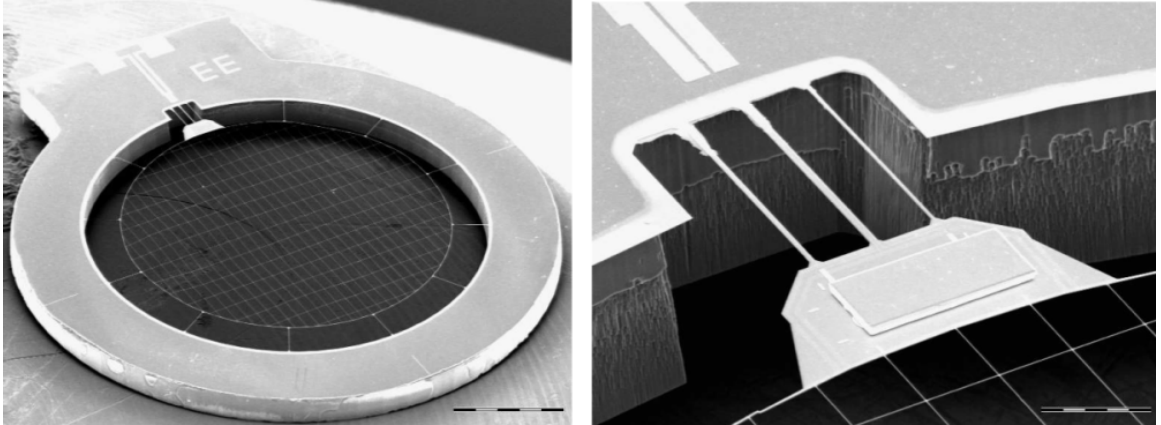
Figure 2.3: A polarization-sensitive bolometer consists of a silicon nitride absorbing mesh that is suspended from radial support legs. The axis of polarization sensitivity is determined by the direction of the grid that is metalized. The right image zooms in on the NTD germanium thermistor that converts temperature changes in the absorber into a voltage signal (carried through leads on the central leg). The legs on either side of the signal leads can be trimmed to adjust the thermal conductance to the 250 mK bath.

2.2 Detectors

The pride and joy of any precision instrument is its detectors, and BICEP relies on polarization-sensitive bolometers [29] (PSBs) to perform its B-mode search. Figure 2.3 shows a typical BICEP PSB, which consists of a 4.5-mm diameter grid-like mesh that absorbs incident radiation while minimizing the cross section to cosmic ray hits. The mesh is etched from a layer of Si_3N_4, which provides structural rigidity, and is suspended from low thermal conductance legs along its outer edge. A thin layer of gold is deposited along one direction of grid to give the detector its polarization sensitivity. The temperature of the absorbing mesh, which varies with incident optical power, is converted to a voltage signal with a neutron transmutation-doped (NTD) germanium thermistor that is located at the edge of the mesh. The BICEP PSBs operate at a bath temperature of 250 mK, and the thermal conductance between the mesh and the bath can be adjusted by trimming the legs shown in the right image of Figure 2.3.

Each pixel in the BICEP focal plane contains an orthogonal PSB pair mounted

in a single housing that acts as a $\lambda/4$ backshort and couples to a corrugated feed horn stack. As described in §4.3, CMB temperature and polarization information is recovered from the sum and difference, respectively, of PSB timestreams in a pair. Atmospheric emission, which is unpolarized, is effectively removed by PSB differencing and allows BICEP to measure CMB polarization from the ground. Systematic errors in polarization that result from PSB differencing are minimized by placing each PSB pair behind the same feed horns and band-defining filters.

The behavior of a PSB is modeled with the following equations:

$$R(T) = R_0 e^{-\sqrt{\Delta/T}} \tag{2.1}$$

$$G(T) = G_0 (T/T_0)^{\beta}. \tag{2.2}$$

The first describes the resistance $R(T)$ as a function of temperature, where R_0 is a fitted parameter and Δ is expected to be 41.8 K based on the material properties of the thermistor. The second equation describes the thermal conductance as a function of temperature, where T_0 is set to 300 mK by convention, and G_0 and β are determined by fits to calibration data. The typical bolometer parameters for BICEP are $R_0 = 100\ \Omega$, $\Delta = 41.8$ K, $G_0 = 60$ pW/K, and $\beta = 1.5$.

PSB detector technology has been successfully demonstrated by BOOMERANG and will also be used by the *Planck* satellite's high-frequency instrument, which is scheduled to launch in early 2009. In addition, the QUAD experiment used an array of PSBs to measure CMB polarization and was recently the first experiment to resolve peaks in the EE spectrum [10]. The BICEP focal plane comprises 49 pairs of optically active PSBs, which is the largest detector array in any CMB polarization experiment (as of the submission date of this thesis), thus giving the instrument unprecedented total sensitivity.

As described in Table 2.1, the PSB pairs are divided primarily between two frequency bands, with 25 pixels operating at 100 GHz and 24 at 150 GHz. Following the 2006 Austral winter, two of the 150 GHz pixels were reconfigured for 220 GHz operation; these experimental pixels are not used for CMB analysis. The detectors

in the focal plane are arranged in six hextants, as shown in Figure 2.4, and the orientation of the detectors in each hextant alternates between focal plane Q and U. Thus, a 60° rotation about the boresight swaps polarization coverage on the sky.

2.3 Feed horns and filters

BICEP's pass bands are defined within atmospheric transmission windows, as illustrated in Figure 3.3. The 100 GHz band edges and the lower edge of the 150 GHz band are set by oxygen lines, while the upper 150 GHz band edge is set by a water line. The oxygen background in the atmosphere is generally stable, but water vapor is poorly mixed in the atmosphere and results in increased atmospheric noise near the 183 GHz resonance peak. The band passes must be carefully constructed in order to avoid hitting any of the atmospheric emission lines.

Each pixel in the BICEP focal plane, as shown in Figure 2.5, consists of a stack of three corrugated microwave feed horns that couple incoming radiation to a pair of PSBs. The lower edge of the frequency band pass for each pixel is defined by the waveguide cut-off imposed by the horn directly above the PSBs. The upper edge is set by a series of metal mesh resonant filters that are placed in front of the PSB feed horn. The filters are composed of multiple layers of metal grids photolithographed on dielectric substrates that are hot-pressed together, and the surface is antireflection (AR) coated to minimize loss. The metal mesh acts as a low-pass filter with a frequency cut-off set by the length scale of the grid structure. The transmission spectrum of the filters exhibits spectral leaks at multiples of the cut-off frequency, so it is necessary to stack several filters with different cut-offs in order to block these leaks. Even small leak levels can cause serious problems in gain matching and excess optical loading, since the spectra of most backgrounds increase as the square of the frequency. In addition, high-frequency radiation potentially excites multiple modes in the feed horns, thus degrading the beam shape and polarization purity. For BICEP, the 100 and 150 GHz edge-defining filters have frequency cut-offs of 3.65 cm^{-1} and 5.90 cm^{-1}, respectively. Two additional blocking filters with

BICEP Focal Plane: 2007
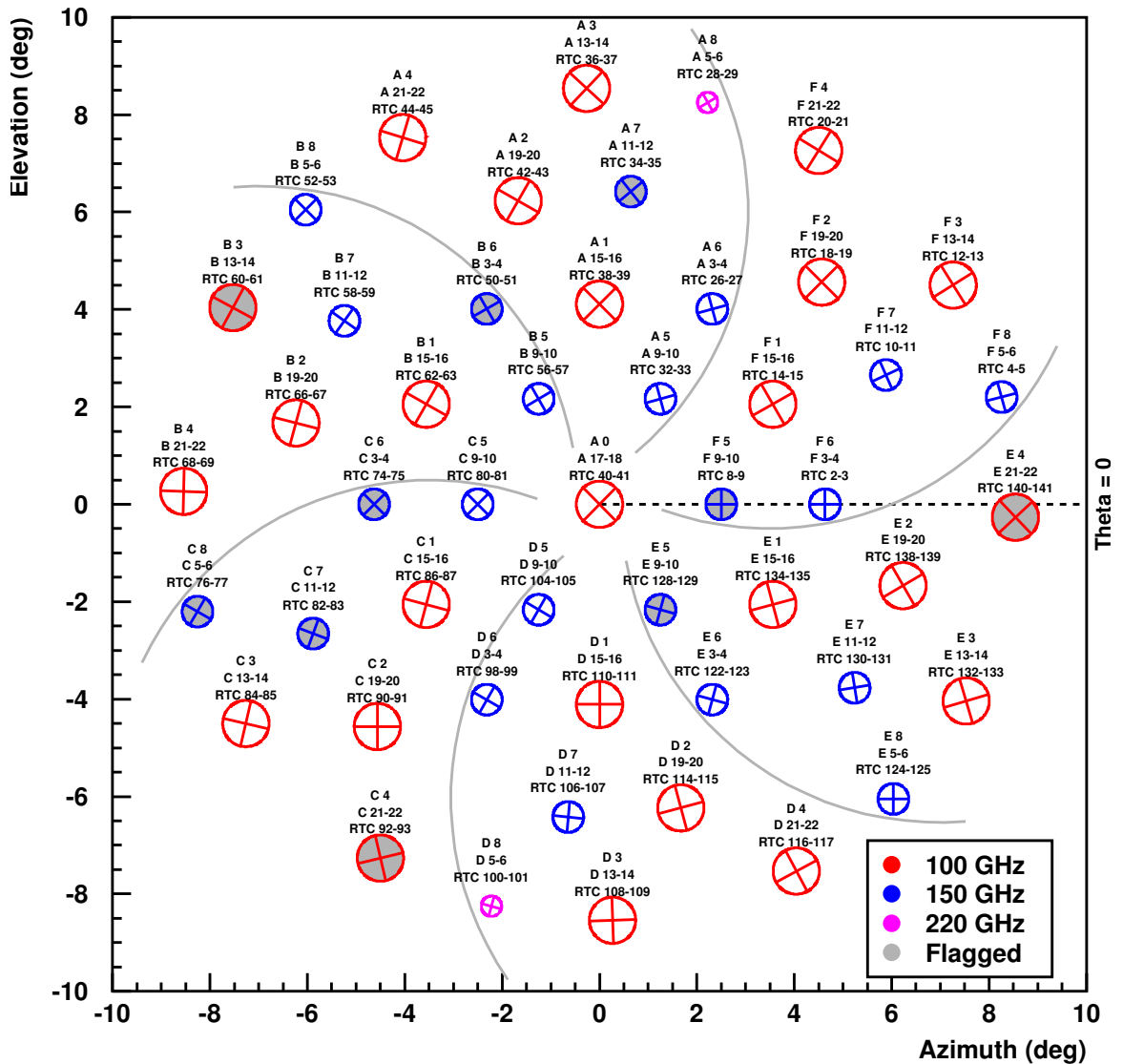
Figure 2.4: Schematic of the BICEP focal plane illustrating the configuration used for the 2007 and 2008 observing seasons. The focal plane comprises 25, 22, and 2 PSB pairs operating at 100, 150 and 220 GHz, respectively. The lines inside each circle correspond to the orientation angles of the PSBs. The focal plane has six-fold symmetry, as shown by the gray curved lines, and the orientation of the pixels in each hextant alternates between focal plane Q and U. Gray pixels are flagged for 2007 and 2008 and are excluded from analysis. (The 2006 focal plane configuration is identical to 2007/2008 except for some of the flagged detectors and the orientation of a few edge pixels. In addition, pixels A4, A8, C4, C8, E4, E8 had Faraday rotator modules, and pixels A8 and D8 operated at 150 GHz.)
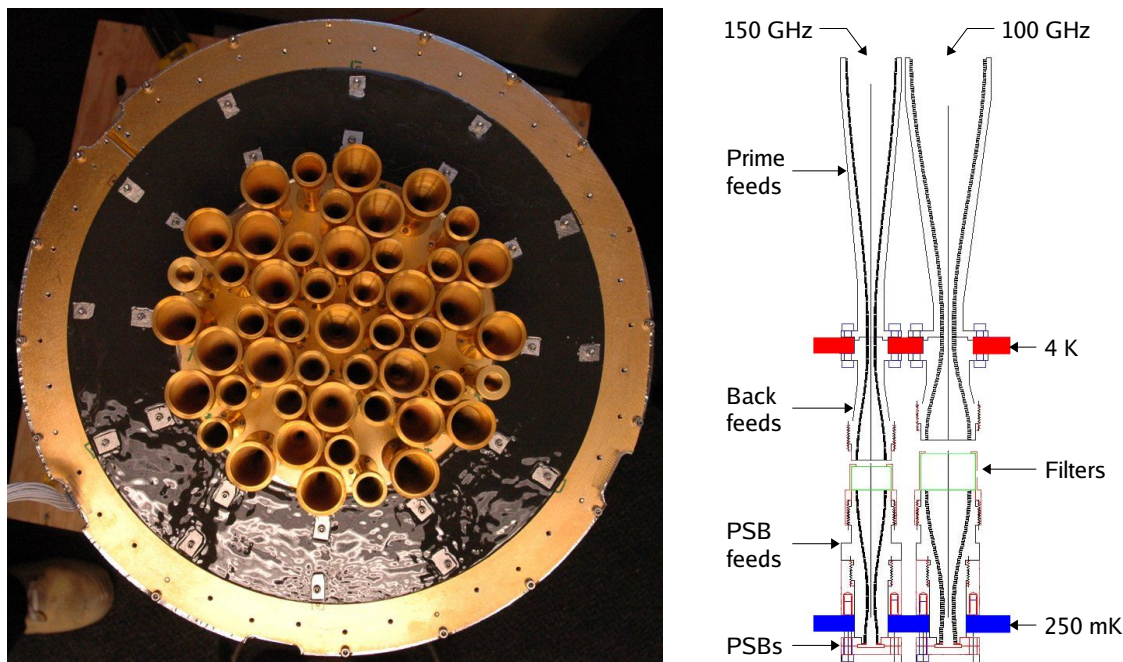
Figure 2.5: The photo on the left shows a CMB photon's view of the BICEP focal plane, which contains 49 pixels, each containing a PSB pair. A schematic of a 150 and 100 GHz pixel is shown on the right. Each pixel consists of three microwave feed horns and a stack of metal mesh filters, and a thermal gap above the filters separates the 4-K prime and back feeds from the PSBs, which operate at 250 mK.

slightly different cut-offs are used in conjunction with the edge filters for each frequency band. Measurements of the spectral pass bands and high frequency leaks are discussed in §3.3.

The feed horn stacks in BICEP are based on designs that have been successfully demonstrated in ACBAR and BOOMERANG. To couple incident radiation to the PSBs, only a single feed horn is necessary, and this is the design that QUAD successfully used in their focal plane. However, the addition of back-to-back horns in front of the PSB horn allows clean separation of filtering and beam definition. Profiled, corrugated feed horns provide low side lobe response and high polarization fidelity in comparison to smooth-walled feeds, and a detailed description of the horn design and optimization for BICEP is given in reference [30]. The beam-defining prime horns produce nearly Gaussian beams with 6.04° FWHM at 100

and 150 GHz. The frequency cut-off of the prime/back feed throat is slightly lower than that of the PSB horn so that the Faraday rotator module (§2.4), which sits at the junction, operates away from the band edge. The prime and back feeds, which are heat sunk to a 4 K liquid helium bath, are separated from the 250-mK PSB horn by a thermal gap section that is surrounded by a light baffle. The metal-mesh filters are held in place at the PSB horn aperture with screw-on caps loaded with beryllium-copper spring washers. The PSB horn defines the lower edge of the pass band and reconcentrates the light onto the PSBs below.

2.4   Faraday rotator modules

The original BICEP focal plane design included a Faraday rotator module (FRM) in each of the pixels, placed between the prime and back horns. The FRM is a solid-state polarization switch that employs the Faraday effect in order to quickly modulate polarized light at cryogenic temperatures without using any moving parts. Such a device is useful for tuning the signal band of the instrument, which is otherwise set by a combination of the scan speed and beam size, and can pull the signal away from any microphonic lines that might be present. In addition, the FRM mitigates any polarization systematic effects introduced by optical elements downstream of the modulator. Each FRM consists of a ferrite cylinder surrounded by a waveguide section, which is wrapped in a wire coil that functions as a solenoid. Alumina cones are attached to both ends to the ferrite to provide a smooth transition in the index of refraction. Applying current to the solenoid generates a longitudinal magnetic field in the ferrite, which then rotates incoming linearly polarized light by an angle proportional to the applied field.

The FRMs are devices specifically developed for BICEP and have not been used in other experiments. As a result, the FRMs were subjected to rigorous testing and characterization prior to deployment in order to determine whether or not the devices were suitable for CMB polarimetry. Figure 2.6 illustrates a PSB pair's response to linearly polarized light (from an aperture-filling wire grid placed on
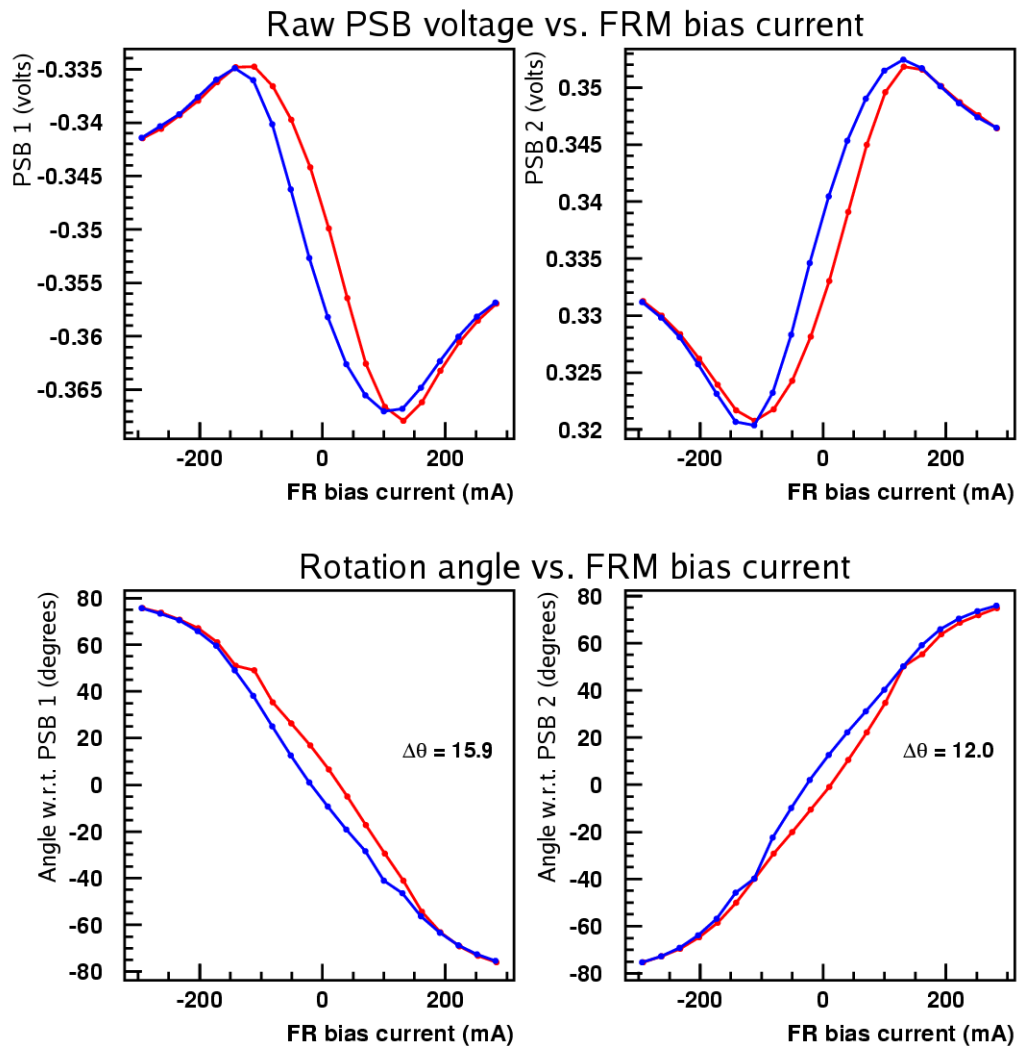
Figure 2.6: The rotation angle curve of each FRM is characterized by placing an aperture-filling wire grid at the telescope window and ramping the FRM bias current. In this particular example, the grid is positioned at $\sim 45°$ with respect to the PSBs, and the bias current is a 0.1-Hz triangle wave. The raw voltage response of a bolometer pair is plotted in the upper panels. Red and blue correspond to increasing and decreasing FRM bias current, respectively. In the lower panels, the bolometer voltages are converted to the angle of rotation of the incoming light. The FRMs display hysteresis, and the curve separation at zero bias current is between $10°$ and $25°$.

the window), rotated by the FRM. As the FRM bias current ramps up and down, the raw bolometer timestreams trace out a sinusoidal curve that flattens at the end points as the ferrite begins to saturate. The FRM rotation angle θ is calculated with the expression

$$\theta = \frac{1}{2} \arcsin \left(\frac{V - (V_{\text{max}} + V_{\text{min}})/2}{(V_{\text{max}} - V_{\text{min}})/2} \right), \tag{2.3}$$

where V is the bolometer voltage and V_{max}, V_{min} are the voltage timestream maximum and minimum. On average, the FRMs produce 45° rotation with ~ 100 mA bias, with a maximum rotation angle of about 80° at ~ 300 mA. An unexpected feature of the FRMs is the presence of hysteresis in the ferrite; as shown in the lower panels of Figure 2.6, the separation between the increasing- and decreasing-bias curves is between 10° and 25°. Alarmingly, this curve separation depends on the FRM bias frequency and asymptotically decreases to a non-zero value as the frequency drops to zero. In principle, the hysteresis curves can be mapped as a function of bias frequency and could be used as look-up tables for FRM operation. There is some evidence that the exact placement of the curves depends on the bias history of the FRM, and it is therefore necessary to precede FRM usage with a standard AC ramp-down procedure. Although FRM usage is complicated by hysteresis effects, the rotation angle curves have been measured to be stable within $\pm 0.1°$ over >24 hours.

The spurious polarization introduced by the FRMs themselves was characterized by placing unpolarized 300-K and 77-K aperture-filling sources at the window and biasing the FRMs through the full range of rotation. The resulting "instrumental polarization" is defined as

$$\frac{1}{2} \cdot \frac{V_{\text{AC}}(300\text{K})}{V_{\text{DC}}(300\text{K}) - V_{\text{DC}}(77\text{K})} \cdot \frac{300\text{K} - 77\text{K}}{300\text{K}}, \tag{2.4}$$

where $V_{\text{AC}}(300\text{K})$ is the peak-to-peak bolometer voltage at 300 K, and $V_{\text{DC}}(300\text{K})$ and $V_{\text{DC}}(77\text{K})$ are the mean bolometer voltage levels at 300 K and 77 K. Typical instrumental polarization levels for BICEP FRMs are 1% and have no significant measured time-variation. The polarization, which is visible in plots of the bolome-

ter output versus FRM bias current, displays the same hysteresis as illustrated in Figure 2.6 when the telescope observes a polarized source.

Although the FRMs are successful polarization modulation devices with sufficiently low instrumental polarization, the death sentence for FRMs in BICEP came in a noise performance showdown between FRM-demodulated and PSB-differenced data. Stability data taken shortly before deploying the instrument indicated that the FRMs introduced excess white noise, and the power spectral densities of the FRM-demodulated bolometer timestreams were significantly higher than those from differenced PSBs. As a result, all but six FRMs were removed from the BICEP focal plane for the 2006 observing season, and the remaining six were removed during the 2006–2007 Austral summer. The simple, yet effective, PSB differencing strategy has worked extremely well for BICEP. Upcoming CMB polarization experiments seeking to probe lower tensor-to-scalar limits may benefit from polarization modulation, as systematics become dominant limiting factors. BICEP2 and SPIDER, which are both small-aperture experiments, plan to use a rotating waveplate at the aperture so that only polarized emission from the sky is modulated. The waveplate is likely a more effective approach than FRMs, which modulate any polarized radiation from the upstream telescope optics.

2.5 Focal plane and 4-K insert

The focal plane assembly is illustrated in Figure 2.7 and consists of a trussed structure that isolates the 250-mK inner plate from the 4-K prime and back horns. The 250-mK plate is the attachment point for the detectors and PSB horns, and the detector bias and read-out lines are distributed on a circuit board that mounts on the underside. The PSBs are biased in series with load resistors, which are contained in six modules mounted at the perimeter of the plate. Graphite-loaded Vespel legs connect the 250-mK plate to an intermediate ring cooled to 350 mK. A second series of Vespel legs connect the 350-mK ring to another thermal buffer ring at 1.4 K, which is connected by a third set of Vespel legs to the outer 4-K feed horn plate.

4 K

1.4 K

250 mK

350 mK

Resistor
modules

PSBs

Heat
straps

4-K Faraday cage "insert"   Drop-in focal plane assembly
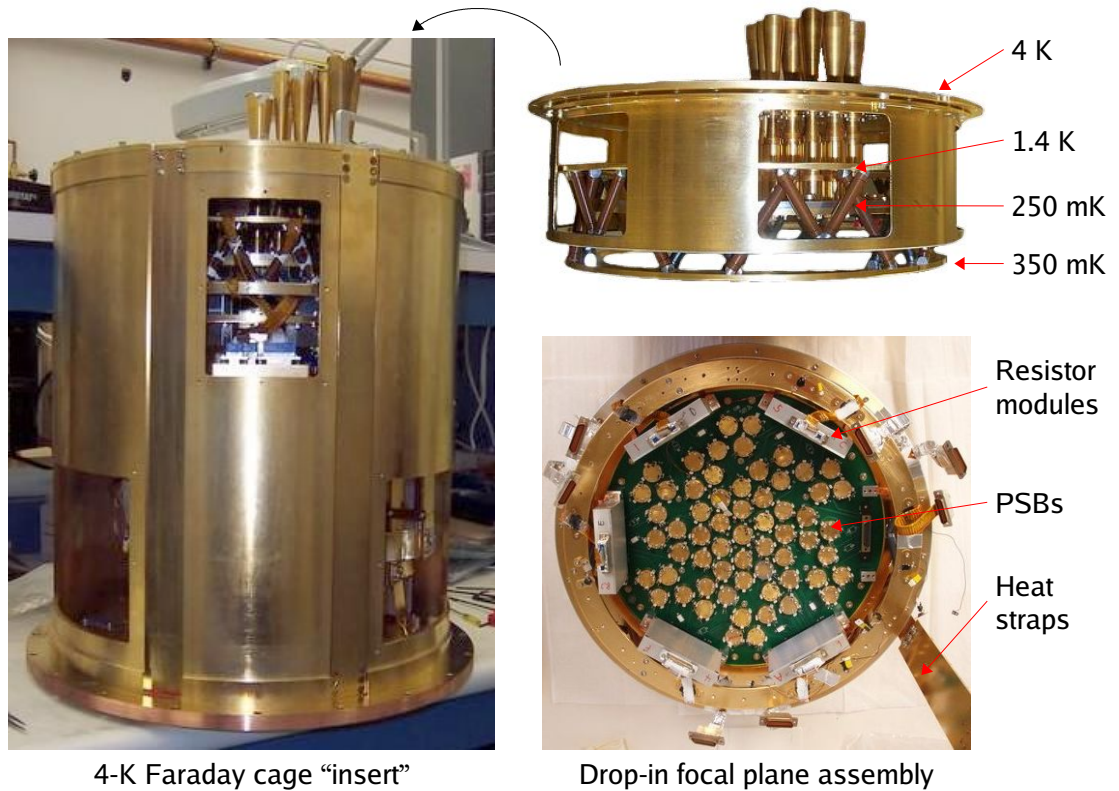
Figure 2.7: The focal plane assembly, shown on the upper right, is a trussed structure with four thermally isolated sections. The innermost plate operates at 250 mK and is separated from the 4-K feed horn plate by several series of Vespel legs and temperature buffer rings. The underside of the focal plane, pictured on the lower right, contains the PSB modules, load resistors, and circuit board that distributes the bias and signal lines. The entire focal plane assembly drops into the 4-K "insert," shown on the left, which acts as a Faraday cage for the PSBs, JFET modules, and sub-Kelvin refrigerator. Cooling power from the refrigerator to the focal plane is conducted along three gold-plated copper heat straps.

The focal plane drops into the top of a cylindrical "insert," which is heat sunk to 4 K via a beefy copper base plate that bolts to the bottom of the liquid helium tank. The insert access windows that are visible in Figure 2.7 are closed and sealed during telescope operation so that the detectors are enclosed in an RF-tight Faraday cage. The insert also serves as the housing for three JFET modules and the ^{4}He/^{3}He/^{3}He sorption refrigerator that cools the focal plane. Three gold-plated copper bars run vertically between the refrigerator stages and isolated sections of the focal plane to supply 1.4-K, 350-mK, and 250-mK cooling power.

In addition to the optically active PSBs, the 250-mK plate is outfitted with six dark PSB pairs, six thermistor pairs (consisting of un-etched bolometers), and 12 5-MΩ resistors, all located near the edge of the focal plane. The thermistors and dark channels monitor thermal instabilities and microphonics in the focal plane, and the resistors are sensitive probes of RF interference. The focal plane temperature is held at 250 mK with a PID control loop on a thermistor channel, using a 100-kΩ resistor as a heater. In the 2006 season, the control thermistor was located on the 250-mK plate, close to the heat strap connection to the refrigerator (Figure 2.4, near pixel A4). Because of the large thermal mass of the focal plane and a 0.6-s delay in the thermistor timestream (caused by the lock-in amplifier), the response time of the PID loop to thermal disturbances was typically ∼30 s. Thermal disturbances are usually transmitted through the focal plane heat straps, so in 2007, two thermistor pairs and extra heater resistors were added directly to the strap for control purposes. The lock-in amplifiers for the strap thermistor channels were reprogrammed to reduce the timestream delay to 0.1 s, and the resulting response time of the PID loop was reduced to ∼5 s. The heat straps were also stiffened with Vespel supports, and the 2007 season showed improved thermal stability compared to the 2006 season.

2.6 Telescope optics

BICEP uses a cold, refracting telescope consisting of two biconvex lenses (Fig-

ure 2.2) to focus light onto the focal plane. The azimuthal symmetry and absence of mirrors minimizes instrumental polarization systematics, and the small aperture size, set to 25 cm to achieve degree-scale resolution, greatly simplifies many calibration procedures. For example, the aperture is easily entirely filled by thermal sources and and wire grids, and the far field of the instrument is only 50 meters away. Figure 2.8 illustrates the layout of the BICEP telescope and a ray trace diagram of the optics. The optical design is telecentric to be compatible with the flat focal plane, and the edge taper at the aperture is about -20 dB to minimize internal spill-over and far-field side lobes. The plate scale is $\sim 1^\circ$/cm, which yields a field-of-view of approximately 17°. The lenses are constructed from high-density polyethylene (HDPE) and are AR-coated with thin layers of Zitex, which is a porous, low-density form of teflon. Low-density polyethylene (LDPE) film is placed between the lens surfaces and the Zitex layers, and the entire assembly is pressed together and heated above the melting temperature of the LDPE. Physical optics simulations indicate that the Strehl ratios of this lens configuration are >0.99 over the entire field of view, and the cross polarization is of order 10^{-5}.

The lenses are held in place with thin aluminum strips that flex as the HDPE cools and contracts. Cooling power to the lenses is supplied separately through copper braids that are heat sunk to 4 K, and the operating temperatures of the lenses are measured to be <8 K. The lenses are mounted inside a rigid aluminum tube (Figure 2.8, right photo), along with light baffles that consist of knife-edge circular apertures blackened with carbon-loaded epoxy. The lens tube is bolted to the top of the 4-K Faraday cage that houses the focal plane and sub-Kelvin refrigerator, and teflon strips are attached to the outer surface of the tube to guide the entire assembly into the cryostat.

The heat load on the optics and cryogen baths is reduced with two absorptive teflon IR-blocking filters that are located above the lens tube. The filters are mounted to the top surface of the 77-K liquid nitrogen tank and to the 20-K liquid helium vapor-cooled stage (VCS), and the measured equilibrium temperatures are 130–150 K and 70–80 K, respectively. Like the HDPE lenses, the filters are also
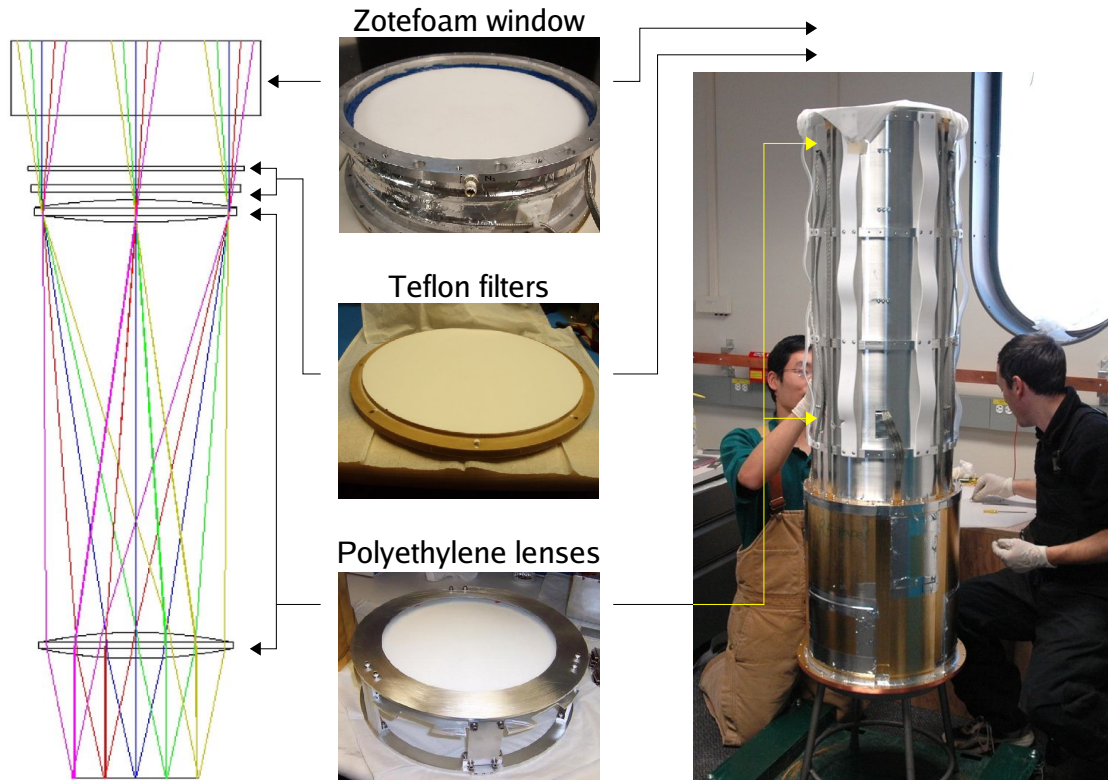
Figure 2.8: The BICEP telescope consists of two AR-coated polyethylene lenses that operate at cryogenic temperatures. The lenses are mounted inside a tube (right photo) that bolts on top of the 4-K Faraday cage that houses the focal plane. Two teflon filters, located above the telescope assembly, block IR radiation and reduce the heat load on the cryogen baths. The window is made of zotefoam, which also conveniently serves as a burst disc if the vacuum space becomes overpressured.

AR-coated with Zitex layers, and the teflon slabs are chemically etched to aid the heat-bonding process.

The window at the entrance of the telescope is constructed from four sheets of zotefoam, a closed-cell foam that is nearly transparent at microwave frequencies, that are heat-bonded together to form a single 10-cm thick slab. The zotefoam "skin," a smooth outer layer created during the manufacturing process, is removed from the window surfaces to minimize reflection losses, and the transmission of the BICEP window is measured to be ∼99%. The foam is epoxied inside a cylindrical aluminum frame with a 300-mm diameter aperture, as shown in Figure 2.8.

Under vacuum, the top surface deflects inwards by ∼3 cm; lab testing also shows that the zotefoam conveniently serves as a burst disc if the vacuum space becomes overpressured. To prevent frost accumulation, the window is covered with a thin sheet of polypropylene film, and the intermediate space is continuously purged with nitrogen gas. The ring that fixes the polypropylene cover to the window is machined with radial slots to direct warm air, rising inside the lab, onto the film surface. Heating the film slightly above the ambient temperature causes any occasional snow accumulation to quickly sublimate. Images from an IR camera, mounted at the edge of the window, show visible snow accumulation for about 7% and 2% of scanning data in 2006 and 2007, respectively. (The ring slots were enlarged between the two seasons.)

2.7 Cryogenics

The BICEP receiver is housed in a cryostat with concentric toroidal liquid nitrogen and liquid helium tanks. The geometry allows the telescope to look upwards and provides an azimuthally symmetric thermal environment. The nitrogen tank acts as a radiation shield for the helium tank, and multiple layers of aluminized mylar are sandwiched between the tanks to reduce the radiative heat load. The maximum hold times of the nitrogen and helium tanks are about three and four days, respectively, although the nitrogen is refilled every two days in order to match the observing schedule. The focal plane and optics tube assembly are inserted from the bottom of the cryostat and bolt to the lower surface of the helium tank to form a thermal connection to the 4-K bath. Helium boil-off gas is directed through a copper heat exchanger at the top of the tank and provides cooling power to the vapor-cooled stage (VCS), which serves as the mounting point for one of the two teflon IR-blocking filters. (The other filter mounts directly to the top of the liquid nitrogen tank.) The VCS temperature is typically ∼20 K during operation and varies with the liquid helium level. The heat exchanger, which consists of a long, small-diameter copper tube that coils around the inner cryostat wall, is an ice plug
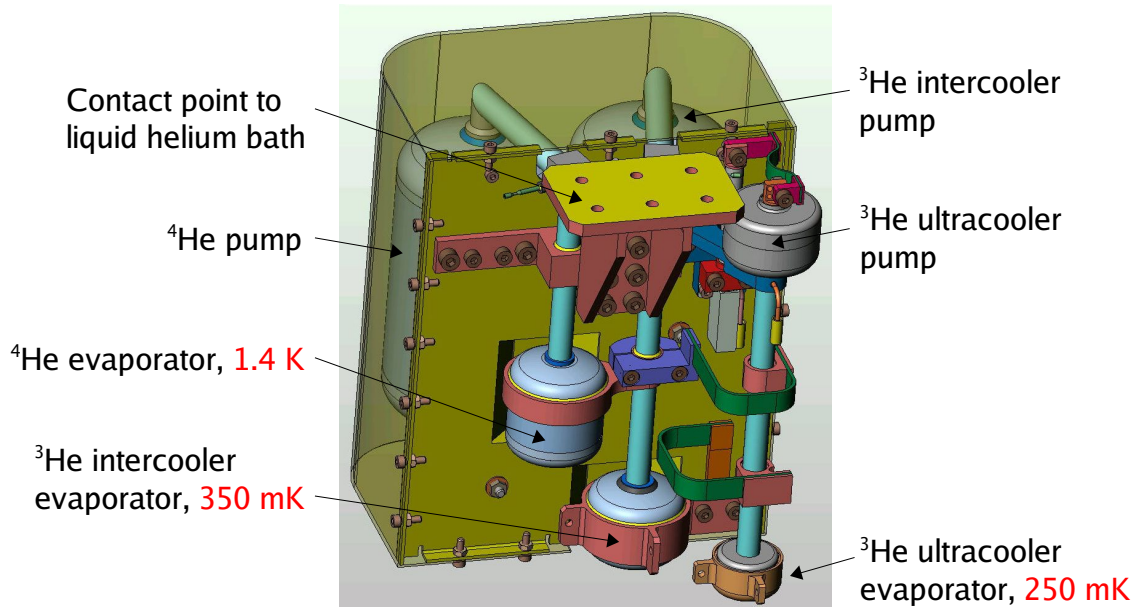
Figure 2.9: The closed-cycle helium sorption refrigerator has three stages: the 1.4-K ^{4}He stage, 350-mK ^{3}He intercooler, and 250-mK ^{3}He ultracooler. The ^{4}He and intercooler charcoal pumps are located on the opposite side of the evaporators and are enclosed in a radiation shield. (The ultracooler pump has a separate shield, which is not shown.) A copper foot at the top of the refrigerator is the contact point to the 4-K liquid helium bath.

death trap, and care must be taken to prevent reverse flow of gas through the tube.

The focal plane is cooled by a closed-cycle ^{4}He/^{3}He/^{3}He sorption refrigerator (Figure 2.9) that mounts to the 4-K base plate of the focal plane insert. The condensation point of the ^{4}He stage is cooled by the liquid helium bath, and the evaporator of each stage is thermally linked to the condensation point of the subsequent stage. The operating temperatures are approximately 1.4 K, 350 mK, and 250 mK for the ^{4}He, ^{3}He intercooler, and ^{3}He ultracooler, respectively. Although the ultracooler can reach temperatures as low as $\sim$230 mK, we choose to operate the focal plane at 250 mK to avoid thermal spikes and instabilities that appear at lower temperatures. The charcoal pumps for each stage are cooled by gas-gap heat switches and are located away from the evaporators, surrounded by light-tight shields. Recycling the refrigerator is a $\sim$4-hour process, plus an extra hour for temperatures

to stabilize. 20 hours after the beginning of the cycle, the ^{4}He stage runs out and equilibrates at 2.4 K, cooled by vapor from the intercooler stage. In response to this change, the temperature of the focal plane increases by 0.5 mK. The maximum hold time of the refrigerator, limited by the intercooler stage, is ~60 hours (however, recycling is performed every 48 hours during standard observing).

2.8 Telescope mount

The BICEP receiver is supported in a three-axis mount that rotates in azimuth, elevation, and continuously about the boresight (also called the telescope "deck"). The mount and receiver are located on the top floor of the Dark Sector Laboratory at 89.99° S, 44.65° W, and the receiver observes above the roof line (Figure 2.2). A flexible bellows or "boot," which moves with the telescope in elevation, forms an environmental seal between the top of the telescope and the roof so that the lower part of the instrument is accessible in a warm lab environment, as shown in Figure 2.10. The boot restricts BICEP's elevation range to 50–90 degrees. A brush seal between the boot and the roof allows rotation in azimuth, and a second brush seal on the upper telescope platform permits boresight rotation. The receiver is loaded into the mount using the "cryoloader," a sliding bracket mounted on two rails that extend between the lab floor and the top of the elevation cage. After the cryoloader is positioned on the mount, the cryostat is strapped to the bracket and hoisted along the rails until it reaches the top. Because space is limited under the boot, the cryostat is cooled while it is off the mount and loaded after the focal plane reaches 4 K.

The boresight pointing of the telescope and mount is determined from star observations with an optical camera, which is rigidly bolted to the top surface of the cryostat. Dedicated pointing calibrations are performed every two days during the refrigerator cycle, weather permitting, as well as before and after each mount releveling. The optical camera data are fit to a pointing model to establish azimuth and elevation encoder offsets, the tilt of the azimuth axis, and the angle between
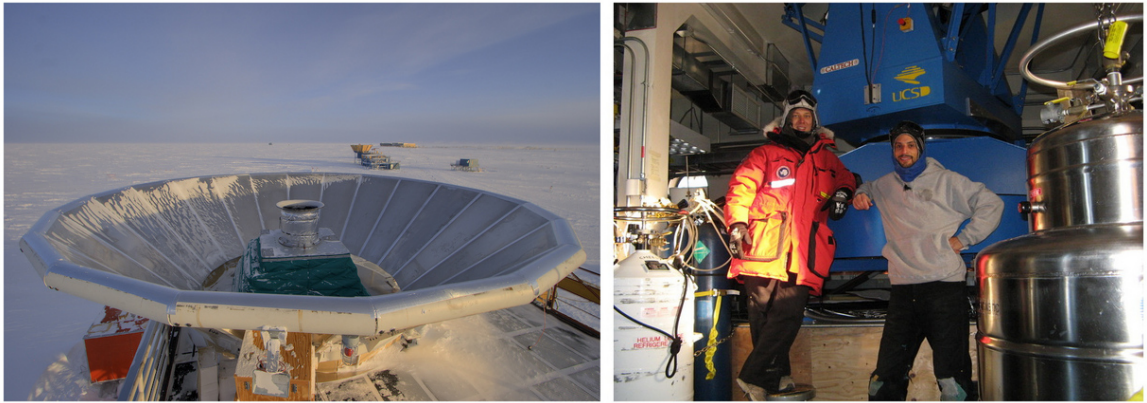
Figure 2.10: BICEP observes from the roof of the Dark Sector Laboratory, as shown on the left. The forebaffle is attached to the upper platform and rotates in boresight with the telescope, and the entire top portion of the instrument is surrounded by a ground screen. The green fabric is the bellows that insulates the telescope from the harsh Antarctic weather. Below the roof cut-out (right), the instrument and the humans enjoy a cozy lab environment. Photos courtesy of Steffen Richter and Denis Barkats, BICEP's trusty winter-overs.

the elevation and azimuth axes. Tilt data are also obtained from two orthogonal tilt meters installed directly on the mount. The tilt drifts as much as $0.5'$ per month, possibly due to the building settling on the snow, and the mount is re-leveled before the tilt exceeds $1'$.

BICEP uses two levels of external shielding, as shown in Figure 2.10, to block stray light radiated or reflected from the ground. A forebaffle is mounted on the upper telescope platform and is directly bolted to the zotefoam window flange so that the telescope and baffle have comoving boresight rotation. The forebaffle is cylindrical with a rounded lip, which reduces diffraction, and the inner wall is lined with Eccosorb HR-10 foam, a microwave absorber. To prevent snow accumulation on the Eccosorb, the forebaffle is lined with an additional layer of smooth Volara polyethylene foam. Surrounding the entire telescope is a large reflective ground screen, installed on the roof of the lab. The ground screen is slanted so that stray side lobes are reflected to the sky, and the outer lip is rounded (like the forebaffle) to reduce diffraction. BICEP's baffle system works sufficiently well that even data taken during the Austral summer show no evidence of sun contamina-

tion. The far side lobe rejection and baffle performance are discussed in further detail in §3.7.4.

2.9 Readout electronics and control system

Each bolometer is connected in series with two 20-MΩ load resistors and is AC-biased at 100 Hz during standard observing. The bias voltage is produced by a digital sinusoidal waveform generator that can be commanded from the control system software. To minimize the length of high-impedance bolometer wiring, the bolometer signals are immediately directed into cold JFET amplifiers that are located in the 4-K insert space, close to the focal plane. The JFET modules, originally developed for Herschel/SPIRE, consist of thin membranes that support the JFETs, which self-heat and operate at ∼120 K. The electronics noise is dominated by the JFETs, which typically contribute 7 nV/$\sqrt{\text{Hz}}$.

The JFET outputs pass through RF-filtered connectors on the 4-K insert base plate and exit through the bottom of the cryostat into a room-temperature Faraday cage that houses the preamplifiers, which apply anti-aliasing filtering and a gain of ∼200. The amplified signals then pass to the digital lock-in amplifiers, where they are multiplied by a sine and cosine and filtered to produce demodulated outputs. The lock-in outputs are bundled onto an ethernet bus, which is converted to an optical fiber signal and sent to the data acquisition computer through a slip ring. The slip ring is located at the bottom of the elevation cage and rotates with the telescope in boresight. In total, there are 144 lock-in outputs, 98 of which correspond to optically active bolometers. The remaining 46 channels are distributed between dark bolometers, thermistors, and resistors. A separate electronics box, also located at the bottom of the cryostat, processes thermometry data from GRT, Cernox, and diode temperature sensors located on the focal plane, refrigerator, optics tube, and cryogen tanks. The data rate from the lock-in amplifiers is 50 Hz, while the thermometry and other housekeeping data are sampled at 1 Hz.

The BICEP control system uses the gcp software, which is in its Nth incarna-

Phase	Length (hours)	Description
A	6	Cryogen servicing, refrigerator cycle
B	9	CMB, bottom half of elevation range
C	9	CMB, top half of elevation range
D	6	Galactic field
E	9	CMB, top half of elevation range
F	9	CMB, bottom half of elevation range

Table 2.2: Breakdown of 48-hour observing cycles.

tion, having been used by DASI, CBI, SZA, QUAD, and SPT. The code structure consists of three main components: (1) the antenna layer, which receives telescope data, (2) the control layer, which processes commands given to the telescope, and (3) the mediator layer, which acts as an interface between the antenna and control layers. An additional gcp module provides an interface with the PMAC, which controls the telescope motion. An interactive viewer enables real-time telescope monitoring, and commands can be issued either manually from the viewer or with observing scripts written in the gcp scheduling language.

2.10 Observing and telescope operations

2.10.1 Sky coverage and scan strategy

The fields that BICEP observes are illustrated in Figure 2.1 on the 100 GHz FDS dust model. The primary CMB field approximately spans $-60° < \mathrm{RA} < 60°$ and $-70° < \mathrm{dec} < -50°$ and lies within the Southern Hole, where the thermal dust emission is more than 100 times below the median of the entire sky. After two years of observing, the integration time in the deepest region of the field exceeds 10^6 detector-seconds per square degree, and the coverage is smoothly apodized at the edges. BICEP also spends a significant amount of time observing a Galactic field that includes Eta Carinae and dust at moderate Galactic latitudes; the right map in Figure 2.1 illustrates the integration time relative to the CMB field. A moderate amount of time has also been spent observing a secondary Galactic field, which
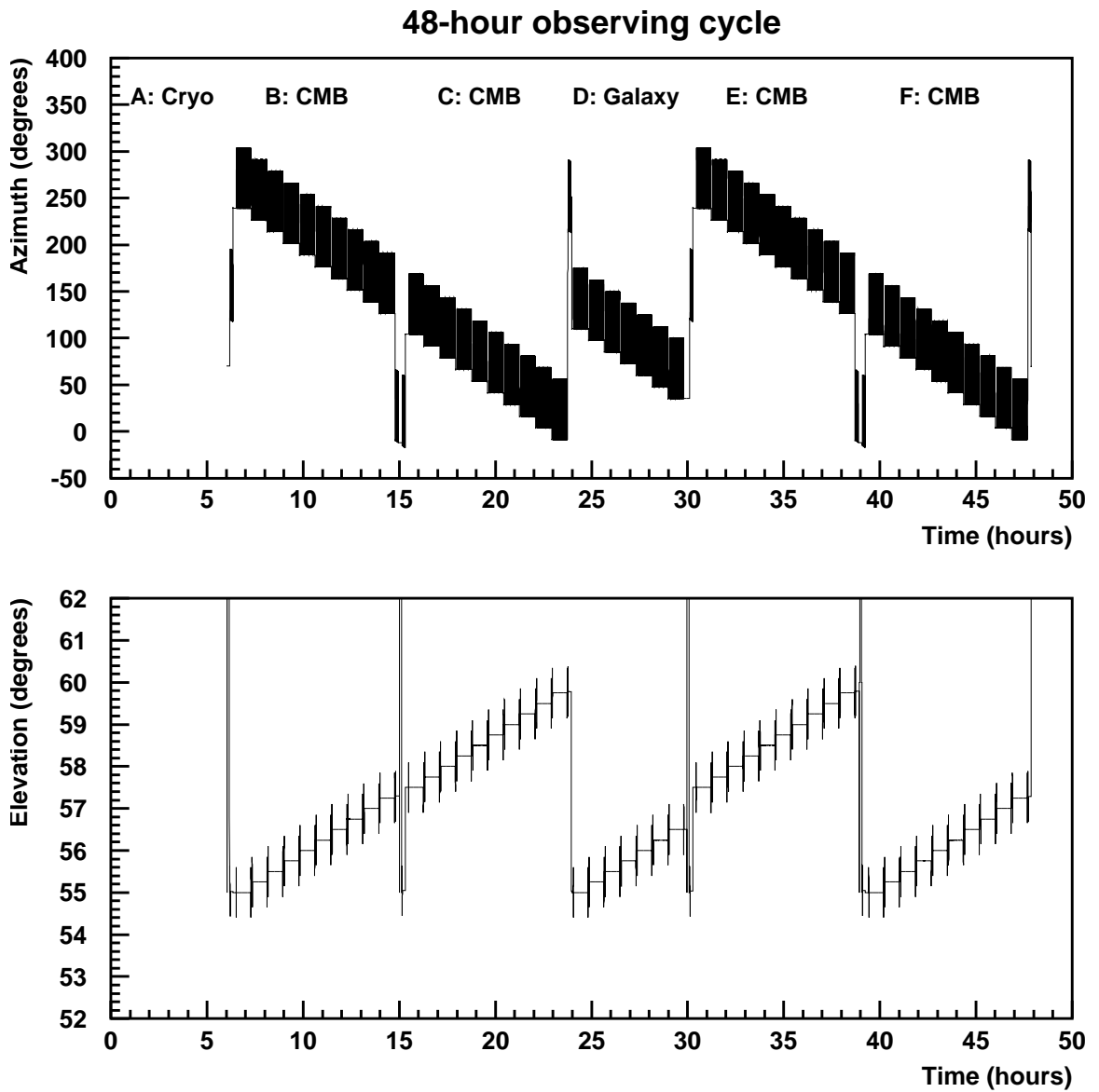
48-hour observing cycle

Figure 2.11: BICEP operates on a 48-hour cycle that is divided into six phases. In each of the phases devoted to CMB or Galaxy observations, the telescope performs azimuth scans at fixed elevation steps. Galactic calibration scans occur at the beginning and end of each phase, and elevation nods at the beginning and end of each elevation step.
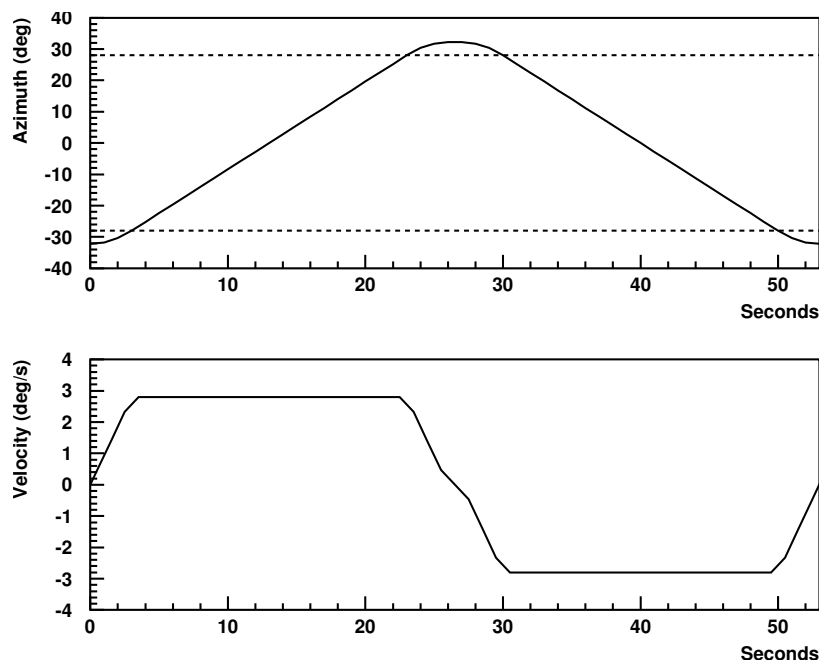
Figure 2.12: The azimuth scan profile (upper panel) has a constant speed of 2.8 deg/s, and the turn-arounds have 1.4 deg/s^2 acceleration and 0.47 deg/s^3 jerk. The constant speed portion, illustrated by the dotted lines and the velocity profile in the lower panel, comprises about 70% of the scan.

spans a brighter region of the plane. The combined coverage of the two Galactic fields lie within a Galactic latitude and longitude range of approximately $|b| < 25$ and $255 < l < 345$. In the 2008 observing season, BICEP began experimenting with 360° azimuth scans, and the telescope has recently observed the entire constant-declination "donut" centered on the south celestial pole.

The BICEP observing cycles are 48 sidereal hours in length and are divided into six phases, as shown in Table 2.2 and Figure 2.11. The first six-hour phase (A) is devoted to recycling the refrigerator and cryogen servicing. Liquid nitrogen and liquid helium are refilled every two and four days, respectively. Star pointing calibrations with the optical camera are also performed during phase A. The following two nine-hour phases (B, C) are spent observing the CMB field, with each phase covering half of the field's elevation range. The Eta Carinae Galactic field is observed during the next six-hour phase (D) while the CMB field moves behind the

South Pole Telescope, BICEP's large[1] neighbor in the Dark Sector. Finally, the CMB field is covered a second time during the final two nine-hour phases (E, F). These two phases span the same azimuth range as phases B and C; however, the elevation halves are mapped in the opposite order. This elevation reversal allows a powerful "first-second day" jackknife that is sensitive to ground contamination.

During each 48-hr observing cycle, the boresight is fixed at one of four angles $\{0°, 180°, 135°, 315°\}$ that were chosen for their thermal stability. Scan-averaged thermistor signals were measured at 16 different boresight angles, and microphonic instabilities were clearly present for a subset of those angles. The chosen four angles give two independent measurements of Q and U, which form the basis for a boresight angle-pair jackknife.

BICEP maps the sky with azimuth-elevation raster scans. During each complete CMB observation (two phases), the telescope boresight steps in elevation between $55°$ and $59.75°$ in $0.25°$ increments. At each step in elevation, the telescope performs a set of 50 back-and-forth azimuth scans over a total period of $\sim$50 minutes. The scans have a fixed azimuth center that is updated once per elevation step to track the RA of the field center. This scan strategy was chosen instead of continuous RA tracking in order to allow removal of any azimuth-fixed or scan-synchronous contamination. The subtraction procedure simply involves binning the bolometer timestreams in azimuth to form a template signal, which is then subtracted from the timestreams. Although azimuth-fixed subtraction also removes some of the CMB signal at low ℓ, the amount of information preserved steadily rises at $\ell > 40$ and eventually asymptotes to 100%. In contrast, lead-trail field differencing, a commonly used ground subtraction method, results in a factor of approximately two in sensitivity loss at all angular scales. Ground contamination is sufficiently low in BICEP data that we have not implemented the subtraction scheme in the analysis so far; we are just beginning to investigate the effect of ground subtraction on jackknife spectra.

Figure 2.12 shows BICEP's azimuth scan profile, which spans $64.4°$ and has a

---

[1]BICEP is small on the ground but big on the sky.

constant speed section of 2.8 deg/s, 1.4 deg/s^2 acceleration at the turn-arounds, and 0.47 deg/s^3 jerk. The azimuth scanning modulates the sky signal, which is placed in a frequency band of approximately 0.1–1 Hz by the 2.8 deg/s scan speed at $\sim$57° elevation. Several scan speeds in a range of 1.0–4.0 deg/s were tested, and the chosen scan profile minimizes microphonic-induced thermal instabilities in the focal plane thermistors.

2.10.2   Gain calibration

Relative detector gains are measured regularly during observing cycles with three different methods: "elevation nods," an infrared source, and scans across the Galactic plane. The first two are performed at the beginning and end of each fixed-elevation scan set, and the Galactic scans occur at the beginning and end of the observing phase.

During an elevation nod, the boresight elevation performs a rounded triangle wave motion with a 1.2° peak-to-peak amplitude, and the detector voltages vary in response to the changing line-of-sight air mass. The calibration procedure and results are discussed in more detail in §3.2. The nod is performed over a 45-s period to reduce thermal disturbances on the focal plane, and thermal drifts are further suppressed by using mirror-image elevation nods at the beginning and end of each scan set (up-down-up and down-up-down).

The elevation nods are preceded by another gain calibration procedure using a pulsed infrared source. The source consists of infrared diodes embedded at the end of a zotefoam arm, which is mounted at the bottom of the forebaffle next to the window. A solenoid rotates the arm and positions the diodes over the center of the window, and the diodes are pulsed at 0.5 Hz to produce a $\sim$100-mK optical signal. Although the gains derived from this method appear to be stable, there are a number of uncertainties associated with the calibrator, including $\sim$3 K excess optical loading introduced by the zotefoam arm, unknown source polarization, and uneven illumination across the focal plane. The calibration data have therefore not

been analyzed, and the arm assembly was removed during the 2007–2008 Austral summer.

At the beginning and end of each observing phase, BICEP briefly observes the bright Galactic field at a single elevation with eight back-and-forth azimuth scans (about 10 minutes). The Galactic plane is visible in the bolometer timestreams and provides a third method of calibrating relative gains. However, we have chosen not to use these gains in the analysis because the elevation nods have higher signal-to-noise.

Chapter 3

Instrument characterization

Precision cosmology demands tight control and detailed understanding of instrumental systematic effects. Minuscule B-mode polarization is easily mimicked by imperfections in the telescope, so it is necessary to thoroughly characterize the instrument, propagate the measured calibration quantities through the analysis pipeline, and determine the final effect on the power spectra. This unpleasant, yet critical, task is described in this chapter. The first part focuses on the calibration techniques and results, and the second part on implications for the power spectra.

A bolometer voltage timestream $d(t)$ is related to the signal on the sky through the expression

$$
\begin{aligned}
d(t) \;=\; & K(t) * \left(n + \frac{1}{2} g \int d\nu\, A_e F(\nu) \int d\Omega \{ \right. \\
& P_{\parallel}(r, \nu, \hat{x})[I(\nu, \hat{x}) + \frac{1-\epsilon}{1+\epsilon}(Q(\nu, \hat{x})\cos 2\psi + U(\nu, \hat{x})\sin 2\psi)] + \\
& \left. P_{\perp}(r, \nu, \hat{x})[I(\nu, \hat{x}) - \frac{1-\epsilon}{1+\epsilon}(Q(\nu, \hat{x})\cos 2\psi + U(\nu, \hat{x})\sin 2\psi)]\} \right). \quad (3.1)
\end{aligned}
$$

The underlying cosmological signal is expressed in terms of the Stokes parameters I, Q, U as a function of frequency ν and position on the sky $\hat{x}$. (The time-dependence that arises from the scan strategy has been suppressed for clarity.) The response of a perfect linearly polarized detector is $I + Q\cos 2\psi + U\sin 2\psi$, which depends only on the detector's polarization orientation angle ψ. However, in a real instrument, this simple expression is buried under a large number of terms that describe the instrument's imperfections. The cross-polar leakage, which is a

PSB's level of response to orthogonally polarized light, is parameterized by ϵ. The detector signal is convolved with the co-polar and cross-polar beams, $P_\parallel(r, \nu, \hat{x})$ and $P_\perp(r, \nu, \hat{x})$, which have spatial extents that depend on the coordinate r. The beam-convolved detector response is integrated over the pass band $F(\nu)$, which is multiplied by the effective antenna area A_e. The gain factor g converts temperature to voltage units, and n is an additive noise term. Finally, the entire expression is convolved with the detector transfer function $K(t)$.

In order to recover CMB temperature and polarization with fidelity, it is necessary to measure all the terms in Equation 3.1 that relate I, Q, U to the detector voltage. The list includes detector transfer functions $K(t)$, absolute and relative gains g, spectral band passes $F(\nu)$, beam shapes $P(r, \nu)$, cross-polar leakage ϵ, and detector orientation angles ψ. In addition, the detector pointing $\hat{x}$ must be precisely reconstructed. (The noise n is discussed separately in §4.4.2.)

3.1   Transfer functions

Deconvolving detector transfer functions is one of the first steps in producing clean timestreams that are suitable for analysis. BICEP scans in azimuth at 2.8 deg/s at an elevation of about $60°$, so the target angular scales of $30 < \ell < 300$ correspond to a frequency range of about 0.1–1 Hz. As discussed in §3.2, the PSB relative gains are measured at 0.02 Hz, so the transfer functions must be characterized over a frequency range that spans at least 0.01–1 Hz in order to link the relative gains to the entire science band.

As illustrated in Figure 3.1, the transfer functions were measured with a Gunn oscillator or broadband noise source (BNS) placed near the telescope window. The Gunn/BNS was square-wave modulated at 0.01–0.1 Hz with a PIN switch, and the detector transfer functions were obtained by averaging the Fourier transforms of the time-domain response to each transition. In order to maintain optical loading conditions representative of CMB observations, the measurements were made with the receiver pointing at zenith, and the microwave sources were coupled to
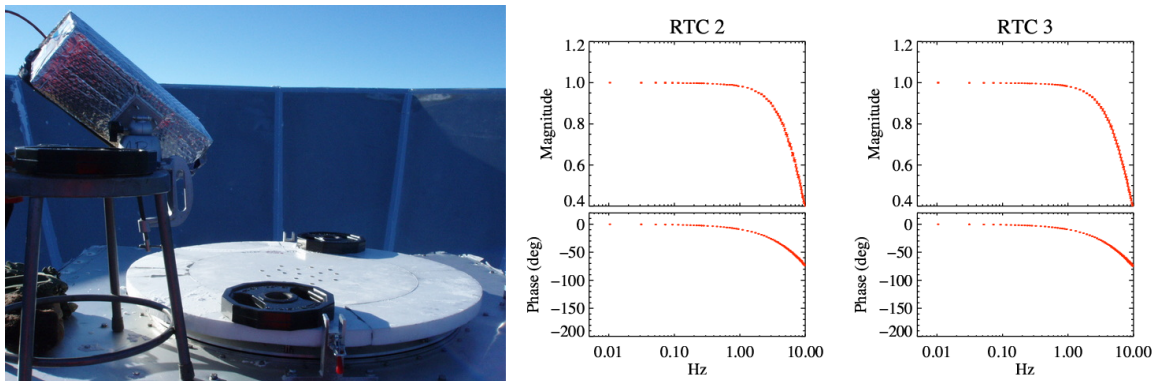
Figure 3.1: The detector transfer functions are measured with a Gunn oscillator or BNS (left image). The signal is scattered into the telescope with washers placed on top of a zotefoam sheet, and the observations are made with the telescope pointing at zenith. Example transfer functions for two PSBs in a pair are plotted on the right.

the telescope via scattering from washers placed on top of a zotefoam sheet at the aperture. Loading dependence and detector nonlinearity were investigated by placing emissive foam chunks in the beam and using different source attenuations; a complete description is available in [30]. Example transfer functions for two PSBs in a pair are plotted in Figure 3.1. The measurements are repeatable within 0.5% between the first and second observation years (with the exception of a few detectors, which are excluded from the science analysis). The relative gain mismatch within PSB pairs, after deconvolving the transfer functions, is $< 0.3\%$ over 0.01–1 Hz. The transfer functions are well described by the model

$$\tilde{K}(\omega) = \tilde{K}_0 \left[\frac{1-\alpha}{(1-i\omega\tau_1)(1-i\omega\tau_2)} + \frac{\alpha}{1-i\omega\tau_c} \right], \qquad (3.2)$$

and the median time constants are $\tau_1 = 20$ms and $\tau_2 = 5$ms. Several detectors exhibit excessive low-frequency roll off ($\alpha > 0.05$ and $\tau_c \geq 300$ms) and are excluded from analysis. The model provides a convenient framework for interpreting the transfer functions in terms of time constants; however, to clean the raw bolometer timestreams, we choose to deconvolve the measured transfer functions directly. The measurements have sufficiently high signal-to-noise, and it is not necessary to rely on model fits.
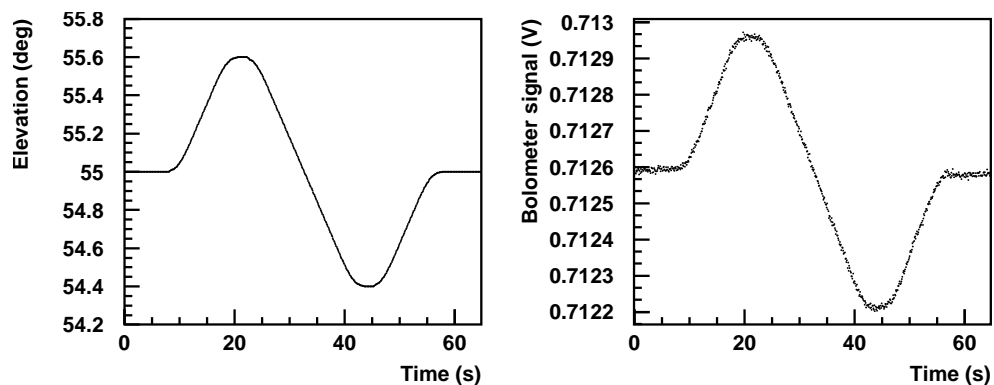
Figure 3.2: An example elevation nod, which is used to calibrate detector relative gains. The boresight elevation motion, shown on the left, is a rounded triangle wave with a peak-to-peak amplitude of 1.2 degrees and period of about 45 s. The corresponding bolometer signal, shown on the right, varies in proportion to the line-of-sight air mass, or $\mathrm{csc(el)}$.

3.2   Relative and absolute detector gains

Relative and absolute detector gains are measured separately using two different techniques. The relative gains are measured with "elevation nods," which are small telescope movements in elevation, as illustrated in Figure 3.2, that inject an atmospheric signal into all of the detectors. The elevation motion during a nod is a rounded triangle wave with a peak-to-peak amplitude of 1.2 degrees and duration of about 45 s. The gain is obtained by fitting the bolometer signal against the cosecant of the detector elevation, which is proportional to the line-of-sight air mass. Elevation nods are performed every 50 minutes at the beginning and end of each set of fixed-elevation azimuth scans, and the relative gains are normalized to the average over the good light detectors during the scan set.

The relative detector gains fluctuate at the few-percent level throughout the observing seasons and have no apparent dependence on optical loading. As a cross check of the elevation nod method, we have also derived relative gains by correlating timestream atmospheric noise within PSB pairs, and the results from the two methods agree within $\pm 0.3\%$. To test the common-mode rejection, PSB pair-sum and pair-difference maps were cross-correlated to measure the amount

of CMB temperature leakage into pair-differences. The resulting median cross-correlation amplitude is 0.4% at degree angular scales.

Once the detectors are calibrated relative to each other, the timestreams are coadded into maps that are in detector units. To convert these units to Kelvin, we cross-correlate the CMB temperature fluctuations measured by WMAP and BICEP to obtain absolute gains. The WMAP maps are smoothed to BICEP's resolution and then converted to detector timestreams using the telescope pointing data. The timestreams are filtered and converted back into maps, thus creating a "BICEP-observed" version of the WMAP data. The BICEP map and processed WMAP maps, which have identical beam and filter functions, are cross-correlated in multipole space to obtain the absolute gain

$$g_\ell = \frac{\langle a_{\ell m}^{\mathrm{WMAP-W}} a_{\ell m}^{*\,\mathrm{WMAP-V}} \rangle}{\langle a_{\ell m}^{\mathrm{WMAP-W}} a_{\ell m}^{*\,\mathrm{BICEP}} \rangle}. \tag{3.3}$$

To avoid noise bias, the $a_{\ell m}$ coefficients in the numerator are taken from two different WMAP maps (in this case, W and V-band). The resulting gain calibration g_ℓ is approximately flat in an ℓ range of about 30–300, where the lower bound is set by the timestream polynomial filtering, and the upper bound is set by beam uncertainty. The absolute gain used for each of the BICEP frequency bands is a single number taken from the average of g_ℓ in this ℓ window.

3.3 Spectral band passes

Band pass mismatches between PSBs in a pair potentially introduce relative gain errors because the relative gains are measured from atmospheric emission, which has different spectral behavior than the CMB. However, because each PSB pair in BICEP is positioned behind a single stack of feed horns and filters, the spectra are expected to match closely. The detector band passes were measured with a portable Martin-Puplett Fourier transform spectrometer (FTS) with 0.3 GHz frequency resolution. The FTS was positioned on the roof of DSL outside the BICEP
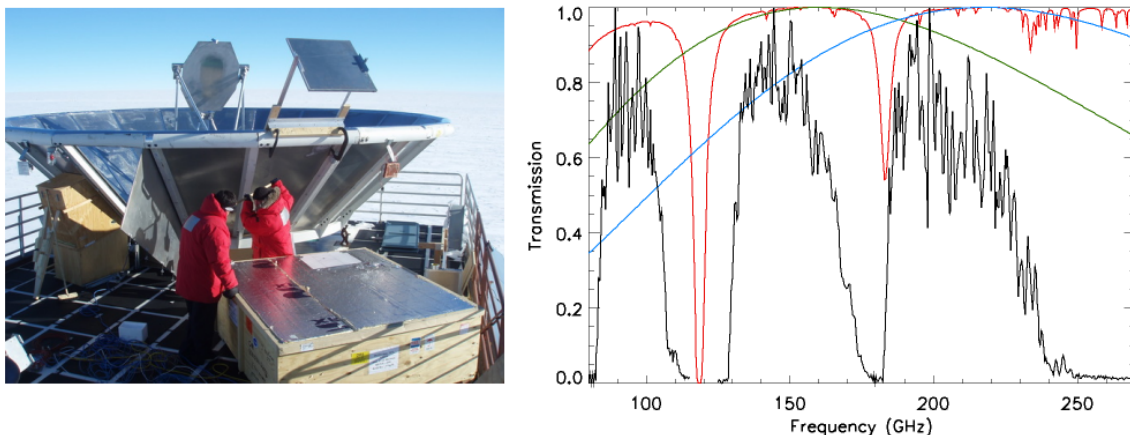
Figure 3.3: The BICEP spectra were measured at the South Pole with a Martin-Puplett FTS (left), which was placed on the roof of DSL inside an insulated box. Two flat mirrors were used to direct the FTS output into the telescope. The average spectra for BICEP's three pass bands are plotted in black on the right, along with the atmospheric transmission (red), CMB spectrum (green), and its temperature derivative (blue).

ground shield, and the output was directed into the telescope with two flat mirrors (see Figure 3.3). The spectra were measured one PSB pair at a time by moving the telescope mount to point each beam at the mirror above the FTS output port.

The spectra for each frequency band are, in general, similar across the focal plane and have consistent edge definitions. The average 100, 150, and 220-GHz spectra are plotted in Figure 3.3, along with a model of the atmospheric transmission at the South Pole. The median measured spectral mismatch within pairs corresponds to differential gain levels of 0.3% and 0.8% at 100 and 150 GHz. Outside of the main band, we have also examined the spectral responses for high frequency leaks caused by the filter stacks. The leaks were characterized by placing thick grill filters (with cut-off frequencies of 165 and 255 GHz) at the telescope aperture and and measuring the detector responses to a chopped source. No leaks were detected in the 150 GHz channels down to the noise floor at -35 dB, while the 100 GHz channels exhibited small leaks at -25 dB. Because the leak amplitudes are small and well matched within PSB pairs, the effect on relative gain mismatch is expected to be negligible.

3.4 Pointing

The two components of detector pointing reconstruction are telescope boresight pointing and detector offsets relative to the boresight (focal plane coordinates). Appendix A describes in detail how detector coordinates on the sky are calculated from boresight pointing and focal plane offsets.

The raw azimuth, elevation, and deck timestreams for the telescope boresight are obtained from encoders located on the three mount axes. The raw pointing is corrected with an offline pointing model, which contains five terms describing the azimuth and elevation encoder zeros, magnitude and direction of the azimuth axis tilt, and the tilt of the elevation axis relative to the azimuth axis. These pointing model parameters are measured every two days with star observations from the optical camera located on the top surface of the cryostat. During each pointing calibration procedure, the telescope points at a series of 24 stars at boresight orientation angles of -45°, 45°, and 135°. The azimuth and elevation offsets that are required to center the stars are fit to the pointing model, and the typical fit residuals are 10–12″ rms. A detailed description of how to apply the pointing model corrections to the raw boresight pointing is given in Appendix B.

The focal plane coordinates are obtained from measurements of the CMB temperature fluctuations using a map cross-correlation procedure. First, the nominal detector locations are used to generate flat sky single-detector maps at each deck angle, as well as a coadded map using all data. Each single-detector map is cross-correlated with the full coadded map to obtain image offsets. The offsets (after appropriate rotation) are averaged over the deck angles for each detector, and the focal plane coordinates are updated with these offsets. The map-making and offset calculation are repeated until the focal plane coordinates converge. The resulting uncertainty in the detector locations is 1.7′ rms.

For BICEP, the CMB temperature fluctuations are more effective than celestial objects for measuring detector locations. The moon and planets are below BICEP's elevation range, and RCW 38 is visible to only part of the focal plane. The only
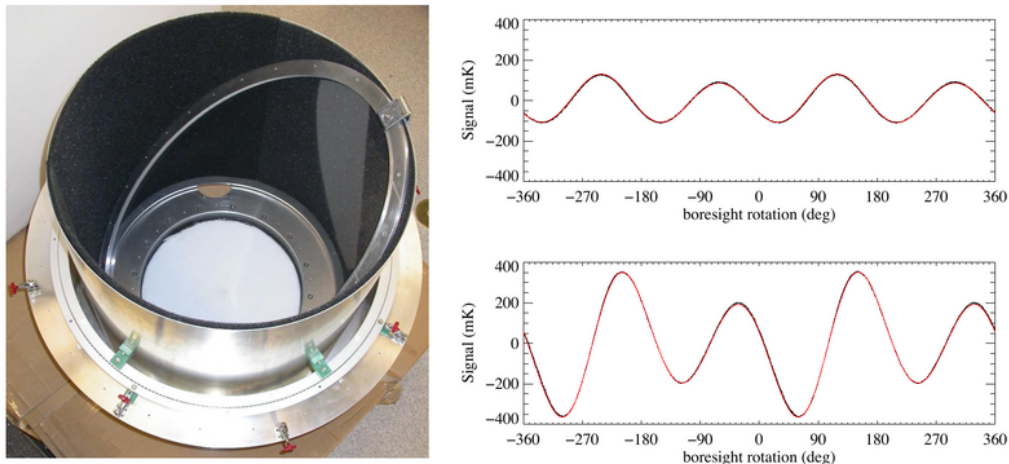
Figure 3.4: The dielectric sheet calibrator (DSC), pictured on the left, consists of a polypropylene sheet mounted at 45° in an eccosorb-lined cylinder. The DSC is kept fixed above the BICEP window while the telescope rotates in boresight, and two example detector responses are plotted on the right. The upper and lower plots show PSB pairs 4.1° and 8.5°, respectively, off-axis from the boresight. The data are black, and model fits are red. For these measurements, the PSBs in a pair are differenced to remove common-mode atmospheric fluctuations.

bright, accessible, compact source is Eta Carinae; however, fairly long integrations are required to achieve sufficient signal-to-noise. The uncertainty in the focal plane coordinates from Eta Carinae observations is about 2′, which is slightly worse than the uncertainty in the CMB cross-correlation method.

3.5 Detector polarization orientation angles

The detector polarization orientation angle ψ, projected on the sky and referenced to the meridian, is needed to solve Equation 3.1 for Q and U. It is convenient to define another detector orientation angle χ that is referenced within the focal plane, which provides a natural coordinate system for calibration apparatus. For a detector at a focal plane location (r, θ), the angle χ is defined relative to the radial vector so that the polarization orientation in focal plane coordinates is $\chi + \theta$. For a discussion of the relationship between χ and ψ, see Appendix A.

The primary device for measuring χ is a dielectric sheet calibrator (DSC), which is modeled after the calibrator employed by the POLAR experiment [31]. The DSC, as shown in Figure 3.4, consists of an eccosorb-lined cylinder that contains a polypropylene sheet mounted at $45°$. The polypropylene acts as a partial beam splitter and creates a small polarized signal

$$P_{\mathrm{DSC}} \approx (T_H - T_C)(R_{\mathrm{TE}} - R_{\mathrm{TM}}) \cos 2(\phi_{\mathrm{DSC}} - \chi - \theta) \tag{3.4}$$

that is proportional to the temperature difference $T_H - T_C$ between the eccosorb and the sky. The polarization arises from the reflectance difference $R_{\mathrm{TE}} - R_{\mathrm{TM}}$ perpendicular (TE) and parallel (TM) to the plane of incidence of the dielectric sheet, and the direction is determined by the angle ϕ_{DSC} of the DSC relative to the detector. The DSC is mounted above the BICEP window and is kept fixed while the telescope rotates in boresight. Detectors that are close to the boresight, as shown in the upper-right panel of Figure 3.4, have a nearly sinusoidal response, while off-axis detectors exhibit more complex behavior. Model fits, which account for off-axis effects, agree well with the data. The DSC measurements of individual PSB orientation angles are repeatable within $0.3°$ rms, and we find that PSBs in each pair are orthogonal within $0.1°$. The uncertainty in the absolute orientation of each PSB is $\pm 0.7°$, limited by the ability to determine the orientation of the dielectric sheet relative to the focal plane.

3.6 Cross-polar leakage

The cross-polar leakage ϵ describes the response of a PSB to orthogonally polarized light. Note that ϵ is a property of the detector itself and is independent of the cross-polar beam, which is a property of the optical chain upstream of the PSB. (For BICEP, ϵ dominates over the cross-polar beam.) The cross-polar leakage is measured by sending chopped, 100% polarized light into the telescope at several different orientation angles with respect to the detectors. The demodulated detec-
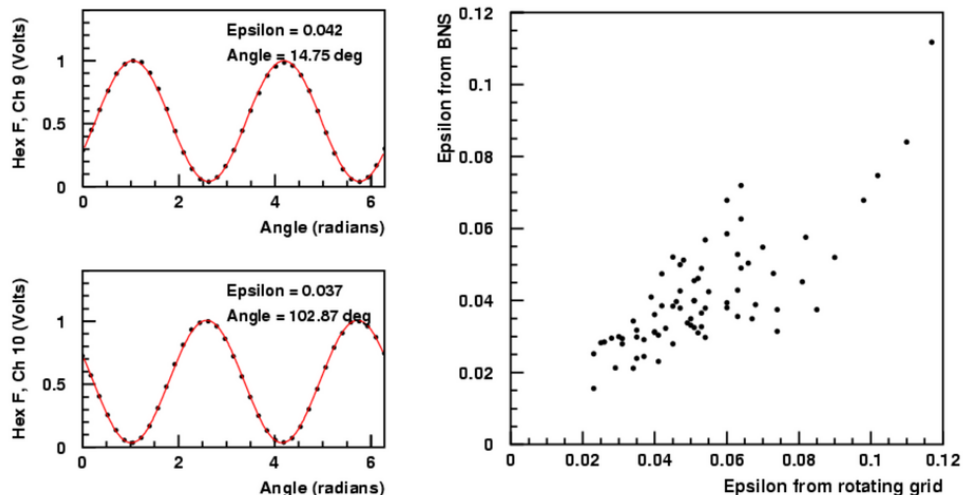
Figure 3.5: The left pair of panels show example data (black points) for two orthogonal PSBs from a rotating wire grid measurement. A fit to Equation 3.5, shown in red, yields the ϵ and orientation angle values listed in the plots. The values of ϵ obtained with the rotating grid and the BNS are compared in the scatter plot on the right. The two measurements are reasonably well correlated, although the ϵ values from the BNS are lower by about 0.01 on average.

tor signal d_i for each source orientation ϕ_i is

$$d_i = A \cos 2(\phi_i - \chi - \theta) + d_0, \tag{3.5}$$

where A is the amplitude, d_0 is the signal offset, and the phase $\chi + \theta$ is the detector orientation angle in focal plane coordinates. The cross-polar leakage is given by the ratio of the minimum and maximum responses, $\epsilon = (d_0 - A)/(d_0 + A)$.

BICEP uses two devices, a rotating wire grid and a linearly polarized broadband noise source (BNS), to measure ϵ in two different ways. The first device consists of a wire grid mounted on a rotating stage with an eccosorb-covered chopping blade, and the entire assembly is placed on the telescope window so that the chopped signal alternates between sky and ambient temperatures. The telescope is stationary while the grid slowly rotates, and Figure 3.5 illustrates example demodulated timestreams for two PSBs in a pair.

The BNS consists of a PIN-switched noise diode with a standard gain horn

mounted on the end, and a wire grid is placed in front of the horn to ensure 100% polarized output. Unlike the rotating grid source, the BNS produces high-power output that is visible in the far field of the telescope. For ϵ measurements, the BNS is placed on top of a mast on the MAPO roof so that the source is at an elevation of $2°$ (Figure 3.8). A flat mirror is mounted above the telescope to direct the signal into the aperture. The BNS source is held fixed, and the telescope scans "mini rasters" over each detector at many deck angles; the amplitude variations of the resulting mini beam maps as a function of deck angle are used to calculate ϵ. A scatter plot comparison of ϵ values obtained with the BNS and rotating grid sources is shown in Figure 3.5. The median ϵ values from BNS and rotating grid measurements are 0.04±0.01 and 0.05±0.02, respectively. The measurements of χ have also been confirmed with these two devices, although higher accuracy and precision are achieved with the DSC.

3.7   Beam characterization

The co-polar and cross-polar beams, $P_\parallel(r, \nu)$ and $P_\perp(r, \nu)$, describe the spatial response of an optical system to incoming light that is polarized parallel and perpendicular to the detector's axis of sensitivity. Given a 100% polarized source, aligned with one PSB in a pair so that $I = Q$, we can simplify the integrand in Equation 3.1 and express the response of the PSB pair as

$$d_\parallel \approx Q(P_\parallel + \epsilon P_\perp) \approx QP_\parallel \tag{3.6}$$

$$d_\perp \approx Q(\epsilon P_\parallel + P_\perp) = QP_\parallel \cdot (\epsilon + \frac{P_\perp}{P_\parallel}). \tag{3.7}$$

The PSB that is aligned with the source polarization sees a signal $d_\parallel$ that is proportional to the co-polar beam. In the limit that $\epsilon \gg P_\perp/P_\parallel$, the signal $d_\perp$ from the orthogonal PSB is also proportional to the co-polar beam, suppressed by a factor of ϵ. This limit applies in BICEP, where $\epsilon \sim 10^{-2}$ and $P_\perp/P_\parallel \sim 10^{-5}$ (obtained from physical optics simulations and confirmed by beam measurements). We therefore
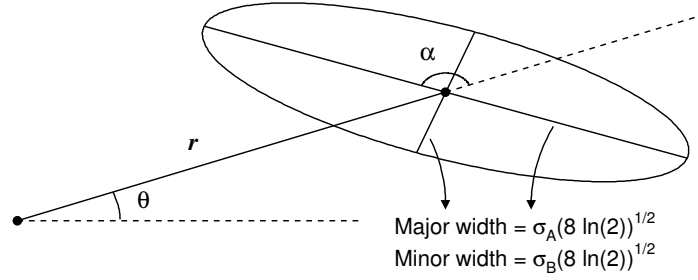
Figure 3.6: Variables used to describe a Gaussian beam. The centroid coordinates are r and θ (relative to the telescope boresight), the major and minor full widths are $\sqrt{8\ln(2)}\sigma_A$ and $\sqrt{8\ln(2)}\sigma_B$, and α is the tilt angle between the radial vector and the major axis.

ignore $P_\perp$ and characterize only $P_\parallel$.

The BICEP optics are designed to produce $0.95°$ and $0.63°$ Gaussian beams (100 and 150 GHz, respectively) over a $17°$ instantaneous field of view. As shown in Figure 3.6, the BICEP beams are modeled as elliptical Gaussians and characterized by five parameters: two coordinates (r, θ) that give the centroid location, a major and minor sigma (σ_A, σ_B), and a tilt angle (α). The centroid coordinates are measured relative to the telescope boresight. The angle θ is referenced $90°$ from the meridian when the boresight angle dk is zero, and θ increases counterclockwise looking at the sky. The tilt α describes the angle between the radial vector and the major axis.

PSB pairs are differenced to recover polarization information, so it is useful to characterize beam mismatches within PSB pairs that potentially create systematic errors in polarization. We define the following differential beam quantities:

- Differential beam size: $2(\bar{\sigma}_1 - \bar{\sigma}_2)/(\bar{\sigma}_1 + \bar{\sigma}_2)$

- Differential pointing: $2(\vec{r_1} - \vec{r_2})/(\bar{\sigma}_1 + \bar{\sigma}_2)$

- Differential ellipticity: $(e_1 - e_2)/2$

The subscripts (1,2) denote the two PSBs in a pair, the average sigma $\bar{\sigma}_i$ is given by $[(\sigma_A)_i + (\sigma_B)_i]/2$, and ellipticity is defined as $e = (\sigma_A - \sigma_B)/(\sigma_A + \sigma_B)$.
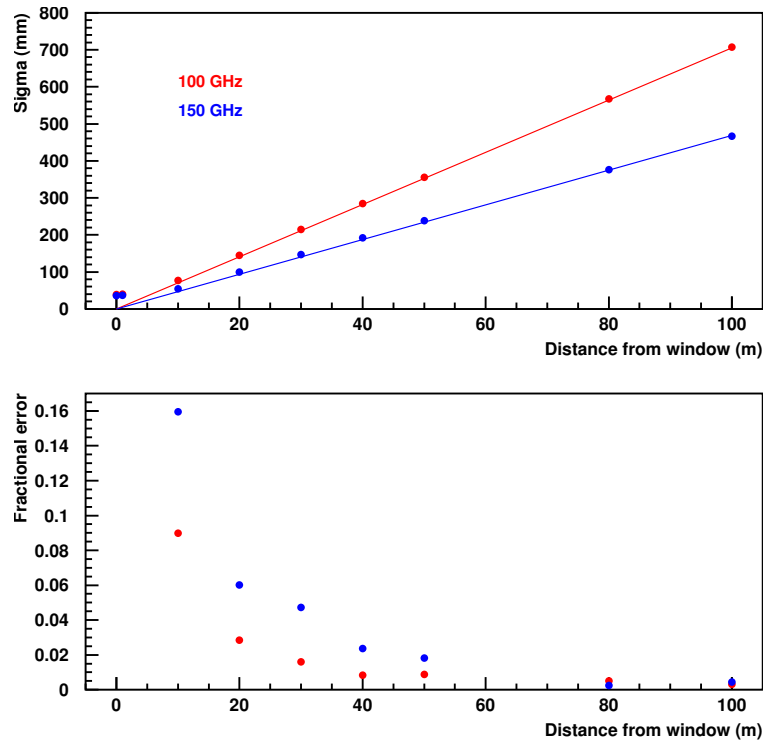
Figure 3.7: The upper panel shows the calculated beam width as a function of distance from the telescope window. The red and blue points correspond to 100 and 150 GHz, respectively, and the lines indicate the beam widths as given by the far field angle. The lower panel shows the fractional difference between the actual and far field beam widths. At a distance of 50 meters, the fractional difference is below 2% for both frequencies.

3.7.1 Beam measurements

The BICEP beams were mapped by raster scanning the telescope over a bright source at various fixed boresight angles. The far field of the telescope is about 50 meters from the aperture (see Figure 3.7), a convenient distance that permitted indoor measurements at Caltech and rooftop measurements at the South Pole. The beam mapping at Caltech was performed inside a high bay using a thermal source chopping between ambient temperature and a liquid nitrogen bath. At the South Pole, a 30-foot fold-over tower was installed on the roof of DSL, giving a line-of-sight distance of about 10 meters. An additional tower was installed on the roof of MAPO, at a distance of nearly 200 meters, and a flat mirror was temporarily

mounted above the BICEP window to direct the beams down to the low elevation of the tower (see Figure 3.8). The sources used at the South Pole included a thermal source chopping between ambient and sky temperature, the BNS, the moon, and Jupiter.

3.7.2 Analysis

In order to fit the beam data, a preliminary calculation is done to determine the azimuth/elevation coordinates (az_0, el_0) of the source as "seen" by the telescope boresight. This is done simply by fitting the center pixel centroids at several evenly spaced deck orientations and taking the average. Note that the center pixel is not necessarily in the same location as the boresight.

The source coordinates are subtracted from each boresight azimuth and elevation timestream sample (az, el), using the coordinate transformations

$$\tan(el') = \frac{-\sin(c)\sin(\beta)}{\cos(c)} \tag{3.8}$$

$$\cos(az') = \cos(c)/\sin(el'), \tag{3.9}$$

to produce source-subtracted boresight coordinates (az', el'). Here c and β are the distance and angle between (az, el) and (az_0, el_0):

$$\cos(c) = \sin(el_0)\sin(el) + \cos(el_0)\cos(el)\cos(az - az_0) \tag{3.10}$$

$$\cos(\beta) = \frac{\sin(el_0) - \cos(c)\sin(el)}{\sin(c)\cos(el)}. \tag{3.11}$$

To determine the beam center for one detector, the signal maximum is identified in the timestream, and a flat sky projection is done in a small window centered on the corresponding telescope coordinates (az'_{max}, el'_{max}):

$$x = \frac{\cos(el')\sin(az' - az'_{max})}{\cos(el')\cos(az')} \tag{3.12}$$

$$y = \frac{\cos(el'_{max})\sin(el') - \sin(el'_{max})\cos(el')\cos(az' - az'_{max})}{\cos(el')\cos(az')}. \tag{3.13}$$
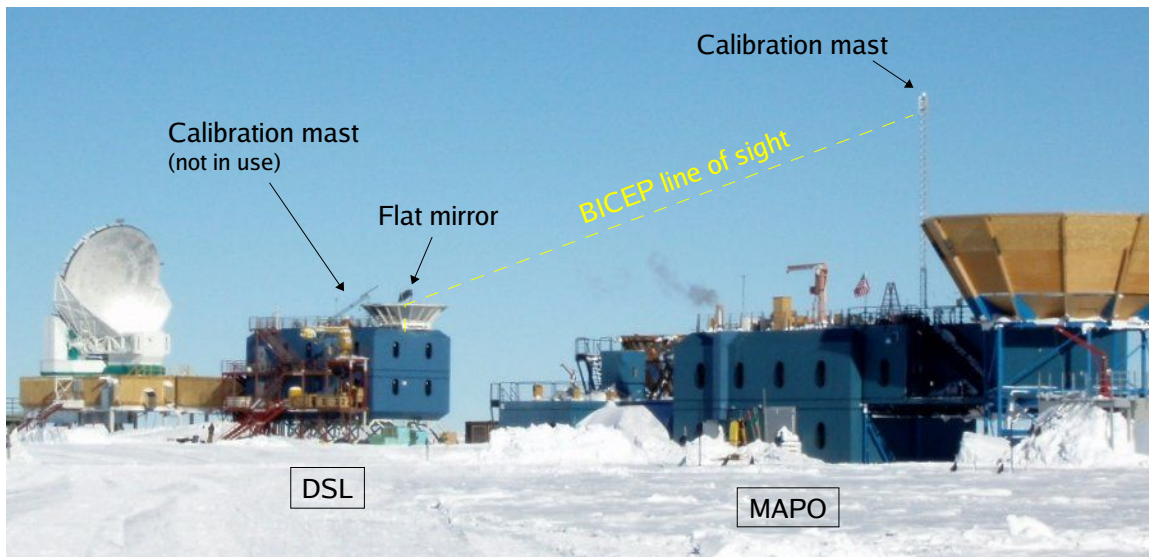
Figure 3.8: The BICEP beam mapping setup at the South Pole consisted of sources mounted at the top of fold-over towers. In this picture, BICEP is observing the MAPO tower, and a flat mirror is mounted above the telescope to direct the beams over the edge of the ground shield.

The detector timestream is binned in x and y, and the resulting map is fit to an elliptical Gaussian to obtain a centroid, major sigma, minor sigma, and tilt angle. The difference between the fitted centroid and the origin in the flat sky projection is used to correct the original estimate of $(\mathrm{az}'_{\mathrm{max}}, \mathrm{el}'_{\mathrm{max}})$. The focal plane coordinates (r,θ) are calculated from the distance and angle of $(\mathrm{az}'_{\mathrm{max}}, \mathrm{el}'_{\mathrm{max}})$ with respect to the azimuth/elevation origin (after accounting for the boresight orientation angle). The offset angle of the (r,θ) vector with respect to the local meridian is subtracted from the fitted tilt angle to obtain α.

The above equations ignore parallax corrections, which account for the displacement between the beam divergence point and the pivot point of the telescope mount (0.689 meter for BICEP). The correction factor is given by the ratio of this displacement to the distance between the pivot point and the source. Parallax corrections must be applied when the beam mapping source is close to the telescope, i.e., in all cases except celestial objects.
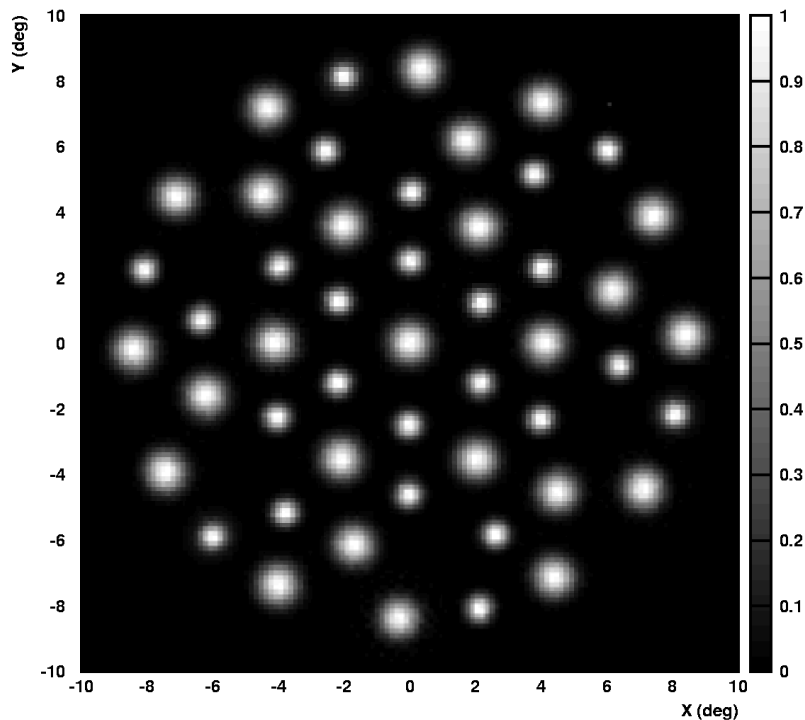
Figure 3.9: Beam maps from one detector in each PSB pair are combined to form this composite focal plane image. (The maps of the other detectors look similar.) The measurements were made with an unpolarized thermal source in the Caltech high bay, and the signal-to-noise in this image is about 100. The main beams are highly circular and have an average ellipticity of about 1%.

3.7.3   Main beams

Figure 3.9 shows a composite image of BICEP's focal plane from beam data taken in the Caltech high bay. The beams are well described by the Gaussian model, and fit residuals are typically about 1% with respect to the beam amplitude. The fitted centroids are repeatable to about $0.02°$ and agree well with the design locations. (Although the centroid precision from these beam maps is somewhat higher than the precision achieved with CMB cross-correlation in §3.4, the accuracy is limited by uncertainties in parallax and near-field corrections.) The average measured beam widths are $0.928°$ and $0.604°$ for 100 and 150 GHz, respectively (see Figure 3.10), about 3% smaller than the values predicted from physical optics simulations. The beam ellipticity is $<1\%$ for 100 GHz and about 1% for 150 GHz; the
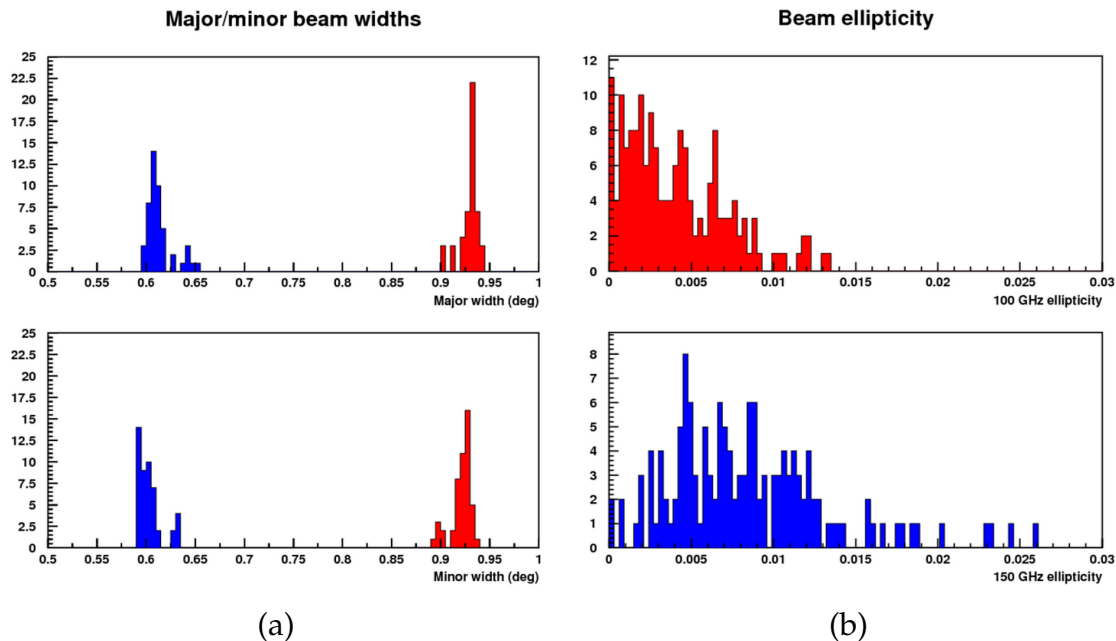
Figure 3.10: Panel (a) shows histograms of major and minor beam widths for 100 GHz (red) and 150 GHz (blue) channels. The small groups of outliers correspond to pixels that contained Faraday rotator modules in 2005–2006. Panel (b) shows histograms of the beam ellipticity measured at six different boresight angles for all detectors in both frequency bands.

near-roundness of the beams creates instabilities in the fitted tilt angles, which are generally not repeatable between maps taken at different boresight orientations.

A composite image of the differenced normalized beams for each PSB pair is shown in the left panel of Figure 3.11. The measurements were made with the BNS at the Pole, which is a bright microwave source that is ideal for probing low-level effects. The largest beam mismatch effect is a pointing offset that gives rise to dipole patterns in many of the differenced beams. The median dimensionless differential pointing $2|\vec{r_1} - \vec{r_2}|/(\bar{\sigma}_1 + \bar{\sigma}_2)$ is 1.3×10^{-2} (corresponding to a $\sim 0.004°$ offset on the focal plane[1]), and the right panel in Figure 3.11 illustrates that the offsets are highly repeatable between measurements at different boresight orientations. The measurement precision is 4×10^{-3}, determined by comparing differential

---

[1]The 0.004° differential pointing offset is smaller than the 0.02° centroid precision quoted previously. The reason for this difference is that 0.02° is the uncertainty in the absolute position of each detector pair; however, the relative pointing within a pair is measured with higher precision.
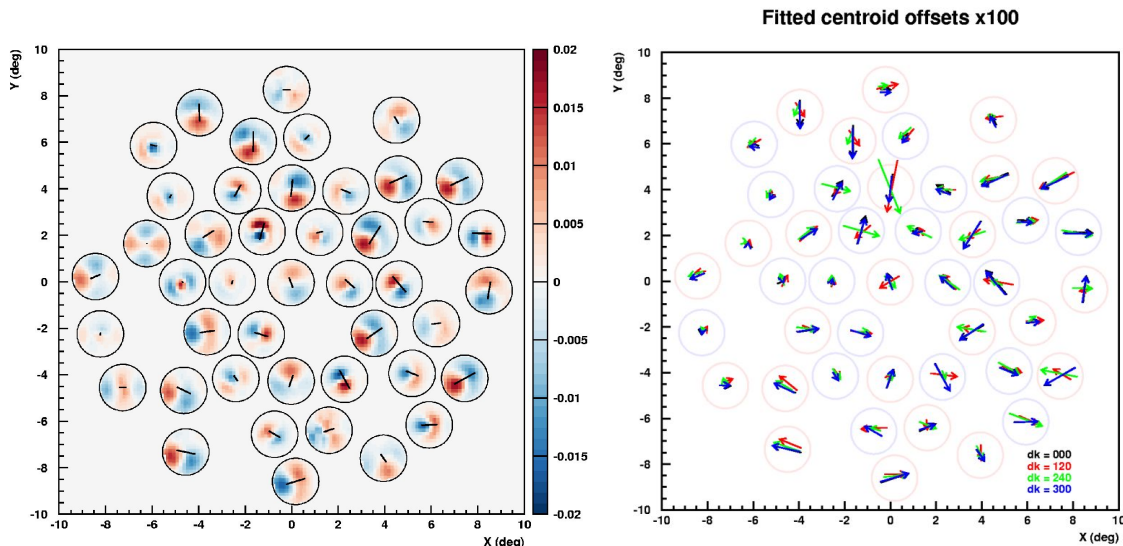
Figure 3.11: Beams for each PSB pair are normalized and differenced to produce a composite differential beam map (left). The overplotted lines show the fitted centroid offsets magnified by a factor of 100. In the right image, fitted centroid offsets from beam measurements at four different boresight angles (dk $= 0°, 120°, 240°, 300°$) are overplotted. The measured differential pointing is highly repeatable for most PSB pairs. The faint red and blue circles denote 100 and 150 GHz pixels.

pointing data from BNS and moon observations. In contrast to the pointing offsets, measurements of differential size and ellipticity are not repeatable, and the upper limits are 2×10^{-3} and 1×10^{-3}, respectively.

The differential pointing offsets, also known as "beam squint," are correlated with detector polarization angles, but the exact origin is unclear. Beam squint is predicted for offset reflector antennas measuring circular polarization [32], but no such prediction exists for linearly polarized systems (to the best of team BICEP's collective knowledge). The data are reasonably well described by a model in which the angle of the differential pointing vector is proportional to the polarization orientation angle χ of the front (or back) PSB. It is interesting to note that QUAD, which has a two-lens system coupled to a 2.64-m Cassegrain telescope, observes a similar pattern of pointing offsets [33] that more closely follows the model.
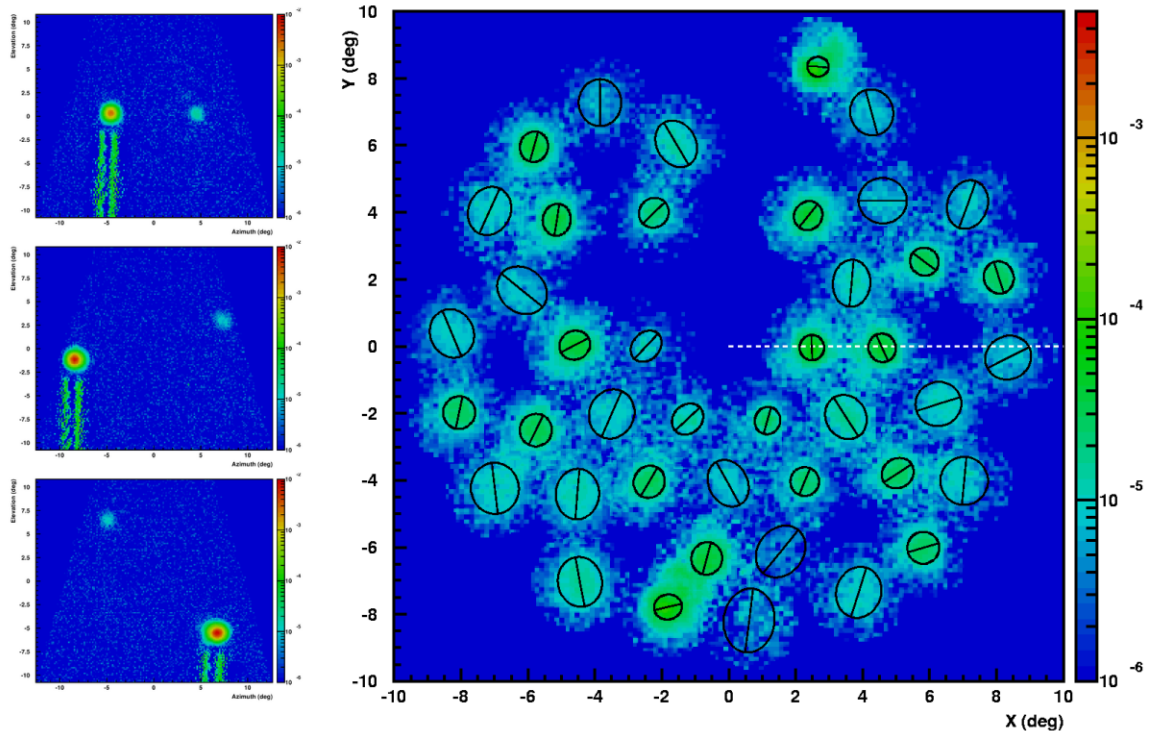
Figure 3.12: The left panels show South Pole beam maps for three selected channels where the signal is plotted in telescope boresight coordinates. Each main beam has a ghost image (a "little buddy") on the opposite side of the boresight. (The beam distortion is due to the choice of plotting coordinates, and the vertical streaks are reflections from the tower struts that leak into the demodulated signal.) The right panel shows a composite map of beam buddies mapped at a single boresight angle, and fits to elliptical Gaussians are outlined in black. The buddies directly above the center pixel are obscured by scattered light from the tower.

3.7.4 Ghost images and far side lobes

An unexpected feature of the BICEP optics is the presence of ghost images or "little buddies" paired with the main beams, as illustrated in Figure 3.12. Each buddy appears directly opposite of the main beam across the boresight, and the median amplitude with respect to the main beam is -24 dB and -22 dB for 100 and 150 GHz. The buddies are present for every channel in the focal plane except for the center pixel, and the symmetry of their locations suggests that the buddies are caused by few-percent reflections off the lenses and filters (Figure 3.13). This effect can be suppressed in a monochromatic instrument, where the antireflection coatings
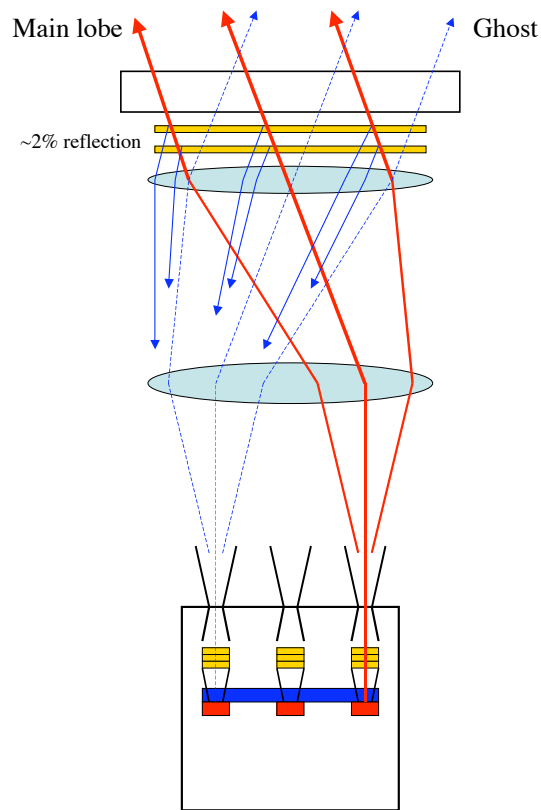
Figure 3.13: A possible explanation for the origin of the little buddies. The main beam (red lines) is partially reflected from the lenses and filters onto the opposite side of the focal plane, creating a ghost image (blue lines).

are optimized for a single frequency. Within each PSB pair, the buddies of both detectors are well-matched and are therefore expected to contribute negligibly to potential gain mismatches when the detectors are differenced.

The far side lobe response of BICEP was measured at the South Pole using a high-power PIN-switched Gunn oscillator mounted on top of the DSL tower. The telescope observed the source by stepping in elevation and rotating 360° about the boresight at every elevation step, thus radially building up the map. Measurements were made using several different source attenuation settings to achieve the dynamic range required to probe the main beam, which saturates at high power levels, and the faint side lobes. The side lobe maps are azimuthally averaged and

Figure 3.14: Side lobe maps are azimuthally averaged and combined to produce the left plot of side lobe power as a function of angle from the boresight. The performance of the reflective baffle is comparable to not using a baffle at all, but the absorptive eccosorb-lined baffle shows improved side lobe rejection at off-axis angles of $> 15°$. On the right, a pair-difference side lobe map is divided by pair-sum data to obtain fractional polarization.
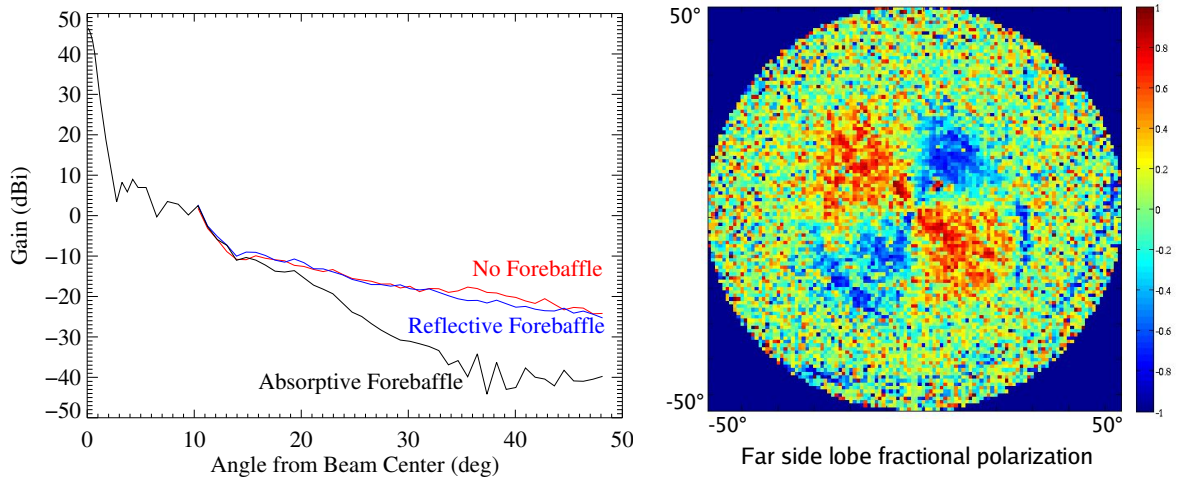
combined in Figure 3.14 (left plot), which compares measurement results with and without the baffle attached to the BICEP window. Past an angle of about 15° from the boresight, the eccosorb-lined baffle shows improved side lobe suppression over the reflective and no baffle cases.

The Gunn is polarized and can be used to measure fractional polarization of the far side lobes in addition to the total power. The right image in Figure 3.14 shows the ratio of a pair-difference and pair-sum map for one PSB pair. The fractional polarization has a quadrupolar pattern, and the amplitude of the variation is measured to be 10–50% for all pixels over an off-axis angle range of 10–20°. These data were taken with the absorptive forebaffle in place, and past 30° off axis, the quadrupolar pattern for most of the detectors is no longer visible above the noise floor. (Without the forebaffle on the telescope, the quadrupolar pattern is clearly visible out to the edge of the map.) Far side lobes potentially couple to emission from the Galaxy and ground, creating a false polarized signal. To assess the level of B-mode contamination, the polarized far side lobe response was convolved with

a dust model of the Galaxy and a model of varying snow accumulation on the ground screen. In both cases, the resulting false polarized signal was negligible (see Table 3.1).

3.8 Thermal stability

Temperature drifts in the focal plane and optics potentially create false polarized signals if they contaminate the differenced PSB timestreams within the signal band. The scan profile and boresight angles that are used for CMB observations (§2.10.1) have been chosen for minimizing thermal instabilities, and we characterize the response of the PSBs to thermal fluctuations under those operating conditions.

Focal plane temperature fluctuations are problematic if PSBs in a pair have mismatched thermal responsivities. For each bolometer, we measure the voltage change in response to a 10-mK temperature drop at the end of every refrigerator cycle. The median thermal responsivity is 0.8 $\mu\mathrm{K_{CMB}}/\mathrm{nK_{FP}}$, and the median mismatch within PSB pairs is 0.08 $\mu\mathrm{K_{CMB}}/\mathrm{nK_{FP}}$. The focal plane thermal fluctuations have a measured amplitude of 0.5 nK rms over 0.1–1 Hz, corresponding to a 0.04-$\mu\mathrm{K_{CMB}}$ spurious polarized signal.

Emission from the optics is expected to be unpolarized and, like instabilities in the focal plane temperature, is problematic only if the optical relative gains within PSB pairs are mismatched. Bolometer half-scans were averaged over a two month period and showed in-band fluctuations with only 0.7 $\mu\mathrm{K_{RJ}}$ amplitude.

3.9 Systematics and power spectra

Although we put forth our best efforts to characterize and calibrate BICEP, the measurement results always contain some amount of uncertainty. The impact of these uncertainties can be broadly separated into two categories: (1) systematic errors that contaminate the polarization data by mixing TT, EE, and BB, and (2) calibration uncertainties that affect only the scaling of the spectra. We are mostly

Parameter	Definition	Benchmark (r=0.1)	Measurement
Gain mismatch	$\frac{\Delta(g_1-g_2)}{(g_1+g_2)/2}$	0.5%	0.4%
Diff. beam size	$\frac{\bar{\sigma_1}-\bar{\sigma_2}}{(\bar{\sigma_1}+\bar{\sigma_2})/2}$	4%	< 0.2%
Diff. pointing[a]	$\frac{|\vec{r_1}-\vec{r_2}|}{(\bar{\sigma_1}+\bar{\sigma_2})/2}$	1.5%	1.3%
Diff. ellipticity	$\frac{e_1-e_2}{2}$	9%	< 0.1%
Absolute PSB pol. angle	$\Delta\psi$	4°	0.7°
Pol. side lobes to Galaxy[b]	-	-8 dBi	< -38 dBi
Pol. side lobes to ground[b]	-	-19 dBi	< -38 dBi
Cold stage temp. stability[c]	ΔT	1.3 nK	< 0.5 nK
Optics temp. stability[c]	ΔT_{RJ}	10μK	$< 0.7\mu$K

[a] The average differential pointing is 1.3% but has been repeatably characterized with 0.4% precision.

[b] At 30° off-axis with 20% polarized response in the side lobes.

[c] Scan-synchronous, over $30 < \ell < 300$.

Table 3.1: Potential systematic errors for BICEP. Each of these errors must be controlled such that the spurious BB polarization does not exceed 1×10^{-2} μK^2 at $\ell \sim 100$, the benchmark for probing $r = 0.1$.

concerned with the first category, particularly systematic errors that induce false B-mode polarization. Each systematic error must be sufficiently controlled so that the amplitude of any falsely created B-mode signal is well below the peak of the cosmological BB spectrum. For BICEP's target tensor-to-scalar ratio of $r = 0.1$, we define the initial benchmark to be equal to the corresponding BB amplitude, 1×10^{-2} μK^2 at $\ell \sim 100$. Table 3.1 summarizes the measurements of BICEP's systematic errors, described in the first part of this chapter, as well as the benchmarks for achieving the $r = 0.1$ goal. The calibration uncertainties that affect only the scaling of the spectra are summarized in Table 3.2, and we set the maximum allowed uncertainty in the spectrum amplitudes to be $\Delta C_\ell / C_\ell = 10\%$.

The calibration uncertainties that affect the spectrum amplitudes can be easily understood analytically. An error in the absolute gain measurement, for example, translates into a vertical scaling of the spectra that is proportional to $(g + \Delta g)^2$, so the gain uncertainty must be less than 5%. The impact of errors in ϵ and detector orientation angle ψ can be calculated from Equation 3.1. The simplified response

Parameter	Definition	Benchmark	Measurement
Absolute gain	$(\Delta g)/g$	5%	$< 5\%$
Cross-polar leakage	$\Delta\epsilon$	2.6%	2%
Relative PSB pol. angle	$\psi_{1,2} \pm \Delta\psi$	9°	0.3°

Table 3.2: Calibration uncertainties for BICEP. These errors affect the scaling of the spectra but do not leak temperature into polarization or cause EE–BB mixing. The benchmark for each of these uncertainties is set such that the error in the spectrum amplitudes is $\Delta C_\ell/C_\ell \leq 10\%$.

of a bolometer, ignoring the cross-polar beam terms, is

$$d \approx \frac{1}{2}g[I + \frac{1-\epsilon}{1+\epsilon}(Q\cos 2\psi + U\sin 2\psi)]. \tag{3.14}$$

An incorrect estimate of ϵ affects only the common amplitude of Q and U, while the relative amplitudes are unchanged. The effect on the spectra is, therefore, a simple scaling that doesn't mix EE and BB:

$$C_\ell^{EE} \quad \sim \quad (1-\Delta\epsilon)^2/(1+\Delta\epsilon)^2 \tag{3.15}$$

$$C_\ell^{BB} \quad \sim \quad (1-\Delta\epsilon)^2/(1+\Delta\epsilon)^2 \tag{3.16}$$

$$C_\ell^{TE} \quad \sim \quad (1-\Delta\epsilon)/(1+\Delta\epsilon). \tag{3.17}$$

(The temperature spectrum C_ℓ^{TT} is unaffected by ϵ.) The error on ϵ must be less than 2.6% in order to acheive an uncertainty in the EE and BB amplitudes that is no greater than 10%.

Ignoring cross-polar leakage effects and focusing on ψ, the response of an approximately orthogonal bolometer pair $d_{1,2}$ with a relative orientation uncertainty $\Delta\psi$ is

$$d_{1,2} = \frac{1}{2}g_{1,2}[I \pm (Q\cos 2(\psi \pm \Delta\psi) + U\sin 2(\psi \pm \Delta\psi))]. \tag{3.18}$$

The differenced detector signal is

$$\frac{d_1}{g_1} - \frac{d_2}{g_2} = \cos 2\Delta\psi(Q\cos 2\psi + U\sin 2\psi), \tag{3.19}$$

so an error in the relative angle affects the amplitude of Q and U in a manner similar to an error in ϵ. If, once again, we require the uncertainty on the EE and BB amplitudes to be less than 10%, then the relative angle uncertainty $\Delta\psi$ must be less than $9°$. A common mode error

$$d_{1,2} = \frac{1}{2}g_{1,2}[I \pm (Q\cos 2(\psi + \Delta\psi) + U\sin 2(\psi + \Delta\psi))], \qquad (3.20)$$

on the other hand, results in a differenced detector signal

$$\frac{d_1}{g_1} - \frac{d_2}{g_2} = (Q\cos 2\Delta\psi + U\sin 2\Delta\psi)\cos 2\psi + (U\cos 2\Delta\psi - Q\sin 2\Delta\psi)\sin 2\psi \quad (3.21)$$

that mixes Q and U. A co-rotation of the PSBs therefore causes leakage between the EE and BB spectra. The maximum leakage into BB is $\sin^2(2\Delta\psi) \cdot EE$, so at $\ell \sim 100$ where the EE amplitude is $0.7~\mu K^2$, the largest allowed $\Delta\psi$ uncertainty is about $3.4°$. This rough estimate is consistent with simulations, which predict that $\Delta\psi$ should be less than $4°$ to meet the $r = 0.1$ target.

Most systematic errors interact with the scan strategy in complex ways, and the exact effects on the power spectra can be computed only through simulations. An ensemble of simulated CMB skies is generated from a cosmological model using code such as synfast, and signal-only timestreams for all detectors are created from BICEP's actual pointing data. The simulations presented here use pointing data from eight nine-hour phases (B and C in Table 2.2, four of each) that span BICEP's entire CMB field at all four boresight angles. Systematic effects are added at the timestream generation step, and the timestreams are then filtered and binned back into maps. The power spectra of the BICEP-observed maps are compared with the input spectra, and any differences are attributed to the systematic errors. A particularly informative test is to use input spectra with $r = 0$ and to examine the output BB spectrum for power that has leaked from TT or EE.

The effects of many systematic errors can be understood by simulating relative gain mismatches. These systematics include transfer function errors, which act as

frequency-dependent gains, spectral mismatches, beam buddies, and, of course, relative gain errors themselves. Relative gain mismatches are simulated by inserting a randomly drawn Δg at the timestream generation step:

$$d_{1,2} = \frac{1}{2}(g \pm \Delta g)[I + \frac{1-\epsilon}{1+\epsilon}(Q\cos 2\psi + U\sin 2\psi)]. \tag{3.22}$$

Differential gains primarily leak temperature into polarization, and the brightness of the temperature fluctuations results in stringent requirements on Δg. The spectra from simulations of 10 relative gain distributions are shown in Figure 3.15. For these simulations, the gain errors are Gaussian distributed so that $\sigma(2\Delta g/g) = 1\%$, and the numbers are held fixed for the PSB pairs during each simulation of eight phases of data. The level of false BB depends strongly on how the gain errors are distributed in the focal plane, and the 100×150 BB cross-spectrum is sometimes even negative from anticorrelations in Δg. In the worst case, the false BB amplitude at $\ell \sim 100$ is $3.5 \times 10^{-2}\,\mu K^2$. The amplitude scales with $(\Delta g)^2$, so the differential gain error must be controlled to about 0.5% in order to achieve the $r = 0.1$ goal. Although this requirement is quite strict, it is also the worst case scenario from this set of simulations, and the other gain distributions show more cancellation effects that produce a smaller level of false BB.

Imperfections in the beams can alias temperature fluctuations into a false polarized signal and can cause EE–BB mixing. The coupling between beam systematics and the sky has been described in references [23; 34], and we follow the formalism of the latter for BICEP simulations. We model the beam as the sum of a symmetric Gaussian and a smaller, non-trivial, component with second moments of inertia σ_x and σ_y. A PSB timestream sample $d(\mathbf{p})$ that falls into a pixel centered at $\mathbf{p}$ is expressed as a convolution of the beam $P(\mathbf{r} - \mathbf{r}_b)$, which is centered at $\mathbf{r}_b$, with a second-order Taylor expansion of the sky signal around $\mathbf{p}$:

$$\begin{aligned}
d(\mathbf{p}) &= \frac{1}{2}\int d\mathbf{r}\, P(\mathbf{r} - \mathbf{r}_b)\Big[\big(I(\mathbf{p}) + \vec{\nabla}I(\mathbf{p})(\mathbf{r} - \mathbf{p}) + \frac{1}{2}(\mathbf{r} - \mathbf{p})^T D^2 I(\mathbf{p})(\mathbf{r} - \mathbf{p})\big) \\
&\quad + \cos 2\psi\big(Q(\mathbf{p}) + \vec{\nabla}Q(\mathbf{p})(\mathbf{r} - \mathbf{p}) + \frac{1}{2}(\mathbf{r} - \mathbf{p})^T D^2 Q(\mathbf{p})(\mathbf{r} - \mathbf{p})\big)
\end{aligned}$$

$$+ \sin 2\psi \Big(U(\mathbf{p}) + \vec{\nabla} U(\mathbf{p})(\mathbf{r} - \mathbf{p}) + \frac{1}{2}(\mathbf{r} - \mathbf{p})^T D^2 U(\mathbf{p})(\mathbf{r} - \mathbf{p}) \Big) \Big]. \quad (3.23)$$

In spherical coordinates, the derivatives are

$$\vec{\nabla} = \begin{pmatrix} \partial/(\sin \theta \partial \phi) \\ \partial/\partial \theta \end{pmatrix} \quad (3.24)$$

$$D^2 = \begin{pmatrix} \partial^2/(\sin^2 \theta \partial \phi^2) & \partial^2/(\partial \theta \partial \phi \sin \theta) \\ \partial^2/(\partial \theta \partial \phi \sin \theta) & \partial^2/\partial \theta^2 \end{pmatrix}. \quad (3.25)$$

If we define $m(\mathbf{p}) = I(\mathbf{p}) + Q(\mathbf{p}) \cos 2\psi + U(\mathbf{p}) \sin 2\psi$, then the zeroth and first order terms in Equation 3.23 are

$$\frac{1}{2} \Big[m(\mathbf{p}) + \vec{\nabla} m(\mathbf{p})(\mathbf{r}_b - \mathbf{p}) \Big], \quad (3.26)$$

and the second order terms are

$$\frac{1}{2} \int d\mathbf{r} \, P(\mathbf{r} - \mathbf{r}_b)(\mathbf{r} - \mathbf{p})^T D^2 m(\mathbf{p})(\mathbf{r} - \mathbf{p})$$

$$= \frac{1}{2} \mathrm{Tr} \Big[D^2 m(\mathbf{p}) \int d\mathbf{r} \, P(\mathbf{r} - \mathbf{r}_b)(\mathbf{r} - \mathbf{p})(\mathbf{r} - \mathbf{p})^T \Big]$$

$$= \frac{1}{2} \mathrm{Tr} \Big[D^2 m(\mathbf{p}) \int d\mathbf{r} \, P(\mathbf{r} - \mathbf{r}_b) \big((\mathbf{r} - \mathbf{r}_b)(\mathbf{r} - \mathbf{r}_b)^T + (\mathbf{r}_b - \mathbf{p})(\mathbf{r}_b - \mathbf{p})^T \big) \Big]$$

$$= \frac{1}{2} \mathrm{Tr} \Big(D^2 m(\mathbf{p}) \Big[R \begin{pmatrix} \sigma_x^2 & 0 \\ 0 & \sigma_y^2 \end{pmatrix} R^{-1} + \begin{pmatrix} (\Delta\phi)^2 & \Delta\phi\Delta\theta \\ \Delta\phi\Delta\theta & (\Delta\theta)^2 \end{pmatrix} \Big] \Big). \quad (3.27)$$

Here, R is a rotation matrix between the local beam coordinate system and the sky coordinates, and $\Delta\phi$ and $\Delta\theta$ are the longitude and latitude differences between the observation direction and the pixel center. The individual components of Equations 3.26 and 3.27 are written out explicitly in reference [34], and they are the expressions used by the BICEP code to simulate beam effects. The first and second derivatives of the I, Q, U maps are calculated by the synfast utility, which is part of the Healpix [35] package.

Although the exact impact of beam systematics on power spectra must be com-

puted from simulations, the couplings and scaling relations are apparent from Equations 3.26 and 3.27. To begin, we examine the effects of differential beam size, defined as $\beta_s = (\sigma_1 - \sigma_2)/\sigma$, where $\sigma_{1,2}$ are the beam sigmas of two PSBs in a pair, and their average is σ. Each beam is assumed to be round, so $\sigma_i = (\sigma_x)_i = (\sigma_y)_i$. Differential beam size couples to the second derivatives of the sky signal, and the effect on the power spectra scales with $\sigma^4 \beta_s^2$. Examining differential ellipticity $\beta_e = (e_1 - e_2)/2$ next, we consider two PSBs in a pair with the same average σ but different ellipticities such that $(\sigma_x)_{1,2} = \sigma(1 + e_{1,2})$ and $(\sigma_y)_{1,2} = \sigma(1 - e_{1,2})$. Like differential beam size, β_e also couples to the second derivatives of the maps, and the power spectra scale as $\sigma^4 \beta_e^2$. Finally, we consider the effect of differential pointing, $\vec{\beta}_p = 2(\vec{r_1} - \vec{r_2})/\sigma$. Unlike differential size and ellipticity, $\vec{\beta}_p$ is a vector quantity and couples to both the first and second derivatives of the sky signal with an amplitude that depends on the orientation angle of of the instrument. For example, if the instrument observes a sky pixel **p** such that $\vec{\beta}_p$ rotates by $180°$ between two observations, the spurious differential pointing signal reverses sign and cancels out. In contrast, the false polarization created by differential beam size and ellipticity does not have this cancellation property.

Simulations show that for BICEP's focal plane layout and scan strategy, it is necessary to control differential beam size, pointing, and ellipticity to 4×10^{-2}, 1.5×10^{-2}, and 9×10^{-2}, respectively, to meet the $r = 0.1$ goal. These simulations assumed uniform distributions of each parameter across the focal plane, and the differential pointing vectors were oriented radially. The beam measurements in §3.7 meet these benchmarks with the exception of differential pointing, which has a median magnitude of 1.3×10^{-2}. We have performed more exact simulations using actual measured $\vec{\beta}_p$ values (BICEP's differential pointing distribution is quite different from the radial model), and the results are illustrated in Figure 3.16. The false BB is largest at 150 GHz and has an amplitude of 1×10^{-2} μK^2 at $\ell \sim 100$, which is comparable to the $r = 0.1$ benchmark but well below the noise level of the initial two-year data set. Differential pointing may become a limiting factor in analyzing the three-year data set; however, the differential centroid offsets have

been measured with high precision, and it is possible to use those measurements to correct the maps. Figure 3.17 shows the results of simulations that use the measured beam widths, ellipticities, and tilts, which are noise dominated and should be regarded as upper limits. The false BB in these simulations is $4 \times 10^{-3} \ \mu\mathrm{K}^2$ at $\ell \sim 100$, which is safely below the $r = 0.1$ target. It is worth noting that this false BB is not necessarily entirely caused by differential beam size and ellipticity, since imperfect EE–BB separation in the power spectrum estimation contributes a false BB amplitude of about $3 \times 10^{-3} \ \mu\mathrm{K}^2$.
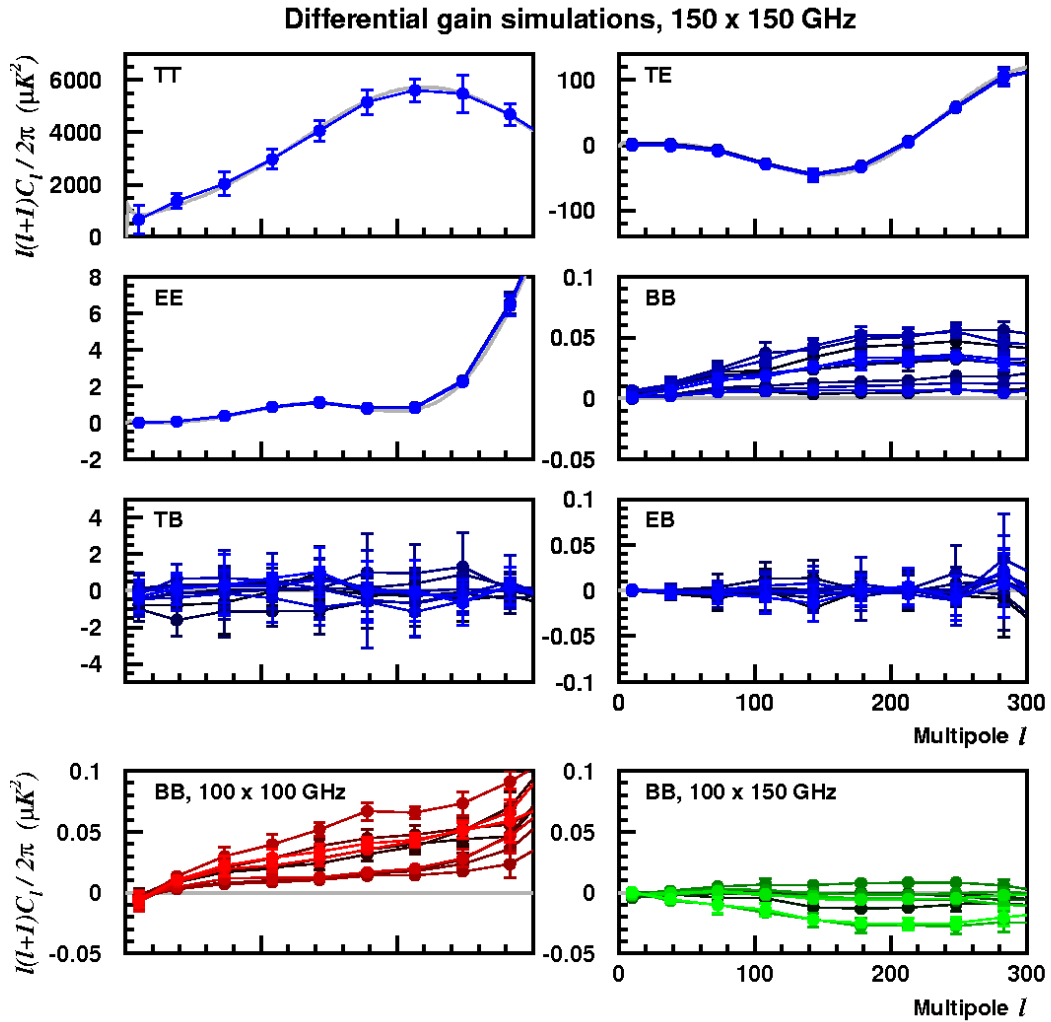
Figure 3.15: Spectra from 10 simulations of 1% relative gain mismatches. All six 150×150 GHz auto-spectra are shown, and the different shades of blue correspond to the 10 relative gain distributions. 10 input skies were used for each gain distribution, and the error bars denote the standard deviation over the inputs. The 100×100 and 100×150 GHz BB spectra are shown in the bottom two panels. The gray curves correspond to the input ΛCDM model with $r = 0$.

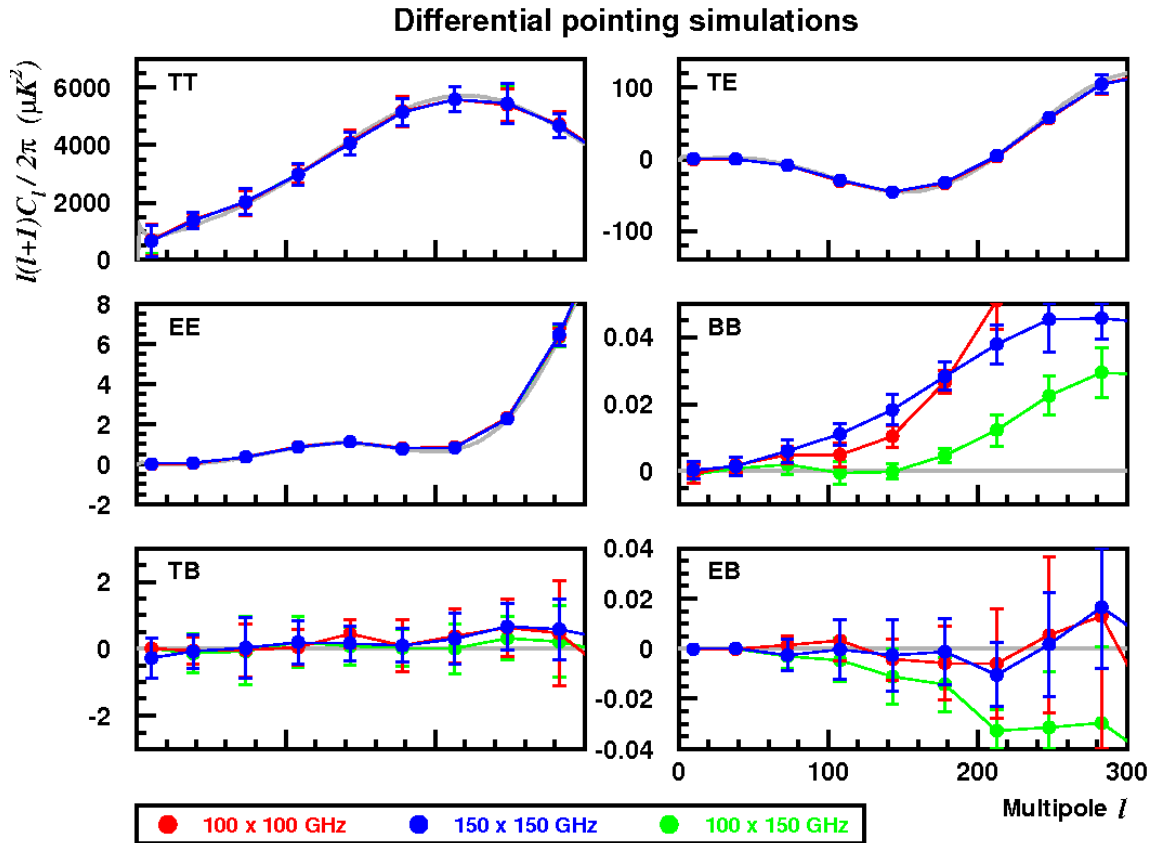Figure 3.16: Spectra from signal-only simulations that use BICEP's measured differential pointing parameters. The gray curves correspond to the input ΛCDM model with $r = 0$, and the error bars are the standard deviation over 10 simulations. The level of false BB created by differential pointing is below the noise level for the two-year data set, but it may become non-negligible for the three-year analysis.
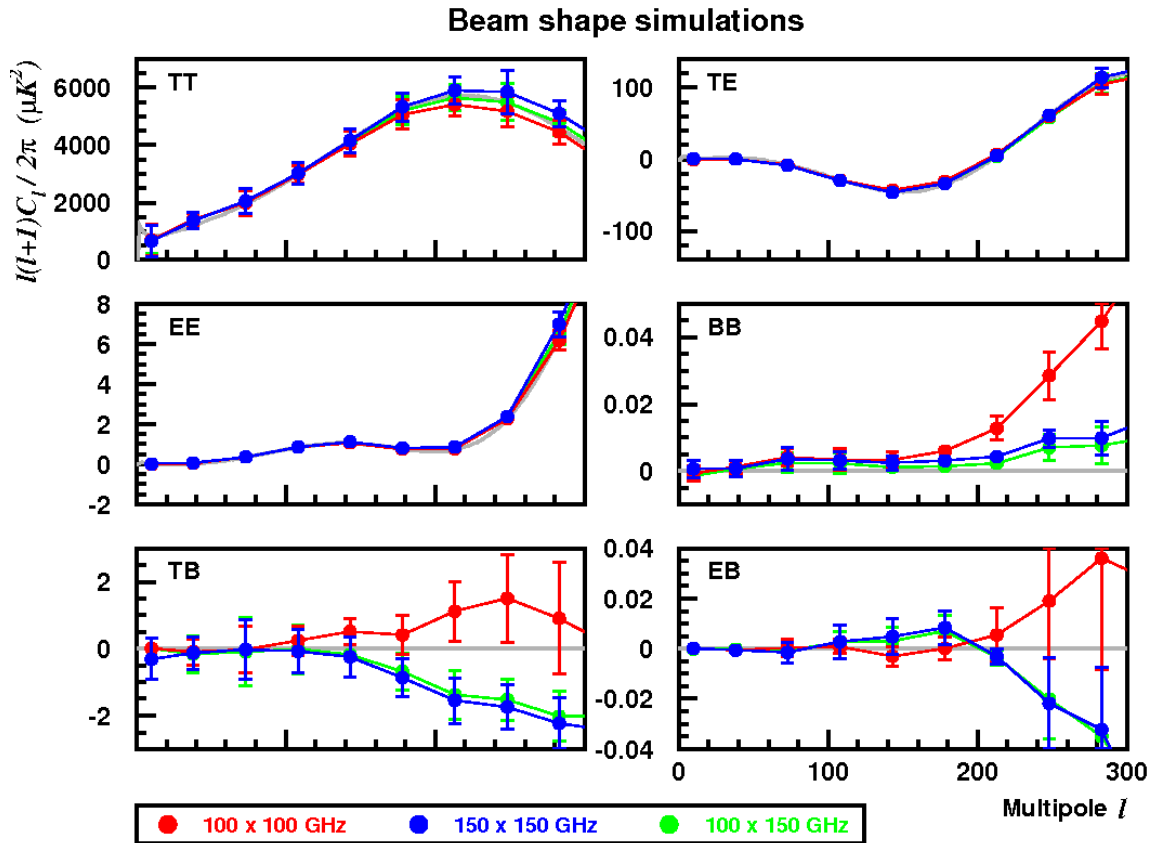
Figure 3.17: Spectra from signal-only simulations that use BICEP's measured beam widths, ellipticities, and tilts. Differential pointing is not applied here. The gray curves correspond to the input ΛCDM model with $r = 0$, and the error bars are the standard deviation over 10 simulations. The beam shape mismatches introduce false BB that is well below the $r = 0.1$ requirement.

Chapter 4

CMB data analysis

4.1 Data cuts

BICEP began taking CMB data in the late Austral summer of 2006 and will continue observing until November 2008, for a total of three seasons of operation. The analysis presented here includes data from the 2006 and 2007 observing seasons.

BICEP acquired a total of 360 complete 9-hour CMB observing phases in 2006 and 551 phases in 2007. The summer CMB data are generally of lower quality than the winter data because of several factors, including mediocre weather conditions, RF interference from LC-130 tranceivers, power plant tests, and summer riffraff (beakers and construction crew alike) stomping through the lab, slamming doors, removing structural beams, etc. Although BICEP is capable of observing during the summer—there is no evidence for sun contamination in the data—we restrict our analysis to winter data taken during February–November for the reasons cited above. The first 2.5 months of the 2006 winter data are also excluded from analysis because different scan strategies were used at the time, and we discovered excess RF pickup in the electronics boxes. This problem was solved by stuffing HR-10 into the RF shield surrounding the electronics and liberally applying aluminum tape on the outer surfaces. The summer and RF cuts reduce the BICEP data set to 249 and 495 9-hour phases for 2006 and 2007, respectively.

The data set is further reduced by cutting observation phases with extremely poor weather quality. For each phase, the standard deviation of relative gains from

elevation nods is calculated for each channel, and the median over the 100 and 150-GHz channels of those standard deviations yields two numbers per phase. An observation phase is cut if either of the median standard deviations is greater than 20% of the average relative gain. After weather cuts, the BICEP data set consists of 234 and 452 phases for the 2006 and 2007 seasons.

During initial timestream cleaning (§4.2), the data are split into "half-scans," or single constant-velocity sweeps in azimuth. Each detector half-scan is examined for glitches, and the results are recorded in a flag field so that problematic half-scans can be excluded from subsequent analysis. (Note that the timestreams are not gap-filled.) Each detector half-scan is subjected to three data quality checks. First, relative gains derived from elevation nods at the beginning and end of a set of scans are compared, and all of the half-scans in the scan set are flagged if the gains have drifted by more than 3%. The half-scans are also flagged if the fitting routine for the elevation nods returns an error. Second, gain-adjusted detector pairs are differenced for each half-scan, and the Gaussianity of the differenced timestream is checked by calculating the median-referenced skew and kurtosis. Detector pair half-scans are flagged if the magnitude of the skew is greater than 1.0 or if the magnitude of the kurtosis is greater than 1.5. Finally, half-scans that contain cosmic rays and other signal spikes are identified by looking for points that are greater than $7\times$ the standard deviation of the smoothed timestream. On average, the combined half-scan flagging criteria exclude about 3% of all half-scans over all light detectors.

Only the constant velocity sections of the telescope half-scans are used in analysis, and the azimuth turnarounds, where the speed falls below 2.6 deg/s, are discarded. This turnaround cut results in 25% data loss per half-scan. BICEP's total observing efficiency is 60% during CMB phases and 45% for each 48-hour cycle, after accounting for non-scanning periods, glitches, and turnaround losses.

Of the 98 light bolometer channels, several are excluded from each season for a variety of reasons, including no response (open channel), excess noise, poorly behaved or season-dependent transfer functions, and exceptionally poor polariza-

tion efficiency. The 2006 Faraday rotator pixels and 2007 220-GHz channels are also excluded from CMB analysis. If a single detector is flagged, its partner in the PSB pair is also flagged. A total of 38 100-GHz and 28 150-GHz channels are used for 2006 analysis, and 44 100-GHz and 30 150-GHz channels are used for 2007.

4.2 Low-level timestream cleaning

The raw output of BICEP consists of 50-Hz voltage timestreams for 144 channels, yielding a total of 2.5 terabytes of data for the first two observing seasons. The 144 channels comprise 98 light bolometers, 12 dark bolometers, 10 resistors, 16 thermistors, and 8 intentionally open channels. In the initial timestream cleaning, the raw data files are concatenated and trimmed for each observing phase, and low-level processing is performed on the timestreams. Complete transfer functions are deconvolved for the 98 light bolometers, and all timestreams are low pass filtered at 5 Hz and downsampled to 10 Hz. Half-scans are identified, and the indices are recorded. Each detector half-scan is examined for glitches, as described in §4.1, and the results are saved to disk as a bit mask. Relative detector gains are derived from elevation nods, and horizon and celestial boresight coordinates are calculated using the offline pointing model.

4.3 Mapmaking

After low-level cleaning, the bolometer timestreams are ready to be binned into maps. The simplified timestream output d_{ij} of a single PSB can be expressed as

$$d_{ij} = g_{ij}[I(p_j) + \gamma_i(Q(p_j)\cos 2\psi_{ij} + U(p_j)\sin 2\psi_{ij})], \tag{4.1}$$

where g is the gain, I, Q, U are the Stokes parameters of the sky signal, γ is the polarization efficiency factor ($\gamma \equiv (1 - \epsilon)/(1 + \epsilon)$, and ϵ is polarization leakage), and ψ is the PSB polarization orientation projected on the sky. The index i denotes

the PSB channel number, j is the timestream sample number, and p_j is the sky pixel observed at time j. The goal of mapmaking is to recover I, Q, U from the bolometer timestreams.

The mapmaking procedure for BICEP is taken from reference [36] and begins by forming gain-adjusted sum and difference timestreams for each PSB pair:

$$d_{ij}^{\pm} = \frac{1}{2}(d_{2i,j}/g_{2i,j} \pm d_{2i+1,j}/g_{2i+1,j}). \tag{4.2}$$

To reduce atmospheric $1/f$ noise, a third order polynomial is subtracted from the sum and difference timestreams for each half-scan in azimuth. If the effects of polarization leakage are neglected, Stokes I is recovered from the filtered sum timestreams with

$$\left(\sum_{i}^{\#\text{pairs}} \sum_{j \in p} w_{ij}^{+} d_{ij}^{+} \right) \Big/ \left(\sum_{i}^{\#\text{pairs}} \sum_{j \in p} w_{ij}^{+} \right) \simeq I(p), \tag{4.3}$$

where w^{+} is the weight assigned to each pair sum. In other words, the detector timestreams are simply binned into sky pixels. Stokes Q and U are calculated from linear combinations of the difference timestreams using the matrix equation

$$\sum_{i}^{\#\text{pairs}} \sum_{j \in p} w_{ij}^{-} \begin{pmatrix} d_{ij}^{-} \alpha_{ij} \\ d_{ij}^{-} \beta_{ij} \end{pmatrix} = \frac{1}{2} \sum_{i}^{\#\text{pairs}} \sum_{j \in p} w_{ij}^{-} \begin{pmatrix} \alpha_{ij}^{2} & \alpha_{ij}\beta_{ij} \\ \alpha_{ij}\beta_{ij} & \beta_{ij}^{2} \end{pmatrix} \begin{pmatrix} Q(p) \\ U(p) \end{pmatrix}. \tag{4.4}$$

Here, w^{-} is the weight assigned to each pair difference, and α, β are PSB pair orientation angle factors defined as

$$\alpha_{ij} = \gamma_{2i} \cos 2\psi_{2i,j} - \gamma_{2i+1} \cos 2\psi_{2i+1,j} \tag{4.5}$$

$$\beta_{ij} = \gamma_{2i} \sin 2\psi_{2i,j} - \gamma_{2i+1} \sin 2\psi_{2i+1,j}. \tag{4.6}$$

The 2×2 matrix in Equation 4.4 is singular for a single pair of $\psi_{2i,j}$ and $\psi_{2i+1,j}$, and the equation can be solved only by accumulating more than one timestream sample in a given sky pixel p. As p is observed with many detector angles ψ, the
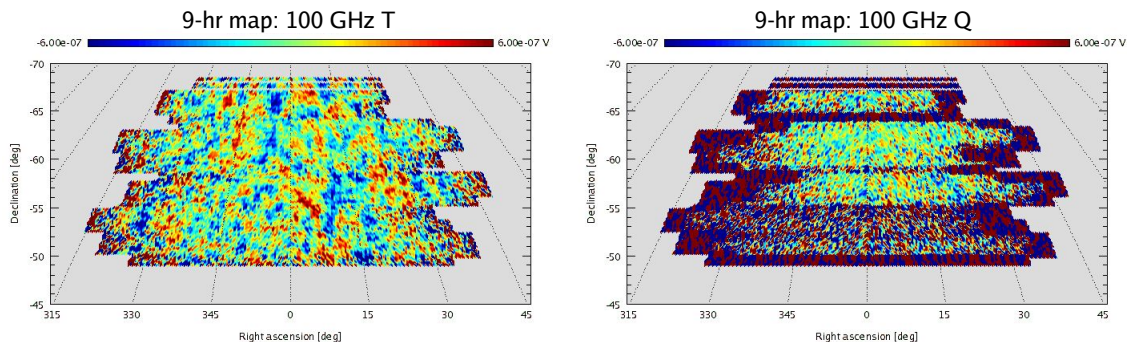
Figure 4.1: Example 100-GHz T and Q maps made from a single nine-hour observing phase. The temperature anisotropies are already visible in this small data set, allowing us to calibrate against WMAP on short time scales. Because the boresight angle is held fixed during each observation phase, the Q and U maps are poorly cross-linked after nine hours. Polarization information in a pixel on the sky is recovered when it is observed with at least two different angles.

off-diagonal $\alpha_{ij}\beta_{ij}$ terms average to zero, and the matrix becomes invertible (this is sometimes called cross-linking). Although only two different observation angles are required to invert the matrix, some instrumental systematics average down as the number of observation angles increases. Figure 4.1 shows example 100-GHz maps made from a single nine-hour observation phase, where the boresight angle is held fixed. The cross-linking is poor during an individual phase, as illustrated by the large number of saturated pixels in the Q map, so we rely on observations at more than one boresight angle in order to recover polarization information. By examining the determinant or condition number of the 2×2 matrix, poorly cross-linked pixels can be identified and masked from analysis.

We choose the pair sum and difference weights $w^{\pm}$ to be proportional to the inverse variance of the timestream noise. The weights are evaluated over each set of azimuth scans (every 50 minutes), a period during which the noise properties are approximately stationary. For each channel pair, the sum/difference weight for a scan set is calculated from the average value of the auto-spectrum between 0.5 and 1 Hz. (The spectra are read from the noise model, which is described in §4.4.2.)

4.4 Power spectrum estimation

With T, Q, U maps in hand, the next data analysis step is turning those maps into power spectra. We follow the MASTER formalism [37], which is a power spectrum estimation technique that relies on Monte Carlo simulations of signal and noise. The raw spherical harmonic transform (SHT) or "pseudo-C_ℓ" spectrum of a map is denoted $\hat{C}_\ell$ and is related to the true underlying power spectrum C_ℓ through the relationship

$$\langle \hat{C}_\ell \rangle = \sum_{\ell'} M_{\ell\ell'} F_{\ell'} B_{\ell'}^2 \langle C_{\ell'} \rangle + \langle \hat{N}_\ell \rangle. \tag{4.7}$$

Here, $M_{\ell\ell'}$ is the mode-mode coupling kernel, F_ℓ is the ℓ-space transfer function due to timestream filtering, B_ℓ is the beam transfer function, and $\hat{N}_\ell$ is the noise bias. BICEP uses two independent analysis pipelines for power spectrum estimation: the first is a flat-sky estimator that evaluates Equation 4.7 using 2D Fourier transforms, and the second performs a curved-sky analysis using Spice [38], which is a publicly available code for solving Equation 4.7. This thesis focuses on the latter of the two pipelines.

Before launching into the details of power spectrum estimation and simulations, it is useful to take a step back and examine where we're going with Equation 4.7. Figure 4.2 illustrates the goal of power spectrum estimation with a simple map-space cartoon. Starting with the "truth," the real underlying CMB anisotropies, the first alteration of the signal by the instrument is blurring, caused by the telescope's finite resolution. An experiment like BICEP observes only a small portion of the sky, so the map is restricted to that observing region. The third-order polynomial filter that is used to subtract atmospheric $1/f$ noise also has the effect of removing the large-scale CMB signal. Finally, instrumental noise is added on top of the remaining signal. Comparing the first and final images, it is clear that what the telescope observes looks almost nothing like the "truth." The goal of power spectrum estimation, then, is to run these steps backwards: in other words, given a CMB observation that is contaminated by instrumental effects, produce the best possible estimate of the signal that lies underneath.
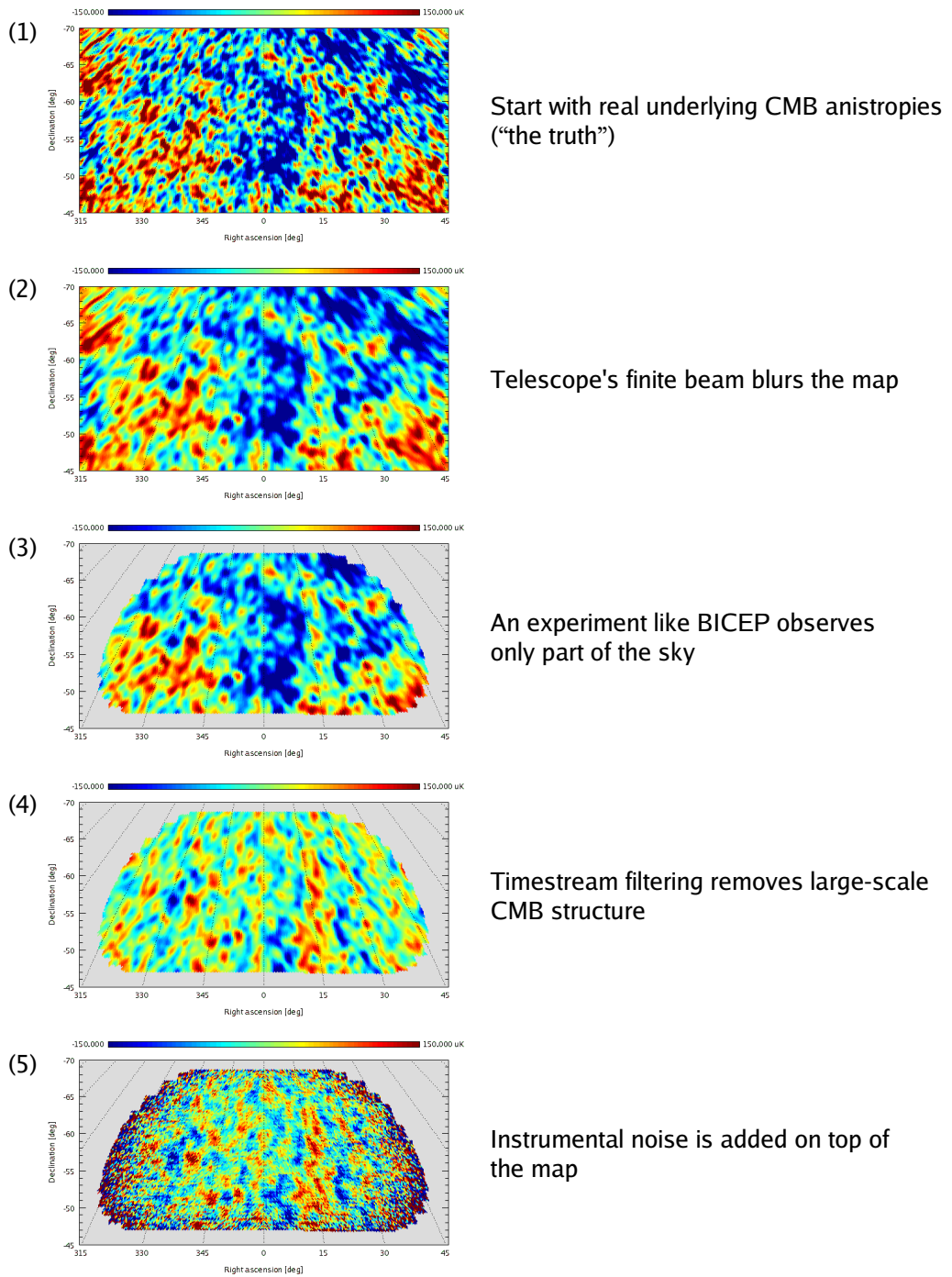
Figure 4.2: A map-space cartoon illustrating how an instrument's CMB observation is affected by the beam, observing region, filtering, and noise. Given a noisy, filtered observation (5), the goal is to produce the best possible estimate of the real power spectrum of (1).

4.4.1 The `Spice` framework

It is important to begin by discussing what `Spice` can and cannot do for you. The primary function of `Spice` is to calculate spherical harmonic transforms of maps, which are evaluated via two-point correlation functions, and to use those SHTs to solve Equation 4.7. Given temperature and polarization maps, `Spice` produces the full set of six auto- and cross-spectra: TT, EE, BB, TE, TB, and EB. The code accepts either one or two input maps and calculates the auto-correlation of the former and cross-correlation of the latter. Apodizing masks can also be supplied as input, and `Spice` calculates the mode-mode coupling that results from analyzing cut-sky maps. The BICEP polarization maps, which are noise-dominated, are apodized with a mask that is proportional to the amount of integration time per pixel, and edge pixels with poor cross-linking are excluded. The temperature maps have high signal-to-noise, and the mask is chosen to be proportional to the square root of integration time so that the weighting is reasonably flat across the map. Calculating power spectra from a map with partial sky coverage causes mixing between EE and BB (the EE amplitude is much larger, so we are mainly concerned with false BB created from leakage effects). `Spice` implements an EE/BB separation technique that removes the leakage exactly in the mean, and we find that for BICEP's sky coverage, the false BB amplitude from simulations of ΛCDM skies is about 3×10^{-3} μK^2 at $\ell \sim 100$.

There are three items in Equation 4.7, F_ℓ, B_ℓ, and $\langle \hat{N}_\ell \rangle$, that are specific to each experiment and cannot be computed by any off-the-shelf package. The beam measurements are described in §3.7, and for the analysis presented here, we approximate the 100 and 150-GHz beams as circular Gaussians with full widths of 0.928° and 0.604°, respectively. Differences between this idealized model and the actual B_ℓ are expected to impact the spectra at high ℓ, but the approximation is valid for $\ell < 300$. The filter function and noise bias are obtained through Monte Carlo simulations of the instrument, and error bars for the spectra are calculated from signal-plus-noise simulations.

Pair sum

Pair difference
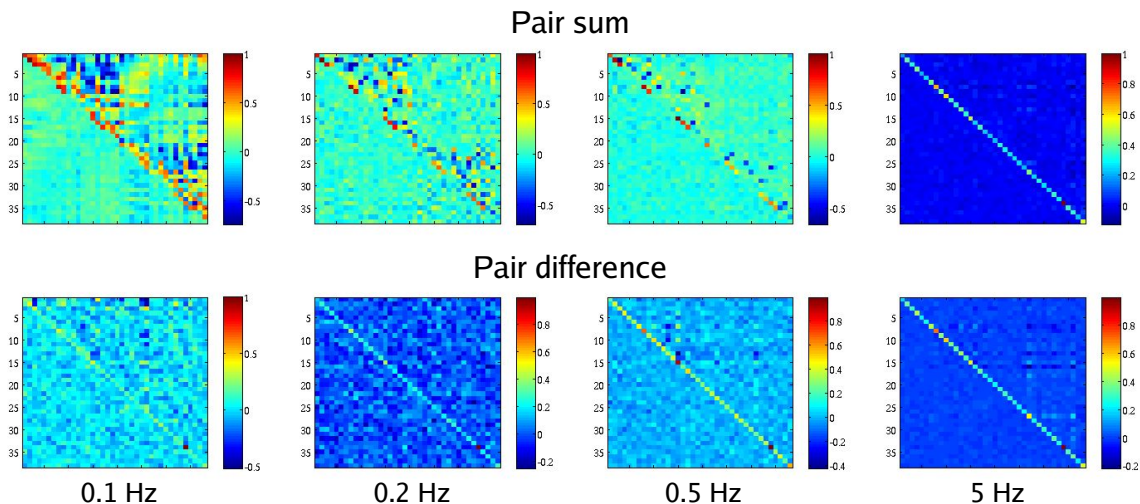

| 0.1 Hz | 0.2 Hz | 0.5 Hz | 5 Hz |

Figure 4.3: Example correlation matrices from the BICEP noise model. Each panel shows the cross-correlations between channel pairs, with the real and imaginary components plotted in the upper-right and lower-left triangles, respectively. The off-diagonal elements are normalized by the auto-correlation values, while the diagonal elements are not normalized. The upper and lower rows show pair sum and difference data; atmosphere-induced correlations are visible as off-diagonal structure in the pair sum matrices. The sum–difference correlations are not shown but are computed and used in the noise model. BICEP's noise model is evaluated in 12 frequency bins spanning 0.05–5 Hz, and four of those bins are illustrated here.

4.4.2 Noise model and simulations

The first step in solving Equation 4.7 is calculating and subtracting the noise bias $\langle \hat{N}_\ell \rangle$. The BICEP noise model is derived from the detector pair sum and difference timestreams, under the assumption that the timestream signal-to-noise (S/N) is negligible, i.e. the signal is the noise. This assumption is certainly safe for the difference timestreams, where the S/N is $\leq 0.1\%$. The S/N in the sum timestreams is about 3%, which is a tolerable level of error since the temperature measurement is not BICEP's primary science goal. (The noise model could be refined by subtracting a CMB template from the sum timestreams, but we leave this as an exercise for a future graduate student.) The gain-adjusted, polynomial-filtered pair sum and

difference timestreams are Fourier transformed

$$\tilde{\mathbf{d}}(f) \equiv \left(\tilde{d}_1^+(f), \tilde{d}_2^+(f), \ldots \tilde{d}_m^+(f), \tilde{d}_1^-(f), \tilde{d}_2^-(f), \ldots \tilde{d}_m^-(f)\right), \tag{4.8}$$

over each half-scan interval, and all auto-correlations and cross-correlations between channel pairs are computed to form the complex frequency-domain noise covariance matrix

$$\tilde{\mathbf{N}}(f) = \langle \tilde{\mathbf{d}}(f)\tilde{\mathbf{d}}^\dagger(f) \rangle. \tag{4.9}$$

The noise covariance matrix is calculated for each set of constant-elevation azimuth scans during observing, or every $\sim$50 minutes, a period during which the noise properties of the telescope are approximately stationary. The brackets denote an average over the 100 half-scans within each scan set. Each half-scan contains 200 timestream samples, so $\tilde{\mathbf{N}}(f)$ has 100 frequency points at the finest resolution. We average $\tilde{\mathbf{N}}(f)$ into 12 logarithmically spaced bins spanning 0.05–5 Hz, and the resulting set of matrices constitutes the BICEP noise model (Figure 4.3).

For the purpose of forming the noise model only, the pair sum and difference timestreams are gap-filled. This procedure is not performed during mapmaking; any detector half-scan with a glitch is simply excluded. Because the noise covariance matrices are constructed by averaging auto- and cross-spectra over many half-scans, excluding a half-scan for a single detector pair sometimes causes the matrices to become non-positive-definite. The simple solution to this problem, excluding a half-scan for *all* detectors if any of them contains a glitch, results in data loss of up to 70% for the noise model calculation. We therefore gap-fill when possible, and we reject a half-scan for all detectors if more than four PSB pairs display a simultaneous glitch.

To construct simulated correlated noise timestreams, we take the Cholesky decomposition $\tilde{\mathbf{N}}(\mathbf{f}) = \mathbf{L}(f)\mathbf{L}^\dagger(f)$ of the noise covariance matrix and multiply a vector of pseudo-random complex numbers $\mathbf{g}(f)$ by $\mathbf{L}(f)$:

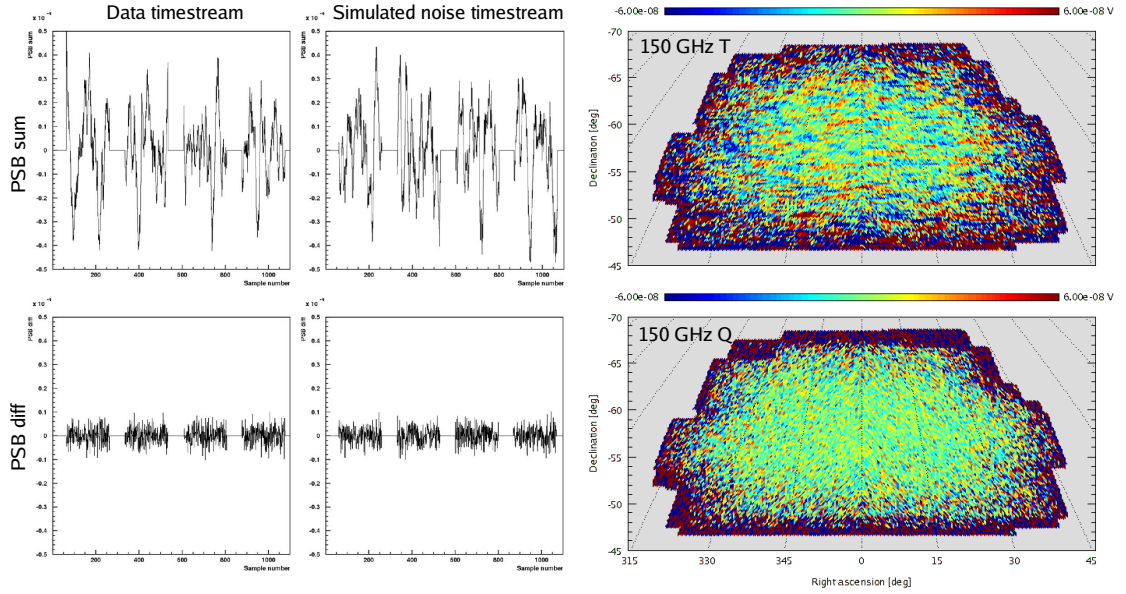$$\tilde{\mathbf{v}}(f) = \mathbf{L}(f)\mathbf{g}(f). \tag{4.10}$$

Figure 4.4: The left two columns show real and simulated noise-only timestreams for a PSB pair over four azimuth half-scans. The upper and lower rows are pair sum and difference data, respectively. The sum timestream displays significant $1/f$ atmospheric noise, which is successfully removed by PSB differencing, and the simulated timestreams reflect the noise properties of the data. Two-year coadded noise-only maps are shown in the rightmost column. The $1/f$ noise in pair sum timestreams appears as striping in the T map, while the Q map looks like white noise.

The complex numbers have Gaussian-distributed real and imaginary components and are normalized such that the amplitude has $\sigma = 1$. The resulting product $\tilde{\mathbf{v}}(f)$ has the same statistical properties as the data $\tilde{\mathbf{d}}(f)$ that were used to construct the noise model,

$$
\begin{aligned}
\langle \tilde{\mathbf{v}}(f)\tilde{\mathbf{v}}^\dagger(f) \rangle &= \langle \mathbf{L}(f)\mathbf{g}(f)\mathbf{g}^\dagger(f)\mathbf{L}^\dagger(f) \rangle \\
&= \mathbf{L}(f)\mathbf{L}^\dagger(f) \\
&= \tilde{\mathbf{N}}(f), \tag{4.11}
\end{aligned}
$$

and is inverse Fourier transformed to obtain a set of simulated noise timestreams. The timestreams are coadded into maps, and a few examples are illustrated in Figure 4.4.
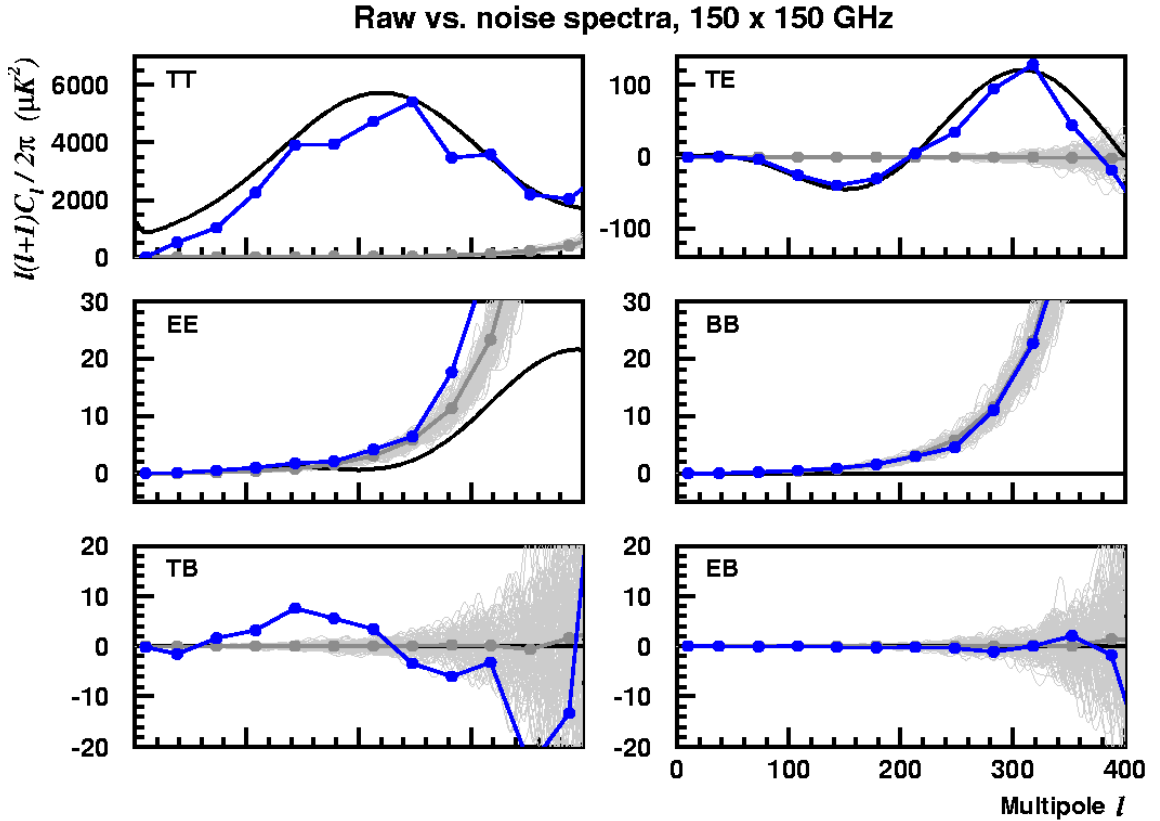
Figure 4.5: The first step in power spectrum estimation is correcting the raw spectra for noise bias. BICEP's raw 150 GHz auto-spectra are plotted in blue, noise spectra from 100 simulations are plotted in light gray, and the dark gray points are the average $\langle N_\ell \rangle$. The black curves correspond to a ΛCDM model. Noise estimation is particularly important for the EE and BB spectra, where the signal consists mostly of noise at high ℓ.

$\langle \hat{N}_\ell \rangle$ is estimated from an ensemble of simulated noise-only maps. The power spectra of each noise realization are averaged together, and the results from 100 simulations are shown in Figure 4.5, along with BICEP's raw 150 GHz auto-spectra. The TT and TE spectra are measured with high signal-to-noise, and the noise bias is nearly negligible up to $\ell = 400$. In contrast, the noise comprises the bulk of the signal in the EE and BB spectra, illustrating the need for careful noise modeling and subtraction. The noise from each half of the TB and EB spectra are mostly uncorrelated, so the resulting spectra are distributed around zero. The low-ℓ suppression of the spectra with respect to the ΛCDM model, which is most apparent

in TT, is caused by BICEP's timestream filtering. To correct for filtering effects, we use signal simulations to estimate F_ℓ.

4.4.3 Signal-only simulations

The signal simulation procedure begins with the generation of model cosmological power spectra using code such as CAMB. We use ΛCDM parameters derived from WMAP five-year data (Table 6 in [5]) and a tensor-to-scalar ratio of zero. From the model spectra, we use synfast to create an ensemble of simulated CMB skies. Equation 3.23 is then applied to the maps to create signal-only detector timestreams according to BICEP's scan strategy. Actual pointing data and measured PSB pair centroids, detector orientation angles, and cross-polar leakage values are included in the simulations. For the purpose of estimating F_ℓ, all differential beam systematic effects are turned off so that there is no mixing between temperature and polarization (the primary function of Equation 3.23 is producing a smoothly interpolated timestream from a pixellized map and its derivatives). The signal timestreams are filtered and weighted exactly as the data are processed and then coadded into maps. The ratio of the spectra of these "BICEP-observed" maps to those of the original input maps gives the transfer function F_ℓ. Panels 3 and 4 of Figure 4.2 show an example of a simulated CMB sky before and after BICEP-filtering. The timestream polynomial filtering that removes atmospheric $1/f$ noise also removes the largest modes in the CMB maps.

Figure 4.6 shows F_ℓ from 100 signal simulations using third-order polynomial timestream filtering. At $\ell \sim 100$, the value of F_ℓ is about 0.8 for all spectra and rises slowly as ℓ increases. Because the TE transfer function behaves poorly at $\ell \sim 200$ when the spectrum crosses zero, F_ℓ^{TE} is set to the geometric mean $\sqrt{F_\ell^{TT} F_\ell^{EE}}$. The transfer functions for BB and EB are set to F_ℓ^{EE}, and F_ℓ^{TB} is set to F_ℓ^{TE}. The validity of these F_ℓ substitutions has been tested with signal simulations that use different input power spectra. The power spectra of the data, after noise subtraction, are divided by F_ℓ to correct for the effects of timestream filtering.
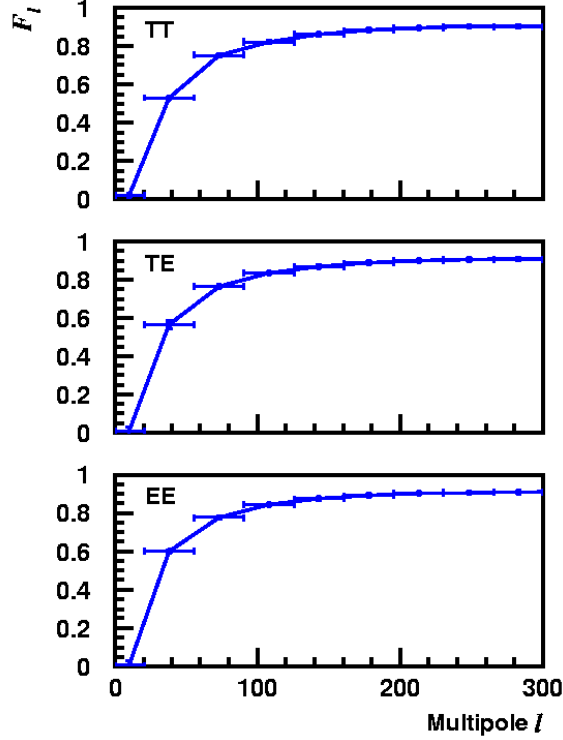
Figure 4.6: Signal-only simulations are used to evaluate the ℓ-space transfer function F_ℓ, shown here for 150 GHz (100 GHz and 100×150 GHz look similar) with third-order polynomial timestream filtering. The TE transfer function is set to the geometric mean $\sqrt{F_\ell^{TT} F_\ell^{EE}}$.

4.4.4 Error bars

After the power spectra have been corrected for noise bias and filtering effects, the final step is assigning error bars. The Fisher matrix for a CMB experiment is

$$\mathcal{F}_{\ell\ell'} = \frac{2\ell+1}{2}\delta_{\ell\ell'}e^{-2\ell^2\sigma^2}\left[C_\ell e^{-\ell^2\sigma^2} + w^{-1}\right]^{-2}, \tag{4.12}$$

where σ is the beam size and w is the instrumental noise. This expression is derived in numerous references, and [12] provides a particularly pedagogical derivation. The C_ℓ errors are equal to the inverse of the square root of the diagonal elements and, after generalizing to cut-sky experiments that observe a sky fraction f_{sky}, are

written as

$$\delta C_\ell = \sqrt{\frac{2}{(2\ell+1)/f_{\text{sky}}}} \left[C_\ell + w^{-1} e^{-\ell^2 \sigma^2} \right]. \tag{4.13}$$

The error consists of two components, one that is proportional to the signal itself (cosmic variance), and another that depends on the instrumental noise and beam function. Given the system noise equivalent temperature, Equation 4.13 provides a rough estimate of the power spectrum error bars. A more precise answer is obtained by examining the variance of signal-plus-noise simulations, which exactly encode time-dependent correlated noise, scan strategy, and sky coverage.

Example simulated signal-plus-noise maps are illustrated in Figure 4.7. If the simulations include a reasonable model of the signal and faithfully reproduce all the properties of the experiment, then the data and simulations should be indistinguishable. Power spectra are calculated for each simulated map using the same $\langle N_\ell \rangle$ and F_ℓ as applied to the data, and the results from 100 simulations are shown in Figure 4.8. The scatter of the simulations determines the error bars.

4.5 Consistency tests

It is important to check that the power spectra are self-consistent and that any signal detected with significance is, in fact, real. We check our power spectra by performing jackknives, a statistical test in which the data are split in two halves and differenced. For BICEP, the split is performed at the mapmaking stage, and the resulting differenced map, which contains little or no signal, should have power spectra that are consistent with zero (or the expected residual signal level) after subtracting noise bias. The interaction of timestream filtering with the details of the data split causes imperfect signal cancellation when forming jackknife maps, but in practice, this residual signal is small.

Jackknife spectra are computed with the same method described in §4.4, using simulated jackknife noise and signal-plus-noise maps to subtract noise bias and assign error bars. The F_ℓ correction does not affect the calculation of the jackknife
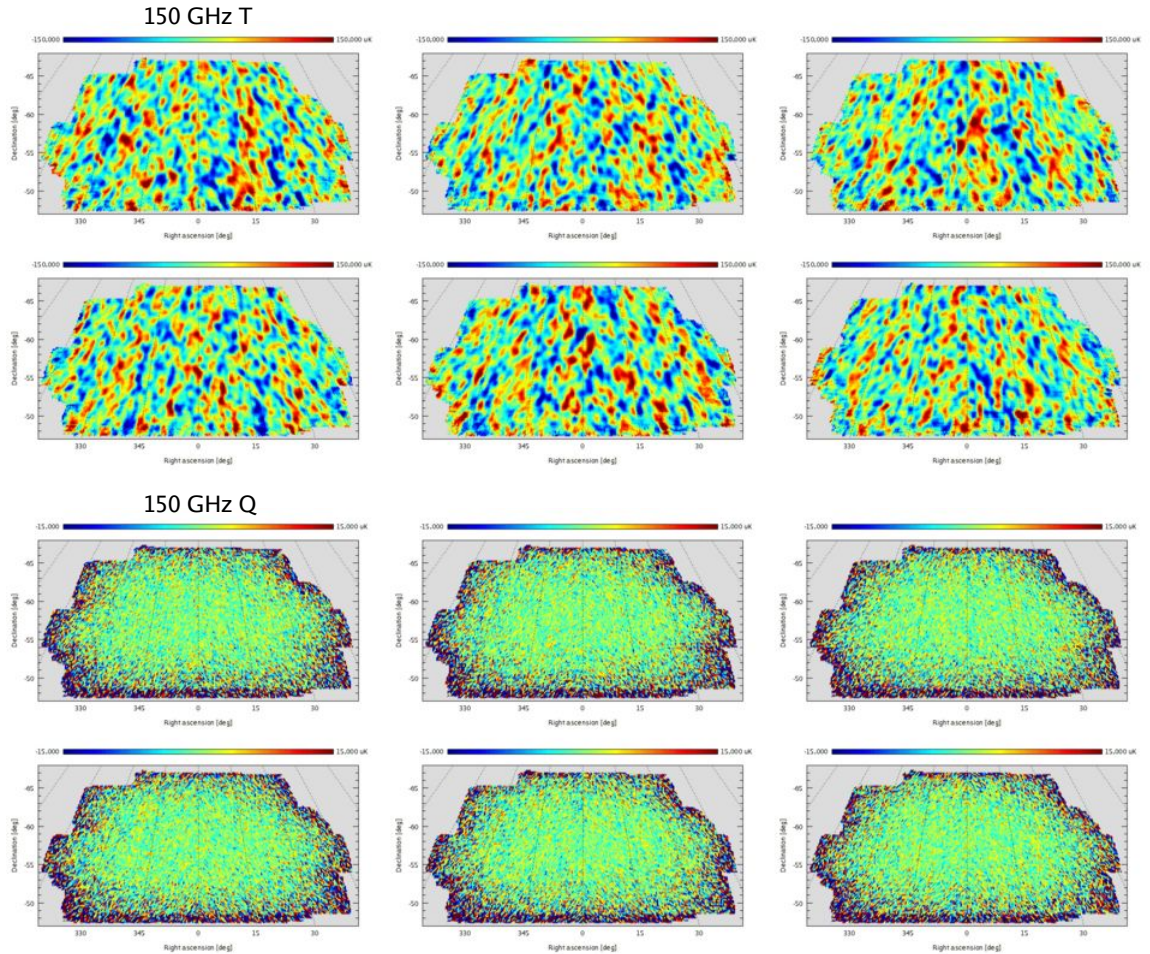
Figure 4.7: Example simulated signal-plus-noise maps at 150 GHz. The upper half shows temperature, and the lower half shows Stokes Q. The color stretches are $\pm 150\,\mu\text{K}$ and $\pm 15\,\mu\text{K}$ for T and Q. (An Easter egg: the lower right T and Q maps are actually data.)

χ^2 values, but it is useful to apply the filter function in order to compare the magnitude of any jackknife failures to the amplitude of the non-jackknife spectra.

Different data splits test different aspects of the instrument's performance. Table 4.1 summarizes the various jackknives performed on BICEP data and the corresponding systematics that each one probes. In the left–right jackknife, the data are split according to the telescope's scan direction in azimuth. Failures generally point to a problem in the detector transfer function deconvolution, or thermal instabilities created at the turnarounds. The elevation coverage jackknife is formed
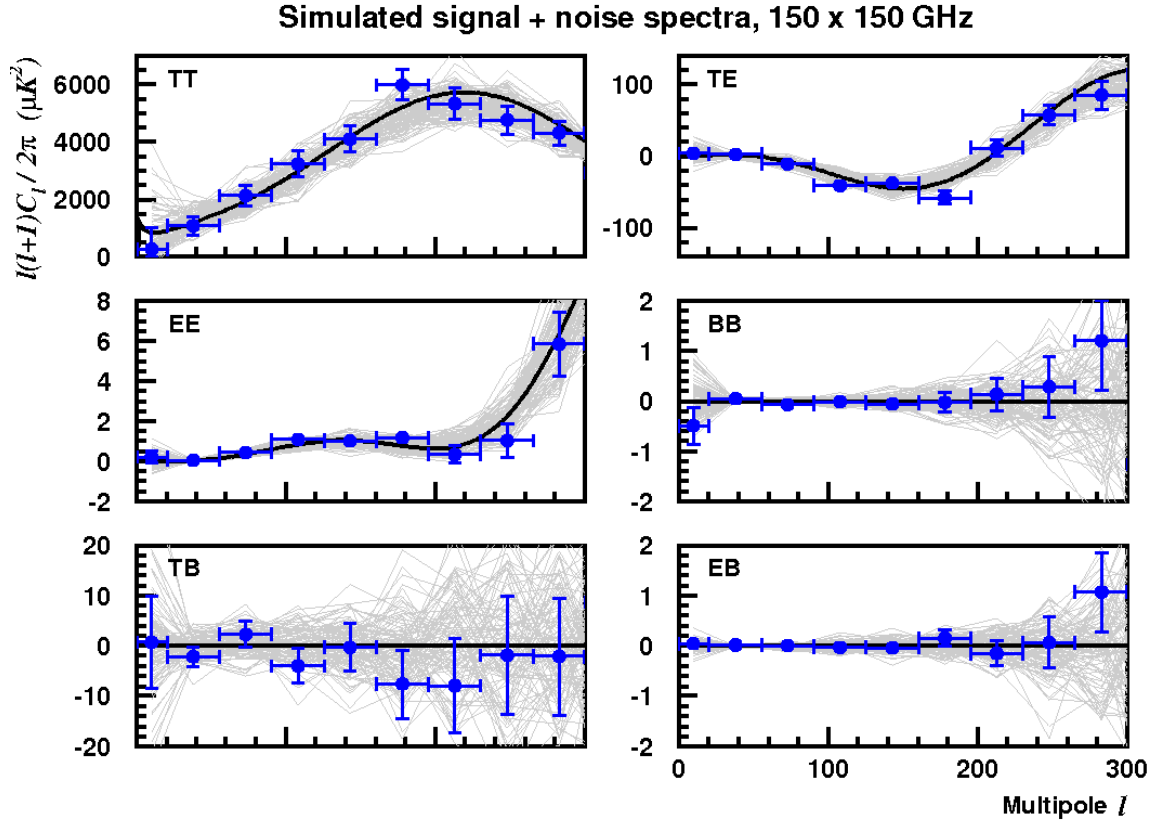
Figure 4.8: Maps from 100 signal-plus-noise simulations (Figure 4.7) at 150 GHz are processed identically to the data to produce power spectra, which are plotted in gray. If the simulations accurately describe the instrument and the signal it sees, then the power spectra of the data should fit within the scatter of the gray lines. The blue points highlight one of the 100 simulations and illustrate the size of the error bars. The black curves correspond to a ΛCDM model.

from the two halves of each 48-hour observing cycle; each half covers the same field starting from a different elevation (see Table 2.2). This jackknife is sensitive to ground-fixed contamination. BICEP observes at four fixed boresight orientation angles, and the boresight angle pair jackknife splits the data into two halves where the boresight angle is $\{-45, 0\}$ or $\{135, 180\}$. This jackknife is arguably the most powerful of the tests listed and is sensitive to many factors, including thermal stability, atmospheric opacity and relative gain mismatches, differential beam pointing, and ground pickup. Essentially, if anything is wrong with the instrument or the analysis, the boresight angle jackknife is likely to fail. The focal plane Q/U

Jackknife type	What it tells you
Left–right	Transfer function errors, thermal instabilities
Elevation coverage	Ground pickup
Boresight angle pairs	Everything (see text)
Focal plane Q/U	Instrumental polarization
8-day temporal split	Weather changes
2006 vs. 2007	Anything different between the two years
100 vs. 150 GHz	Foreground contamination

Table 4.1: BICEP's jackknife tests.

jackknife splits the detectors into two groups according to focal plane orientation (approximately hextants {A, C, E} vs. {B, D, F}, as shown in Figure 2.4) and is a method of probing instrumental polarization effects. In the temporal jackknife, the 8-day observing cycles—48 hours at each of the four boresight angles—are interleaved to form the two halves. This jackknife is sensitive to weather changes but little else, and its main function is to act as the "nice" jackknife that the data should easily pass (if the analysis has been done correctly). The 2006–2007 jackknife simply splits the data into the two observing seasons, and failures reflect any changes made to the instrument between the two years. In particular, the focal plane thermal architecture was improved for the 2007 season, and the temperature control scheme was changed. In the 100 vs. 150 GHz jackknife, the data are split into the two frequency bands, and difference is sensitive to Galactic foreground contamination. In addition to the jackknife splits, the spectra themselves are compared with a ΛCDM model and inspected for any significant departures.

Once the jackknife spectra are formed, χ^2 is calculated for each spectrum over the ℓ bins of interest. The criteria for jackknife success or failure are based on the probability to exceed (PTE) the χ^2 value, which can be calculated either from the theoretical or simulated χ^2 distribution. Jackknife victory is declared when (1) none of the PTEs are abnormally high or low, given the number of χ^2 tests performed, and (2) the PTEs are uniformly distributed between zero and one.

In the BICEP data set, the TT, TE, and TB jackknives often display significant failures, which are likely caused by inaccurate modeling and subtraction of

atmospheric noise. We are currently investigating these failures, which are still unresolved at this point in time. Jackknife failures in the EE, BB, and EB spectra are of greater concern because polarization is the main science goal of BICEP. The traditional approach to solving jackknife failures begins by aggressively cutting data until the remaining set passes all tests. The type of data cuts provide insight on the root causes of jackknife failures, and the analysis techniques are then refined in order to address those issues.

4.6 Thermal noise

The analysis of the 2006 and 2007 data set is approaching completion, and we are currently chasing down the last few jackknife failures before performing a combined analysis of both frequency bands. We have found that the dominant source of jackknife failures is thermal fluctuations on the focal plane that leak into the optical signal, which, if uncorrected, produce visible large-scale structures in the polarization maps (particularly 100 GHz U).

To illustrate the thermal fluctuations, Figure 4.9 shows maps of a thermistor located closest to the heat straps, which are the most probable source of the noise. A third-order polynomial has been subtracted from each of the scans, and most of the remaining power appears as a fourth-order polynomial, the lowest unfiltered mode. The features in the maps vary considerably with boresight angle and observation year, suggesting a microphonic origin for the noise. This particular thermistor exhibits the strongest thermal fluctuations, and thermistors located farther from the heat straps show similar structure, although at a smaller amplitude. Of the four boresight angles used for CMB observations, $0°$ produces the worst thermal instabilities, while $315°$ is the cleanest. The other two angles show comparable amounts of thermal noise at a level between that of $0°$ and $315°$.

Figure 4.10 shows maps of a differenced bolometer pair that is particularly susceptible to thermal noise. The large-scale fourth-order polynomial structure is visible in the optical data, and the sign tracks the thermistor between different bore-
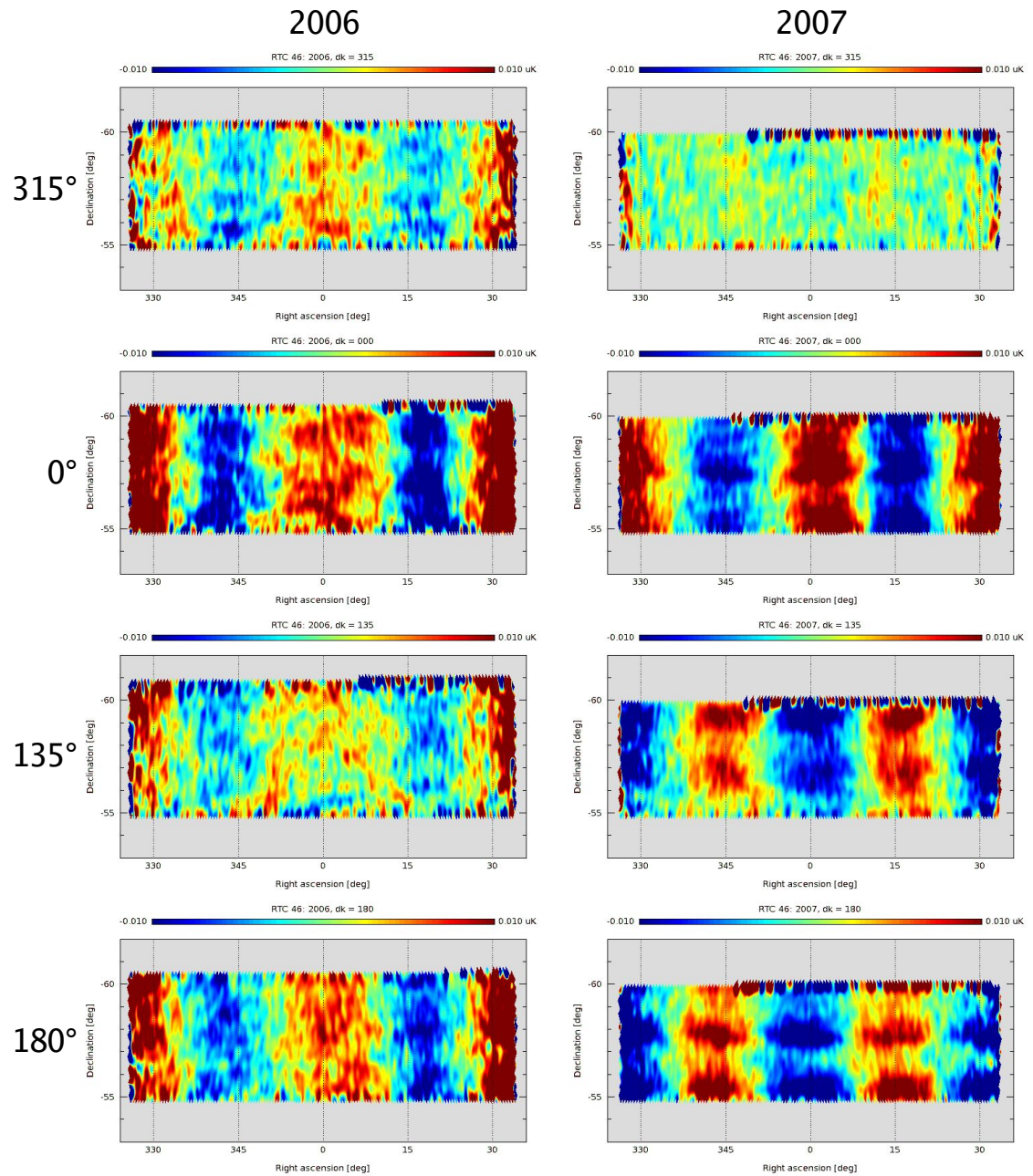
Figure 4.9: Thermistor timestreams are binned in boresight coordinates to produce these maps, which are separated by observation year (2006, 2007) and boresight angle (315°, 0°, 135°, 180°). Thermal instabilities in the focal plane vary greatly between the eight data subsets. The color stretch is ± 0.01 μK.
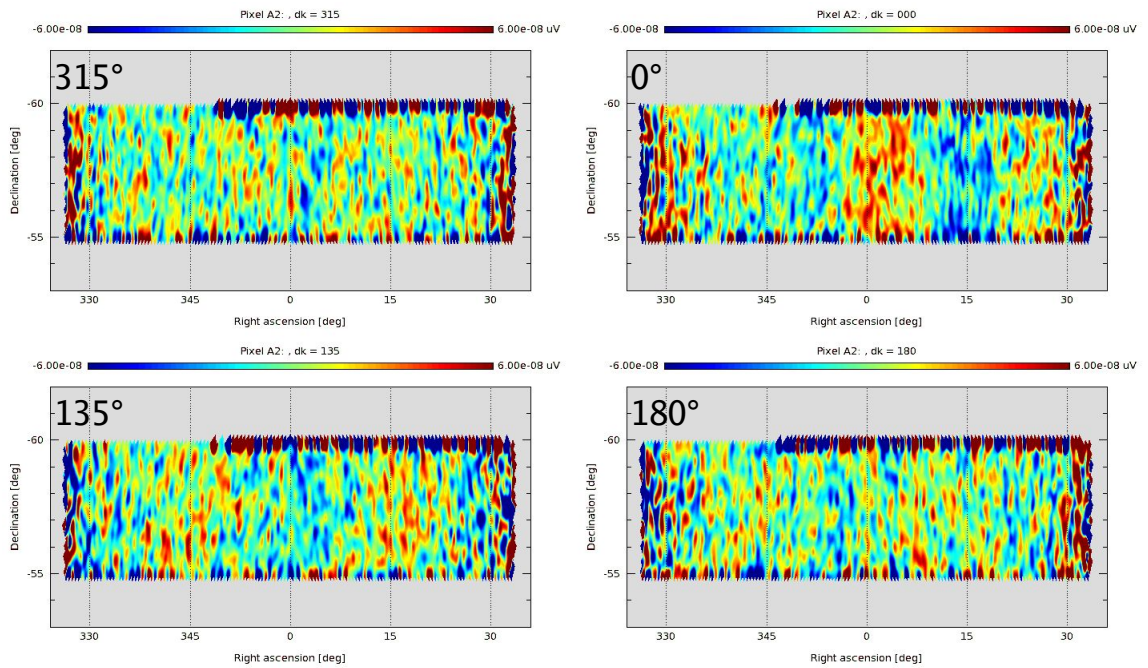
Figure 4.10: A PSB pair (pixel A2) is differenced and binned in boresight coordinates. The maps are split by boresight angle, and only 2007 data is included in this example. The large-scale structure visible in the thermistor maps (Figure 4.9) leaks into the optical signal. Note that the sign of the modulation tracks the thermistor signal and changes between 0° and 135°.

sight angles (for example, compare $0°$ and $135°$). The amount of thermal noise contamination for each bolometer pair can be assessed by cross-correlating their difference maps with the thermistor maps, separated by boresight angle and observation year. The results show that thermal contamination in the bolometer data is worst at a boresight angle of $0°$, and the 100 GHz channels appear to be affected more than the 150 GHz channels. We are currently working on confirming these results with independent measurement techniques, such as examining bolometer timestream responses to heat pulses.

There are several different ways to attack the thermal noise problem in data analysis. Perhaps the most obvious solution is decorrelating the thermistor timestreams from the bolometer data, but this method has been unsuccessful for a number of reasons. We have observed significant temperature gradients across the focal plane, which is made of aluminum and has sub-optimal thermal conductivity, and the thermistors are located only at the perimeter. Therefore, we have poor knowledge of the exact thermal conditions in the central region of the focal plane, and the attempts at decorrelating thermistor timestreams have failed so far.

Because the thermal noise appears primarily at low frequencies corresponding to $\ell \sim 40$, a brute-force solution is increasing the polynomial filtering to higher order. Applying a fifth-order polynomial filter successfully removes the spurious large-scale power in the polarization maps and significantly reduces the number of jackknife failures, but it does not solve all of the jackknife problems. A seventh-order polynomial shows marginal improvement over fifth-order, but it also cuts uncomfortably far into the signal band.

Another approach to removing thermal noise relies on the measured cross-correlation amplitude between bolometer difference and thermistor maps. Based on this amplitude, we can exclude bolometer pairs for each boresight angle and observation year if the level of thermal contamination is above a certain threshold. This data cut has been the most successful solution to jackknife failures so far, but, once again, it does not solve all of the problems.

We are currently investigating the effectiveness of azimuth-fixed subtraction

(§2.10.1) at removing thermal noise contamination. The thermal fluctuations appear to be mostly scan-synchronous and are therefore cleanly subtracted with the template removal technique. A careful study of the resulting spectra and jack-knives is still in progress, but we are cautiously optimistic that a combination of azimuth-fixed subtraction and channel cuts will eliminate the last few remaining jackknife failures.

Chapter 5

Results from BICEP

Preliminary temperature and polarization maps and spectra from BICEP's first two observing seasons are presented in this chapter. The analysis is in its final stages, although we are still refining the details of data cuts and filtering. The two frequency bands are treated separately here, and a combined analysis of the data is in progress.

5.1 Temperature and polarization maps

The BICEP maps of CMB temperature and Stokes Q and U parameters, processed using the techniques described in §4.3, are shown in Figures 5.1 and 5.2. The resolution of the 100 GHz and 150 GHz maps is about 0.9° and 0.6°, respectively, and the pixellization is 0.229° in both cases (corresponding to a `Healpix` nside value of 256). In the central part of the maps, the integration time exceeds 5×10^5 detector–seconds per square degree, and the scan strategy smoothly apodizes the outer edges of the observed region. The rms noise per square degree, measured from Q and U jackknife maps, is 0.78 μK and 0.62 μK for 100 GHz and 150 GHz, respectively, in the central region. The temperature anisotropies are measured with high signal-to-noise and agree well between the two frequencies, while the Q and U maps look almost like white noise. (The 150 GHz Q and U maps, smoothed to 1° resolution, show slight hints of resolved structure.)

Data from both frequencies are combined to form the temperature, E, and B
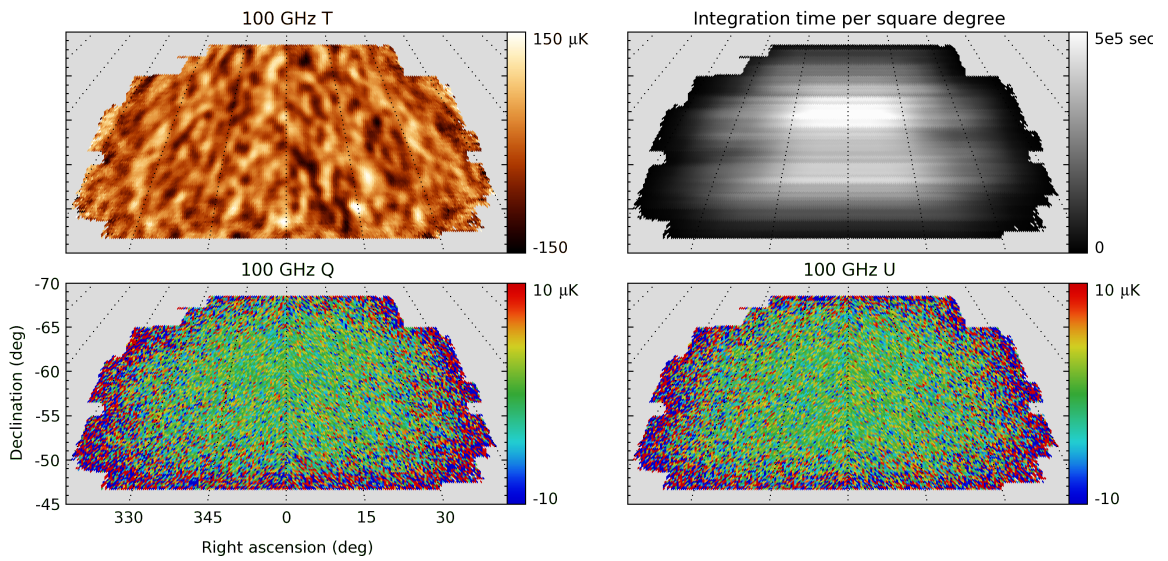
Figure 5.1: BICEP 100-GHz T, Q, U, and coverage maps. The resolution is about 0.9°, and the noise per square degree in the central region is 0.78 μK.
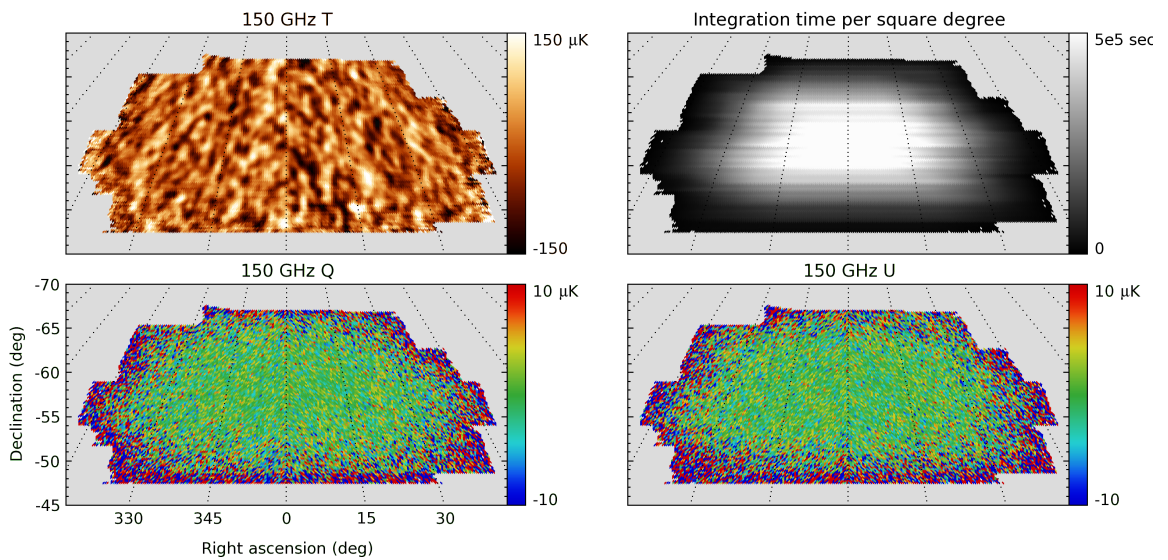

Figure 5.2: BICEP 150-GHz T, Q, U, and coverage maps. The resolution is about 0.6°, and the noise per square degree in the central region is 0.62 μK.
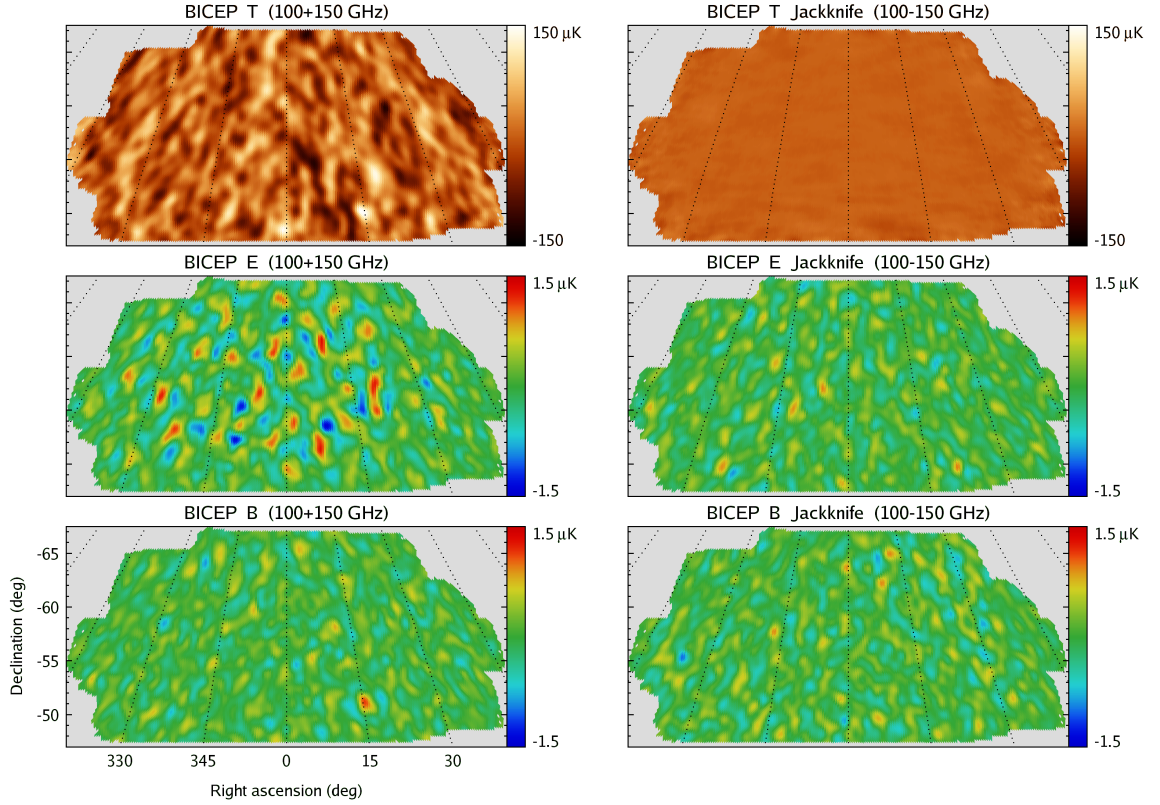
Figure 5.3: Data from BICEP's 100-GHz and 150-GHz channels are combined to form temperature, E, and B signal and jackknife maps. The temperature anisotropies are measured with high signal-to-noise, and the E signal map shows resolved degree-scale structure. The B signal map and the E and B jackknife maps are all consistent with noise.

maps shown in Figure 5.3. The high signal-to-noise of the temperature measurement is demonstrated by the lack of structure in the jackknife map. The faint striping, which is caused by residual atmospheric noise, is successfully removed by PSB differencing. To form the E and B maps, the $a_{\ell m}^E$ and $a_{\ell m}^B$ coefficients are computed from the Q and U maps using the `anafast` utility in `Healpix`. The coefficients are then Wiener filtered according to the expected E-mode signal divided by the beam function. Using the `synfast` utility, $a_{\ell m}^{E,B}$ are interpreted as $Y_{\ell m}$ coefficients from which the E and B maps are generated. The E frequency-sum map shows resolved degree-scale structure at the expected amplitude, while the E and B jackknife maps, as well as the B signal map, are consistent with noise. The jackknife
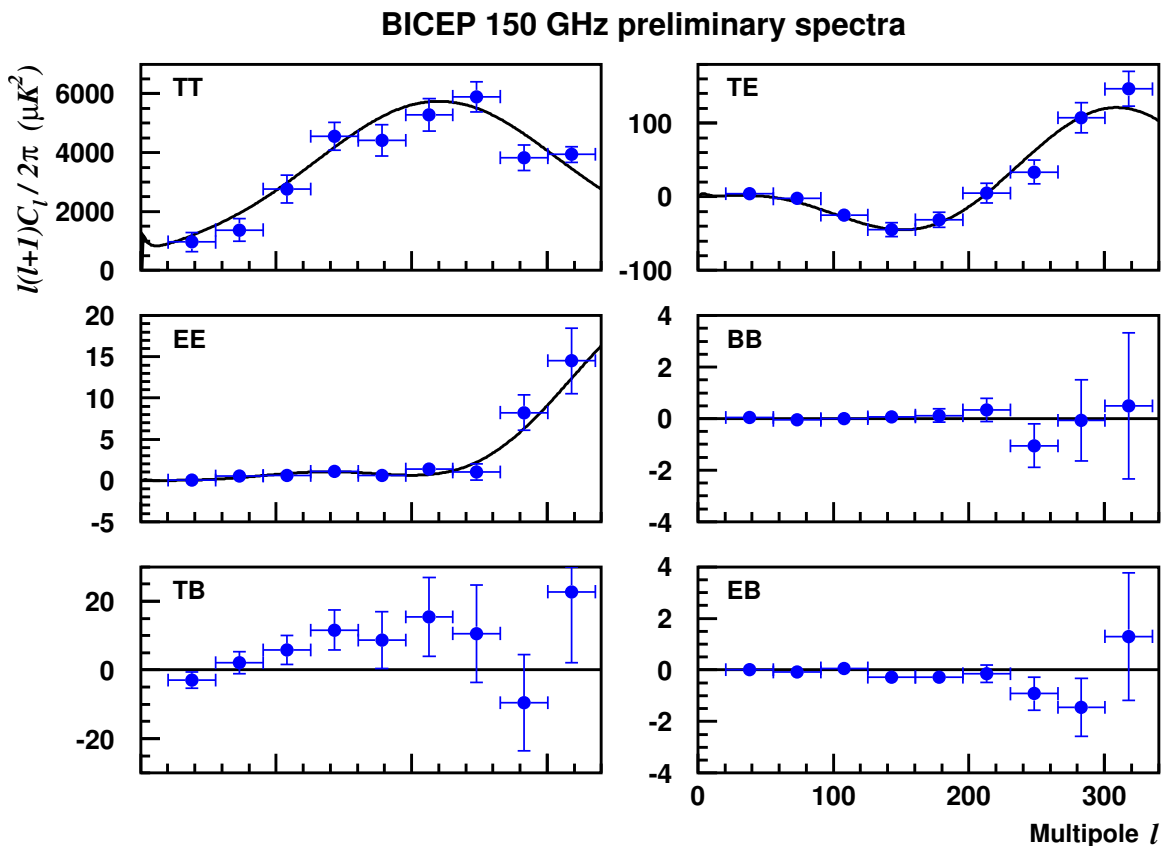
BICEP 150 GHz preliminary spectra

Figure 5.4: Preliminary BICEP 150-GHz power spectra from the 2006 and 2007 data set (blue points). The measurements are consistent with an $r = 0$ ΛCDM model derived from WMAP five-year data, which is plotted in black.

maps, which are formed by differencing the 100 and 150 GHz data, show no evidence of foreground contamination.

5.2 Spectra and jackknives

The spectra presented in this section are preliminary and will change slightly as we refine our analysis techniques. At this point in time, not all the data pass the set of consistency tests described in §4.5, and the main cause of jackknife failures appears to be thermal fluctuations on the focal plane that leak into the bolometer signals. We are currently testing different data cuts and filtering schemes to solve this problem. Thermal noise in the bolometer data can be quantified by cross-correlating
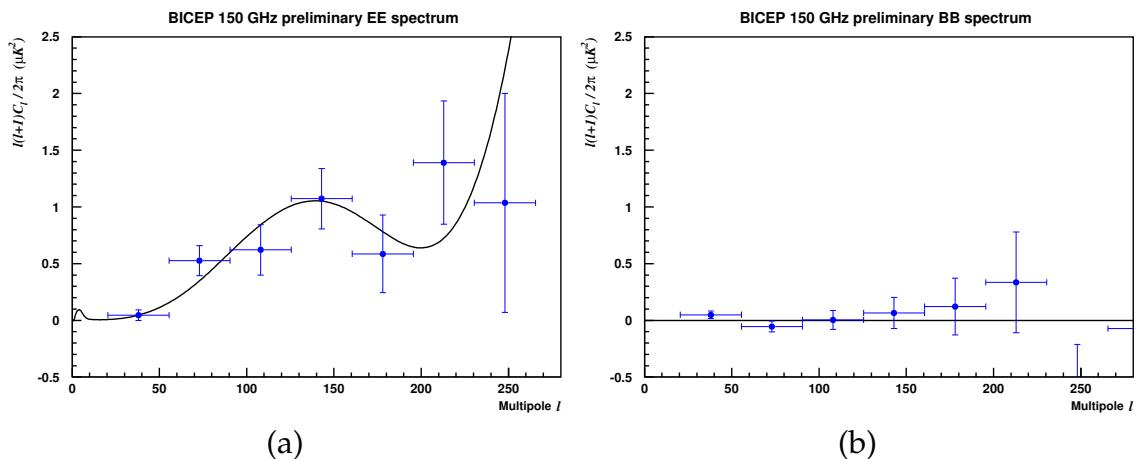
Figure 5.5: Panel (a): the EE spectrum in Figure 5.4 is shown in greater detail to illustrate the high signal-to-noise of BICEP's polarization measurements at degree angular scales. Panel (b): the BB spectrum is consistent with zero. BICEP's sensitivity is maximized around $\ell \sim 100$, the location of the expected B-mode peak.

pair-difference maps with thermistor data, and we have used the cross-correlation amplitudes to form a preliminary data cut that excludes specific channels at each boresight observing angle. Using this data cut, the 150-GHz auto-spectra pass the consistency tests, but the 100-GHz auto-spectra and 100–150-GHz cross-spectra fail in a few cases. Therefore, only the 150-GHz spectra are shown here, and improved analysis of all spectra is an ongoing effort.

Figure 5.4 shows the BICEP 150-GHz spectra plotted with a ΛCDM model derived from WMAP five-year data. The TT, TE, and EE spectra are detected with high significance and are already cosmic-variance limited, and there is no detection of signal in BB, TB, and EB. Overall, the spectra are consistent with the $r = 0$ ΛCDM model, and probabilities to exceed the χ^2 (PTEs) for each spectrum are listed in the first row of Table 5.1. The χ^2 values are calculated from nine bins spanning $21 \leq \ell \leq 335$, and the distributions are taken from 100 signal-plus-noise simulations. BICEP contributes the first high signal-to-noise polarization measurements around $\ell \sim 100$, as illustrated by Figure 5.5, which shows the EE peak at $\ell \sim 140$ in greater detail. A constraint on r from the BB spectrum will depend strongly on the data cuts and filtering, which are still being tuned and will likely

Consistency test	TT	TE	TB	EE	BB	EB
Data vs. ΛCDM	0.28	0.72	0.23	0.62	0.70	0.13
Left–right	0.00	0.91	0.09	0.09	0.88	0.40
Elevation coverage	0.00	0.00	0.00	0.28	0.38	0.46
Boresight angle pairs	0.00	0.03	0.00	0.62	0.03	0.66
8-day temporal split	0.00	0.05	0.03	0.73	0.14	0.27
2006 vs. 2007	0.00	0.00	0.67	0.58	0.30	0.50

Table 5.1: Probabilities to exceed χ^2 in 150-GHz consistency tests. The χ^2 and PTE values are evaluated from nine bins spanning $21 \le \ell \le 335$, and the χ^2 distribution is taken from 100 simulations. (The PTE resolution is therefore 1%.) Apart from the first row, which compares the data with a ΛCDM model, the other tests are jackknives described in Table 4.1. There are significant jackknife failures in the spectra that include temperature information, but the polarization spectra pass the consistency tests.

be conservative for the first data release.

To check the self-consistency of the 150-GHz data, we perform jackknife tests described in Table 4.1[1]. Jackknife spectra are calculated from the difference of two halves of the data set and are expected to be nearly zero (after subtracting noise bias). The interaction of timestream filtering with the data splits causes slightly imperfect signal subtraction when forming jackknife maps, so to account for the expected level of residual signal, the jackknife χ^2 values are calculated by comparing data with signal-only simulations. In practice, the signal-only jackknife spectra are negligible for polarization.

The polarization jackknife spectra are shown in Figure 5.6 and are expressed as band power deviations in Figure 5.7. The EE, BB, and EB spectra pass all the jackknife tests with PTEs that span a range of 0.03 to 0.88 (Table 5.1), the lowest of which corresponds to the BB spectrum in the boresight angle pair jackknife. Although 0.03 is small, the PTEs are expected to follow a uniform distribution, so the probability of one out of the 15 PTE values falling below 0.03 is about 45%. In contrast to the polarization data, the spectra that include temperature information,

---

[1]The focal plane Q/U jackknife has not yet been implemented in the curved-sky analysis pipeline, and the frequency jackknife results are not described here because analysis of the 100-GHz data is still in progress.
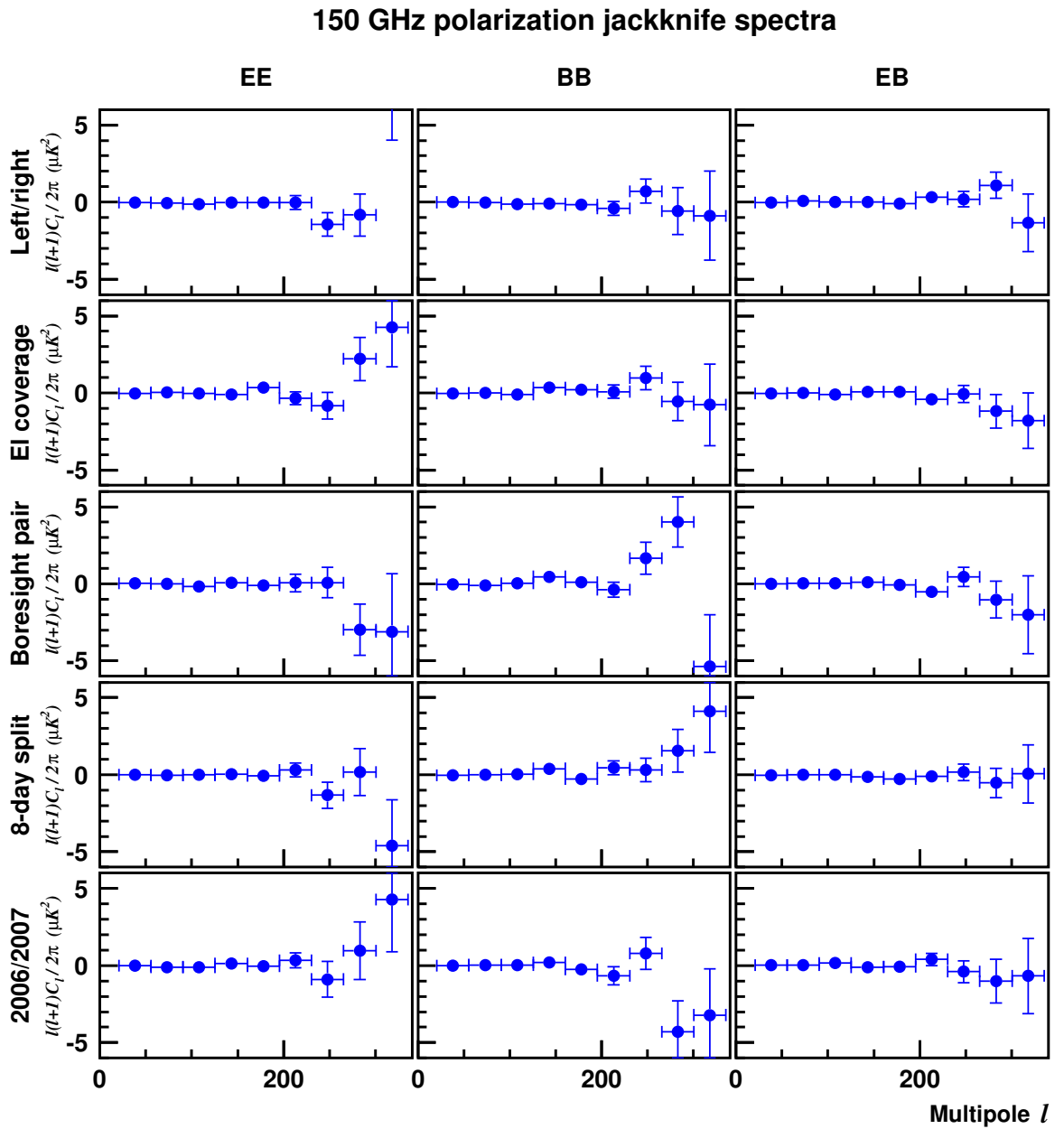
Figure 5.6: 150-GHz polarization jackknife spectra from data splits described in Table 4.1.

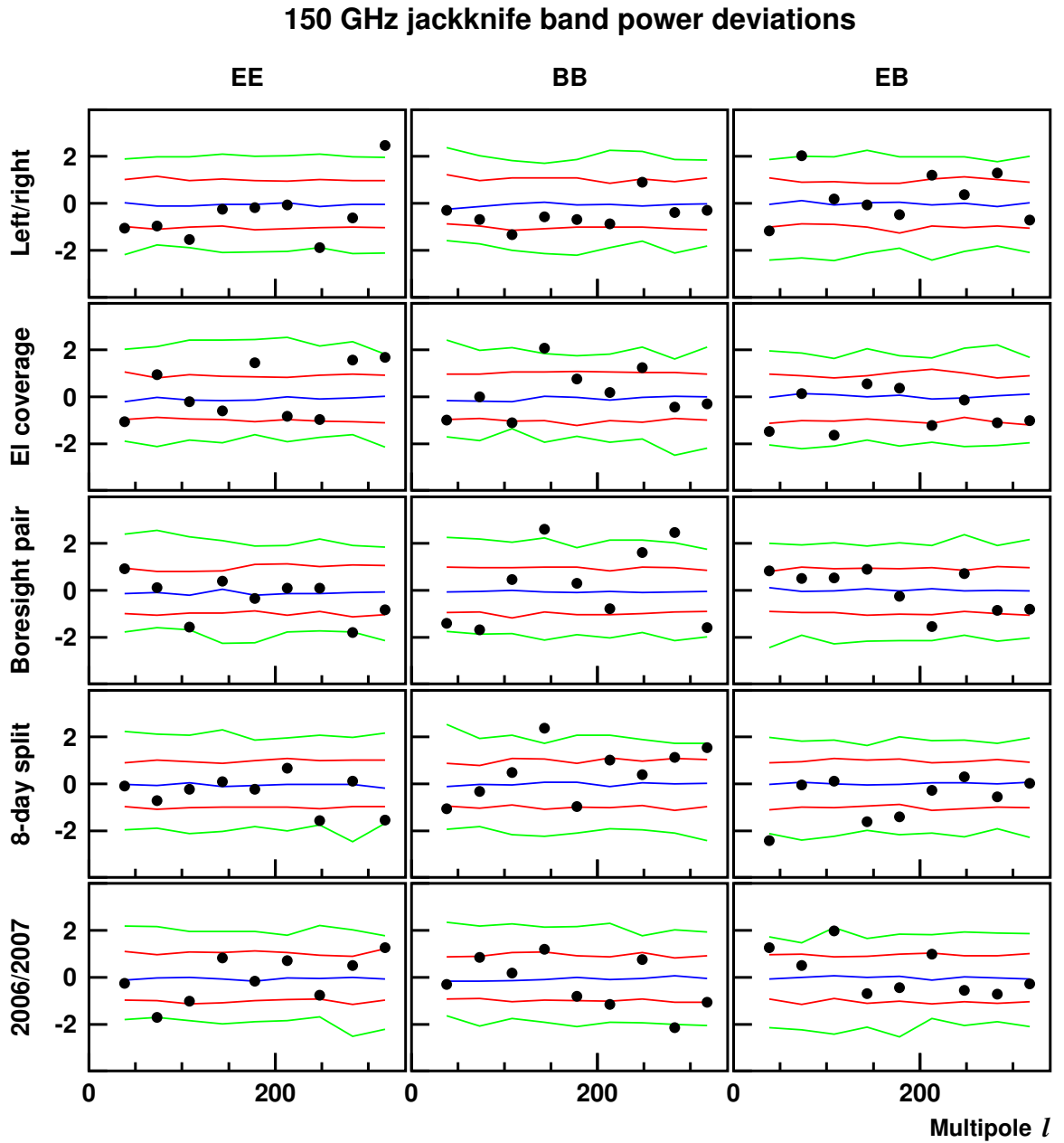**150 GHz jackknife band power deviations**

Figure 5.7: The jackknife spectra in Figure 5.6 are divided by the error bars to obtain band power deviations, which are shown here (black points). The colored lines mark the 2.3%, 15.9%, 50%, 84.1%, and 97.7% points of the distribution of simulated signal-plus-noise band power deviations.
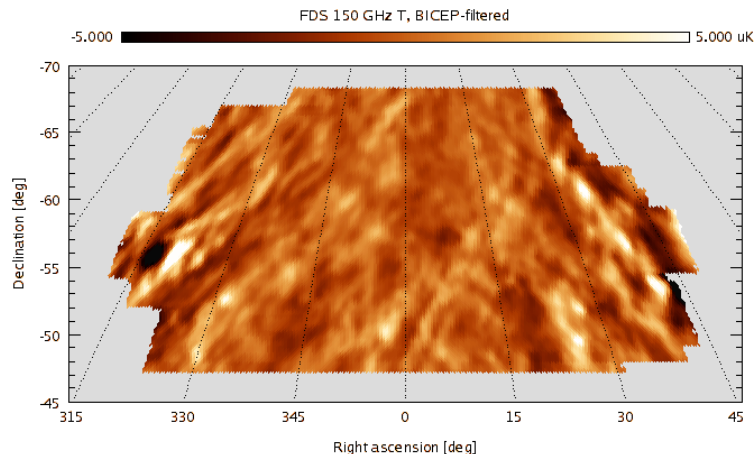
Figure 5.8: Unpolarized 150-GHz dust emission from FDS Model 8, filtered according to BICEP's scan strategy. The temperature power spectrum in this field has an amplitude of about $0.6\ \mu\mathrm{K}^2$ at $\ell \sim 100$.

TT, TE, and TB, display highly statistically significant jackknife failures that we are still investigating.

Two different analysis pipelines have been developed for BICEP, and the results presented here are from a curved-sky analysis, using `Spice` for the power spectrum estimation. The other analysis is performed with a flat sky approximation, using 2D Fourier transforms of maps to calculate the spectra. The code in each pipeline is completely independent of the other, and the only shared data product is the initial set of downsampled, cleaned detector timestreams. We have compared signal and jackknife spectra from both pipelines, and the results are in excellent agreement.

5.3   Foregrounds

There are three potential sources of foreground confusion in BICEP CMB data: thermal dust emission, synchrotron radiation, and extragalactic radio point sources. A complete treatment of foregrounds is still in progress, but some preliminary studies are discussed here.

Dust grains in the Galaxy emit thermal radiation that can be partially polarized due to the alignment of the grains perpendicular to magnetic field lines [39]. Reference [26] presents a detailed full-sky model of the unpolarized thermal dust emission, which is constructed from fits to IRAS, DIRBE, and FIRAS data. The emissivity is modeled as a power law in frequency, and a two-component fit ("FDS Model 8") yields best-fit mean temperatures of $\langle T_1 \rangle = 9.4$ K and $\langle T_2 \rangle = 16.2$ K and spectral indices of $\alpha_1 = 1.67$ and $\alpha_2 = 2.70$. In comparison to dust temperature, little is known about the polarized emission. A study of WMAP data shows that on large scales, the polarized fraction varies between 1% and 6% within the Galactic plane ($|b| < 10°$), and high-latitude dust has a mean fractional polarization of 3.6% [28]. Using these polarization fractions as a rough guideline, we can estimate the expected level of polarized dust emission from FDS Model 8. Figure 5.8 shows the FDS model of dust temperature in BICEP's CMB field, extrapolated to 150 GHz and filtered according to BICEP's scan strategy. The temperature power spectrum of this model has an amplitude of ~ 0.6 μK^2 at $\ell \sim 100$; if we assume that the polarized fraction is about 5%, then the worst-case EE or BB amplitude from dust emission is approximately 1.5×10^{-3} μK^2, which is well below the cosmological BB amplitude for $r = 0.1$. Because the dust temperature has a positive spectral index, we can be optimistic that the polarized emission at 100 GHz is even less.

Synchrotron radiation is emitted by electrons spiraling in Galactic magnetic fields and, like dust emission, is polarized perpendicular to the field lines. The emissivity is also modeled as a power law in frequency, and the average spectral index over the entire sky is measured by WMAP to be -3.2 [28]. The WMAP 23-GHz data are dominated by synchrotron emission and can be extrapolated to 150 GHz with the power law model to determine the expected level of polarized synchrotron for BICEP in the Southern Hole. We find that the polarized synchrotron emission is comparable to that of dust and is therefore unlikely to be a limiting factor in the CMB data analysis.

At degree-scale resolution, the BICEP maps do not show any obvious point source detections, so we rely on the 4.85-GHz Parkes–MIT–NRAO (PMN) sur-

vey [40] to search for point source contamination. The source fluxes at 150 GHz have been measured by ACBAR [41], which has a 5′ FWHM beam and sky coverage that spans most of BICEP's CMB field (with the exception of the region within $|\text{RA}| < 10°$ and $-75° < \text{dec} < -35°$). Table 5.2 lists the 150-GHz fluxes of the PMN sources detected by ACBAR that are located in BICEP's field. For ACBAR, 1 μK = 0.9 mJy at 150 GHz, so the brightest of the sources should be about 30 μK for BICEP. Masking out the 27 sources in Table 5.2 from the BICEP maps has no significant impact on the power spectra and jackknives. Therefore, the preliminary conclusion is that point sources are not a problem, although we plan to perform a more thorough study in the near future.

5.4   Galactic maps

In addition to mapping the CMB temperature and polarization anisotropies, BICEP has spent a significant amount of time observing the Galactic plane (Figure 2.1). Polarization directly in the plane is a tracer of large-scale magnetic fields, and temperature measurements at BICEP frequencies provide a useful cross-check of existing dust models such as FDS and the Planck sky model (PSM). At moderate Galactic latitudes, measurements of diffuse emission are a valuable source of information for upcoming CMB polarization experiments that need to separate Galactic foregrounds from the cosmological signal.

The BICEP 150-GHz Galactic map is illustrated in Figure 5.9 and compared to FDS Model 8 (unpolarized) and PSM [42], which are both filtered identically to the data. In the Galactic plane, BICEP detects polarized emission with high signal-to-noise, and the median polarization fraction is $\sim 2\%$ in the bright regions ($T > 500\ \mu$K). The alignment of the polarization vectors is consistent with large-scale magnetic field lines lying within the plane. The BICEP measurements generally agree well with FDS Model 8, although the model overpredicts the 150-GHz temperature in some regions by a factor of up to 1.5. The Model 8 fit, however, excludes data with Galactic latitude $|b| < 7°$, so this discrepancy is not entirely

Source name	Flux, 4.85 GHz (mJy)	Flux, 150 GHz (mJy)
PMN J0103-6438	395	268
PMN J0144-6421	152	184
PMN J2208-6404	53	136
PMN J0303-6211	1862	429
PMN J0236-6136	406	365
PMN J0257-6112	178	104
PMN J0309-6058	1103	604
PMN J0231-6036	174	105
PMN J0251-6000	433	189
PMN J0050-5738	1338	773
PMN J2309-5703	56	257
PMN J2239-5701	1063	501
PMN J0058-5659	739	514
PMN J2246-5607	618	386
PMN J0253-5441	1193	1277
PMN J0229-5403	242	147
PMN J0223-5347	397	176
PMN J2207-5346	1410	381
PMN J2357-5311	1782	347
PMN J2334-5251	557	432
PMN J0026-5244	40	192
PMN J2336-5236	1588	233
PMN J0133-5159	672	248
PMN J0124-5113	308	335
PMN J0210-5101	3198	1268
PMN J0018-4929	142	178
PMN J2235-4835	1104	1529

Table 5.2: PMN sources detected by ACBAR that are located in the BICEP CMB field. The 150-GHz flux measurements are taken from reference [41], and the brightest source corresponds to about 30 μK for BICEP.
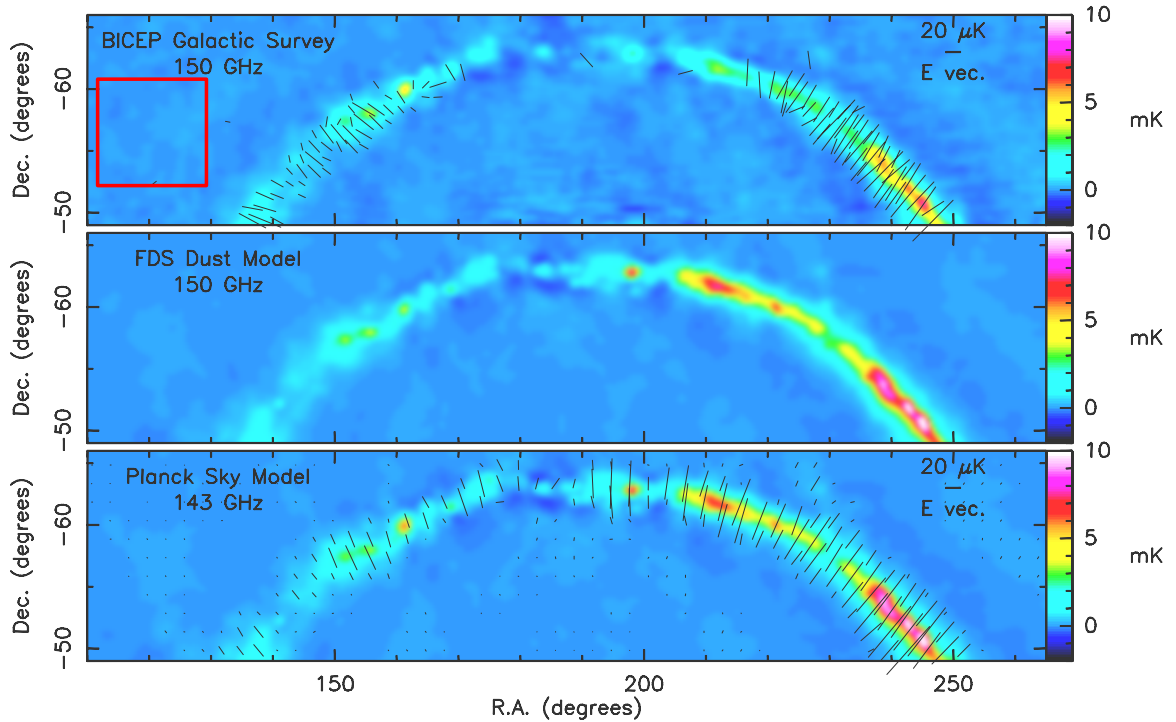
Figure 5.9: BICEP has devoted a significant amount of time to Galactic plane observations, and the 150-GHz map is illustrated in the upper panel. The measured unpolarized emission agrees well with FDS Model 8 (filtered identically to the data), and polarized emission is detected with high signal-to-noise along the plane. The red box marks a region of deep integration where BICEP has detected unpolarized dust emission, and the preliminary constraint on polarization fraction from this region is $< 5\%$. The Planck team has started using BICEP data to verify the Planck sky model [42] (version 1.3 shown here).

surprising. In addition, several compact sources in the plane are not accurately described by the dust model. The PSM is a polarized all-sky model that is partially based on FDS, and the Planck team has started using BICEP data to test the model predictions.

At 100 and 150 GHz, the dominant source of Galactic emission is thermal radiation from dust grains, which increases as a function of frequency. The difference between BICEP's 150 and 100-GHz temperature maps, both smoothed to degree-scale resolution, is compared with FDS Model 8 in Figure 5.10. The CMB fluctuations are removed by differencing the maps, leaving only foreground emission for comparison. The FDS overprediction of 150-GHz temperature is clearly visible
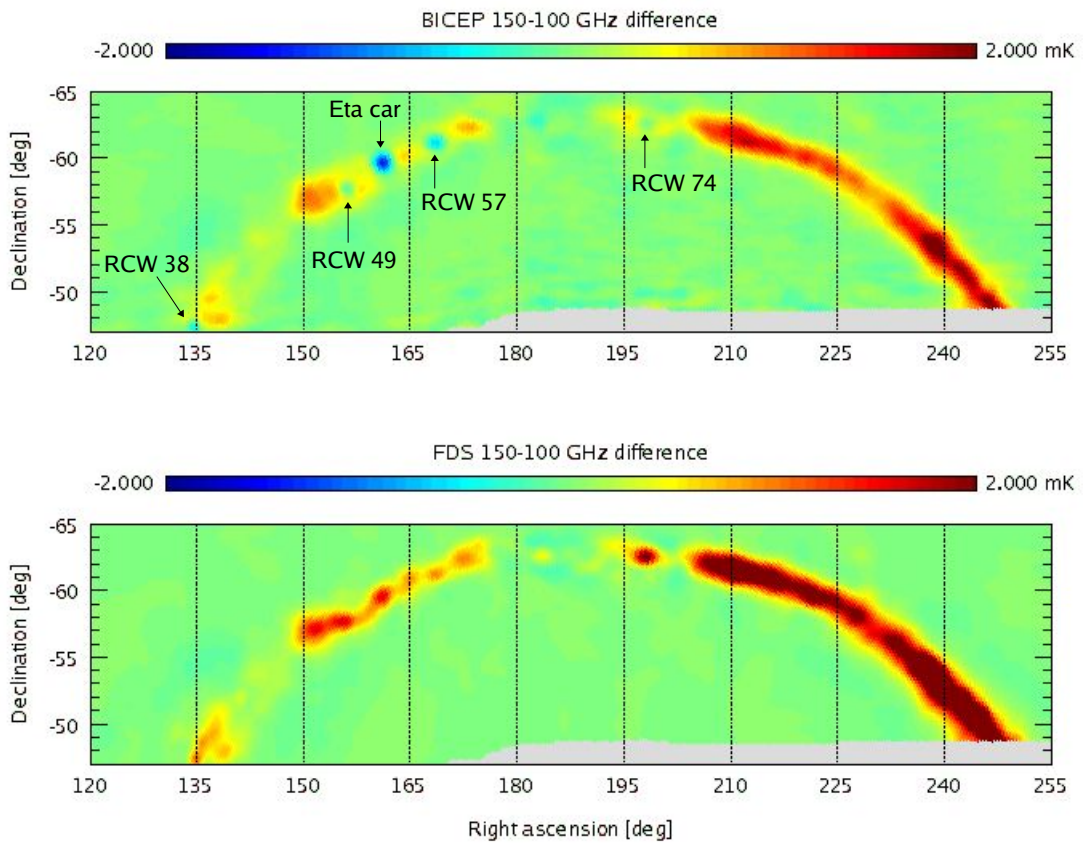
Figure 5.10: The BICEP 150 and 100-GHz Galactic temperature maps are differenced to remove CMB fluctuations, and result is compared to the FDS difference map. FDS overpredicts the temperature at 150-GHz in the Galactic plane, and several compact sources are not accurately described by thermal dust emission.

in the plane, and some of the compact sources also differ between the maps. Eta Carinae is dominated by free-free emission [43] and has a falling spectrum at BI-CEP frequencies, and there are several HII regions with similar behavior (RCW 38, RCW 49, RCW 57, RCW 74).

At mid-range Galactic latitudes (Figure 5.9, red box), BICEP has detected unpolarized dust emission that is too faint to be visible in the maps shown here. After CMB temperature fluctuations are subtracted from the Galactic data, the remaining dust emission in this region has a temperature of $\sim 50\ \mu$K, which agrees well with the FDS Model 8 prediction. The preliminary constraint on dust polarization is $< 5\%$, which is consistent with measurements from WMAP, and further analysis of mid-latitude dust is in progress.

5.5 Conclusions

BICEP has observed the microwave sky from the South Pole since early 2006, and the first two years of data have produced high signal-to-noise measurements of CMB polarization at $\ell \sim 100$. Figure 5.11 compares simulated BICEP spectra with measurements from other experiments, illustrating BICEP's contribution to the EE spectrum at $\ell < 300$. Analysis of the two-year data set is nearly complete, and final spectra will be released shortly. Instrumental systematics have been thoroughly measured and simulated, and BICEP has demonstrated a level of systematics control that is sufficient to probe a tensor-to-scalar ratio of $r = 0.1$.

BICEP will continue observing through the end of 2008 for a total of three seasons of operation. An upgraded receiver, BICEP2, will be installed during the 2009–2010 Austral summer and will observe for two years (2010 and 2011). The BICEP2 receiver has the same small-aperture, two-lens optical design and will use the existing telescope mount, but the focal plane is populated with antenna-coupled transition-edge sensors (TESs) rather than PSBs. In contrast to BICEP1's PSBs, which are coupled to feed horn stacks, these new detector arrays can achieve a much higher packing density, thus increasing the instrument sensitivity. The BI-
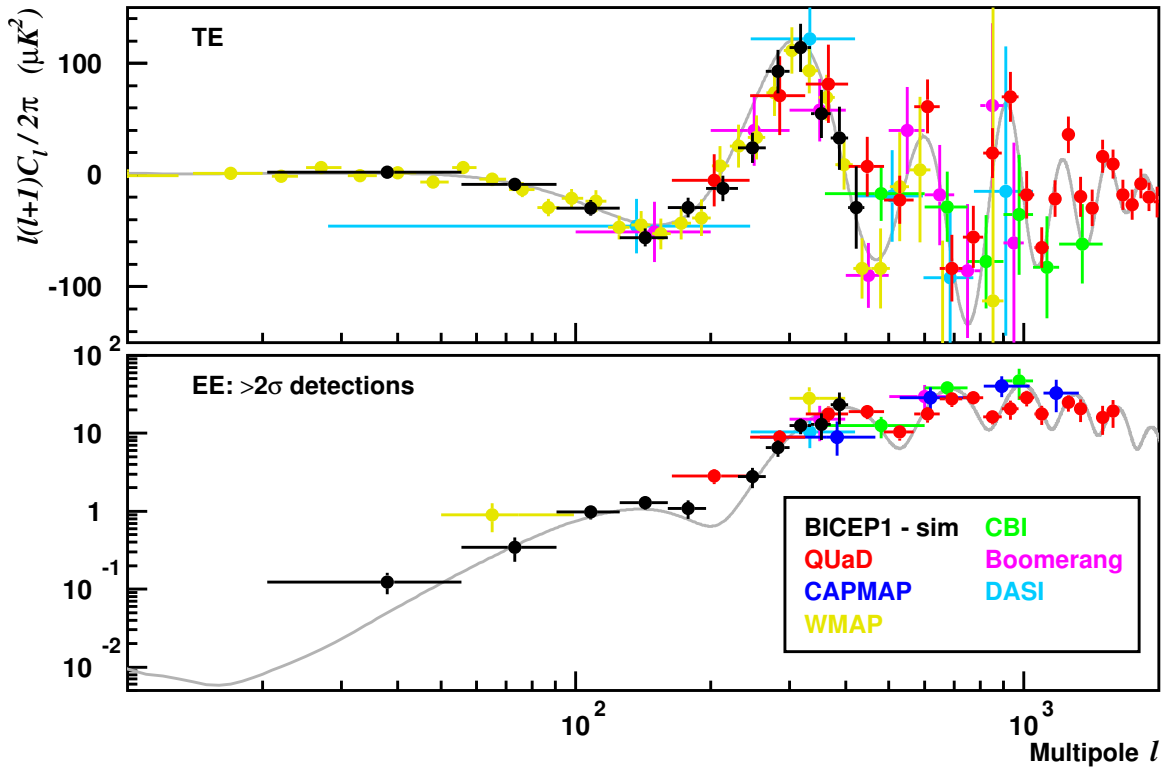
Figure 5.11: Simulated BICEP TE and EE spectra with errors calculated from 100 signal-plus-noise realizations. Most experiments to date have measured the EE spectrum at high ℓ, and BICEP makes a significant contribution at larger angular scales.

CEP2 focal plane will have a total of 256 optically active detector pairs at 150 GHz, with a projected instrument sensitivity of 15 $\mu K_{CMB}\sqrt{s}$. Following the deployment of BICEP2, the frequency coverage and sensitivity will be further expanded with the KECK array, which will ultimately consist of six TES-based receivers observing from the DASI telescope platform. The lessons learned from BICEP1 will help guide the design and operation of BICEP2/KECK as we continue our search for B-mode polarization from inflationary gravitational waves.

Bibliography

[1] M. R. Nolta, J. Dunkley, R. S. Hill, G. Hinshaw, E. Komatsu, D. Larson, L. Page, D. N. Spergel, C. L. Bennett, B. Gold, N. Jarosik, N. Odegard, J. L. Weiland, E. Wollack, M. Halpern, A. Kogut, M. Limon, S. S. Meyer, G. S. Tucker, and E. L. Wright. Five-Year Wilkinson Microwave Anisotropy Probe (WMAP) Observations: Angular Power Spectra. *ArXiv e-prints*, 803, March 2008.

[2] W. C. Jones, P. A. R. Ade, J. J. Bock, J. R. Bond, J. Borrill, A. Boscaleri, P. Cabella, C. R. Contaldi, B. P. Crill, P. de Bernardis, G. De Gasperis, A. de Oliveira-Costa, G. De Troia, G. di Stefano, E. Hivon, A. H. Jaffe, T. S. Kisner, A. E. Lange, C. J. MacTavish, S. Masi, P. D. Mauskopf, A. Melchiorri, T. E. Montroy, P. Natoli, C. B. Netterfield, E. Pascale, F. Piacentini, D. Pogosyan, G. Polenta, S. Prunet, S. Ricciardi, G. Romeo, J. E. Ruhl, P. Santini, M. Tegmark, M. Veneziani, and N. Vittorio. A Measurement of the Angular Power Spectrum of the CMB Temperature Anisotropy from the 2003 Flight of BOOMERANG. *Astrophys. J.* , 647:823–832, August 2006.

[3] A. C. S. Readhead, B. S. Mason, C. R. Contaldi, T. J. Pearson, J. R. Bond, S. T. Myers, S. Padin, J. L. Sievers, J. K. Cartwright, M. C. Shepherd, D. Pogosyan, S. Prunet, P. Altamirano, R. Bustos, L. Bronfman, S. Casassus, W. L. Holzapfel, J. May, U.-L. Pen, S. Torres, and P. S. Udomprasert. Extended Mosaic Observations with the Cosmic Background Imager. *Astrophys. J.* , 609:498–512, July 2004.

[4] C. L. Reichardt, P. A. R. Ade, J. J. Bock, J. R. Bond, J. A. Brevik, C. R. Contaldi, M. D. Daub, J. T. Dempsey, J. H. Goldstein, W. L. Holzapfel, C. L. Kuo, A. E.

Lange, M. Lueker, M. Newcomb, J. B. Peterson, J. Ruhl, M. C. Runyan, and Z. Staniszewski. High Resolution CMB Power Spectrum from the Complete ACBAR Data Set. *ArXiv e-prints*, 801, January 2008.

[5] G. Hinshaw, J. L. Weiland, R. S. Hill, N. Odegard, D. Larson, C. L. Bennett, J. Dunkley, B. Gold, M. R. Greason, N. Jarosik, E. Komatsu, M. R. Nolta, L. Page, D. N. Spergel, E. Wollack, M. Halpern, A. Kogut, M. Limon, S. S. Meyer, G. S. Tucker, and E. L. Wright. Five-Year Wilkinson Microwave Anisotropy Probe (WMAP) Observations: Data Processing, Sky Maps, and Basic Results. *ArXiv e-prints*, 803, March 2008.

[6] J. M. Kovac, E. M. Leitch, C. Pryke, J. E. Carlstrom, N. W. Halverson, and W. L. Holzapfel. Detection of Polarization in the Cosmic Microwave Background using DASI. *Nature*, 420:772–787, 2002.

[7] E. M. Leitch, J. M. Kovac, N. W. Halverson, J. E. Carlstrom, C. Pryke, and M. W. E. Smith. Degree Angular Scale Interferometer 3 Year Cosmic Microwave Background Polarization Results. *Astrophys. J.* , 624:10–20, May 2005.

[8] J. L. Sievers, C. Achermann, J. R. Bond, L. Bronfman, R. Bustos, C. R. Contaldi, C. Dickinson, P. G. Ferreira, M. E. Jones, A. M. Lewis, B. S. Mason, J. May, S. T. Myers, N. Oyarce, S. Padin, T. J. Pearson, M. Pospieszalski, A. C. S. Readhead, R. Reeves, A. C. Taylor, and S. Torres. Implications of the Cosmic Background Imager Polarization Data. *Astrophys. J.* , 660:976–987, May 2007.

[9] T. E. Montroy, P. A. R. Ade, J. J. Bock, J. R. Bond, J. Borrill, A. Boscaleri, P. Cabella, C. R. Contaldi, B. P. Crill, P. de Bernardis, G. De Gasperis, A. de Oliveira-Costa, G. De Troia, G. di Stefano, E. Hivon, A. H. Jaffe, T. S. Kisner, W. C. Jones, A. E. Lange, S. Masi, P. D. Mauskopf, C. J. MacTavish, A. Melchiorri, P. Natoli, C. B. Netterfield, E. Pascale, F. Piacentini, D. Pogosyan, G. Polenta, S. Prunet, S. Ricciardi, G. Romeo, J. E. Ruhl, P. Santini, M. Tegmark, M. Veneziani, and N. Vittorio. A Measurement of the CMB $\langle EE \rangle$ Spectrum from the 2003 Flight of BOOMERANG. *Astrophys. J.* , 647:813–822, August 2006.

[10] QUaD collaboration: C. Pryke, P. Ade, J. Bock, M. Bowden, M. L. Brown, G. Cahill, P. G. Castro, S. Church, T. Culverhouse, R. Friedman, K. Ganga, W. K. Gear, S. Gupta, J. Hinderks, J. Kovac, A. E. Lange, E. Leitch, S. J. Melhuish, Y. Memari, J. A. Murphy, A. Orlando, R. Schwarz, C. O'Sullivan, L. Piccirillo, N. Rajguru, B. Rusholme, A. N. Taylor, K. L. Thompson, A. H. Turner, E. Y. S. Wu, and M. Zemcov. Second and Third Season QUaD CMB Temperature and Polarization Power Spectra. *ArXiv e-prints*, 805, May 2008.

[11] CAPMAP Collaboration: C. Bischoff, L. Hyatt, J. J. McMahon, G. W. Nixon, D. Samtleben, K. M. Smith, K. Vanderlinde, D. Barkats, P. Farese, T. Gaier, J. O. Gundersen, M. M. Hedman, S. T. Staggs, and B. Winstein. New Measurements of Fine-Scale CMB Polarization Power Spectra from CAPMAP at Both 40 and 90 GHz. *ArXiv e-prints*, 802, February 2008.

[12] S. Dodelson. *Modern Cosmology*. Academic Press, San Diego, 2003.

[13] B. Ryden. *Introduction to Cosmology*. Addison Wesley, San Francisco, 2003.

[14] U. Seljak and M. Zaldarriaga. A Line of Sight Approach to Cosmic Microwave Background Anisotropies. *Astrophys. J.* , 469:437–444, 1996.

[15] A. Lewis, A. Challinor, and A. Lasenby. Efficient Computation of CMB Anisotropies in Closed FRW Models. *Astrophys. J.* , 538:473–476, 2000.

[16] M. Hedman. *The Princeton IQU Experiment and Constraints on the Polarization of the Cosmic Microwave Background at 90 GHz*. PhD thesis, Princeton University, 2002.

[17] J. M. Kovac. *Detection of Polarization in the Cosmic Microwave Background Using DASI*. PhD thesis, University of Chicago, 2003.

[18] W. Hu and M. White. A CMB Polarization Primer. *New Astronomy*, 2:323–344, October 1997.

[19] M. Kamionkowski, A. Kosowsky, and A. Stebbins. A Probe of Primordial Gravity Waves and Vorticity. *Phys. Rev. Lett.* , 78:2058–2061, 1997.

[20] U. Seljak and M. Zaldarriaga. Signature of Gravity Waves in the Polarization of the Microwave Background. *Phys. Rev. Lett.* , 78:2054–2057, 1997.

[21] C. J. MacTavish, P. A. R. Ade, J. J. Bock, J. R. Bond, J. Borrill, A. Boscaleri, P. Cabella, C. R. Contaldi, B. P. Crill, P. de Bernardis, G. De Gasperis, A. de Oliveira-Costa, G. De Troia, G. Di Stefano, E. Hivon, A. H. Jaffe, W. C. Jones, T. S. Kisner, A. E. Lange, A. M. Lewis, S. Masi, P. D. Mauskopf, A. Melchiorri, T. E. Montroy, P. Natoli, C. B. Netterfield, E. Pascale, F. Piacentini, D. Pogosyan, G. Polenta, S. Prunet, S. Ricciardi, G. Romeo, J. E. Ruhl, P. Santini, M. Tegmark, M. Veneziani, and N. Vittorio. Cosmological Parameters from the 2003 Flight of BOOMERANG. *Astrophys. J.* , 647:799–812, August 2006.

[22] E. Komatsu, J. Dunkley, M. R. Nolta, C. L. Bennett, B. Gold, G. Hinshaw, N. Jarosik, D. Larson, M. Limon, L. Page, D. N. Spergel, M. Halpern, R. S. Hill, A. Kogut, S. S. Meyer, G. S. Tucker, J. L. Weiland, E. Wollack, and E. L. Wright. Five-Year Wilkinson Microwave Anisotropy Probe (WMAP) Observations: Cosmological Interpretation. *ArXiv e-prints*, 803, March 2008.

[23] W. Hu, M. M. Hedman, and M. Zaldarriaga. Benchmark Parameters for CMB Polarization Experiments. *Phys. Rev. D* , 67(4):043004–1–11, February 2003.

[24] J. R. Bond, A. H. Jaffe, and L. Knox. Radical Compression of Cosmic Microwave Background Data. *Astrophys. J.* , 533:19–37, April 2000.

[25] F. Piacentini, P. A. R. Ade, J. J. Bock, J. R. Bond, J. Borrill, A. Boscaleri, P. Cabella, C. R. Contaldi, B. P. Crill, P. de Bernardis, G. De Gasperis, A. de Oliveira-Costa, G. De Troia, G. di Stefano, E. Hivon, A. H. Jaffe, T. S. Kisner, W. C. Jones, A. E. Lange, S. Masi, P. D. Mauskopf, C. J. MacTavish, A. Melchiorri, T. E. Montroy, P. Natoli, C. B. Netterfield, E. Pascale, D. Pogosyan, G. Polenta, S. Prunet, S. Ricciardi, G. Romeo, J. E. Ruhl, P. San-

tini, M. Tegmark, M. Veneziani, and N. Vittorio. A Measurement of the Polarization-Temperature Angular Cross-Power Spectrum of the Cosmic Microwave Background from the 2003 Flight of BOOMERANG. *Astrophys. J.* , 647:833–839, August 2006.

[26] D. P. Finkbeiner, M. Davis, and D. J. Schlegel. Extrapolation of Galactic Dust Emission at 100 Microns to Cosmic Microwave Background Radiation Frequencies Using FIRAS. *Astrophys. J.* , 524:867–886, 1999.

[27] J. M. Kovac and D. Barkats. CMB from the South Pole: Past, Present, and Future. In J. Dumarchez and J. VTran Thanh Van, editor, *Proceedings of the 6th Rencontres du Vietnam*, Hanoi, Vietnam, May 2007. arXiv:0707.1075 [astro-ph].

[28] A. Kogut, J. Dunkley, C. L. Bennett, O. Doré, B. Gold, M. Halpern, G. Hinshaw, N. Jarosik, E. Komatsu, M. R. Nolta, N. Odegard, L. Page, D. N. Spergel, G. S. Tucker, J. L. Weiland, E. Wollack, and E. L. Wright. Three-Year Wilkinson Microwave Anisotropy Probe (WMAP) Observations: Foreground Polarization. *Astrophys. J.* , 665:355–362, August 2007.

[29] W. C. Jones, R. Bhatia, J. J. Bock, and A. E. Lange. A Polarization Sensitive Bolometric Receiver for Observations of the Cosmic Microwave Background. In T. G. Phillips and J. Zmuidzinas, editor, *Proceedings of the SPIE, Vol. 4855: Millimeter and Submillimeter Detectors for Astronomy*, pages 227–238, Bellingham, Washington, February 2003.

[30] K. W. Yoon. *Design and Deployment of BICEP: A Novel Small-Aperture CMB Polarimeter to test Inflationary Cosmology*. PhD thesis, California Institute of Technology, 2007.

[31] C. W. O'Dell, D. S. Swetz, and P. T. Timbie. Calibration of Millimeter-Wave Polarimeters Using a Thin Dielectric Sheet. *IEEE Trans. Microwave Theory Tech.*, 50(9):2135–2141, September 2002.

[32] T. S. Chu and R. Turrin. Depolarization Properties of Offset Reflector Antennas. *IEEE Trans. Ant. Prop.*, 21(3):339–345, May 1973.

[33] QUaD collaboration: J. Hinderks, P. Ade, J. Bock, M. Bowden, M. L. Brown, G. Cahill, J. E. Carlstrom, P. G. Castro, S. Church, T. Culverhouse, R. Friedman, K. Ganga, W. K. Gear, S. Gupta, J. Harris, V. Haynes, J. Kovac, E. Kirby, A. E. Lange, E. Leitch, O. E. Mallie, S. Melhuish, A. Murphy, A. Orlando, R. Schwarz, C. O' Sullivan, L. Piccirillo, C. Pryke, N. Rajguru, B. Rusholme, A. N. Taylor, K. L. Thompson, C. Tucker, E. Y. S. Wu, and M. Zemcov. QUaD: A High-Resolution Cosmic Microwave Background Polarimeter. *ArXiv e-prints*, 805, May 2008.

[34] N. Ponthieu. Progress on Systematic Effects Estimation (in preparation), 2006.

[35] K. M. Górski, E. Hivon, A. J. Banday, B. D. Wandelt, F. K. Hansen, M. Reinecke, and M. Bartelmann. HEALPix: A Framework for High-Resolution Discretization and Fast Analysis of Data Distributed on the Sphere. *Astrophys. J.* , 622:759–771, April 2005.

[36] W. C. Jones, T. E. Montroy, B. P. Crill, C. R. Contaldi, T. S. Kisner, A. E. Lange, C. J. MacTavish, C. B. Netterfield, and J. E. Ruhl. Instrumental and Analytic Methods for Bolometric Polarimetry. *Astr. & Astroph.* , 470:771–785, August 2007.

[37] E. Hivon, K. M. Górski, C. B. Netterfield, B. P. Crill, S. Prunet, and F. Hansen. MASTER of the Cosmic Microwave Background Anisotropy Power Spectrum: A Fast Method for Statistical Analysis of Large and Complex Cosmic Microwave Background Data Sets. *Astrophys. J.* , 567:2–17, March 2002.

[38] G. Chon, A. Challinor, S. Prunet, E. Hivon, and I. Szapudi. Fast Estimation of Polarization Power Spectra Using Correlation Functions. *Mon. Not. Roy. Astron. Soc.* , 350:914–926, May 2004.

[39] L. J. Davis and J. L. Greenstein. The Polarization of Starlight by Aligned Dust Grains. *Astrophys. J.* , 114:206, September 1951.

[40] A. E. Wright, M. R. Griffith, B. F. Burke, and R. D. Ekers. The Parkes-MIT-NRAO (PMN) Surveys. 2: Source Catalog for the Southern Survey (delta greater than -87.5 deg and less than -37 deg). *Astrophys. J. Suppl.* , 91:111–308, March 1994.

[41] C. L. Reichardt. *A High Resolution Measurement of Temperature Anisotropies in the Cosmic Microwave Background Radiation with the Complete ACBAR Data Set*. PhD thesis, California Institute of Technology, 2008.

[42] Planck Sky Model v1.3 courtesy of the Planck Consortium, in particular G. Rocha, J. Delabrouille, and the Planck Sky Model team.

[43] P. Cox, P. G. Mezger, A. Sievers, F. Najarro, L. Bronfman, E. Kreysa, and G. Haslam. Millimeter emission of η Carinae and its surroundings. *Astr. & Astroph.* , 297:168–174, May 1995.

Appendix A

Coordinate transforms

Thinking on the sphere can be a mind-bending experience. This appendix briefly describes methods for calculating pixel pointing and polarization orientation on the sky, given boresight coordinates and focal plane offsets.

A.1 Rotation matrices

In this example, we solve for $(\mathrm{az}, \mathrm{el})$ of a detector given the following quantities:

- $(\mathrm{az}_0, \mathrm{el}_0, \mathrm{dk}_0)$ = azimuth, elevation, and rotation angle of telescope boresight

- (r, θ) = PSB focal plane coordinates

Let (x, y, z) specify the Cartesian coordinates of the detector. Starting with the boresight at zenith, we obtain

$$x = \sin(r) \cdot \cos(\pi/2 + \theta - \mathrm{dk}_0) \tag{A.1}$$

$$y = -\sin(r) \cdot \sin(\pi/2 + \theta - \mathrm{dk}_0) \tag{A.2}$$

$$z = \cos(r). \tag{A.3}$$

Note that for BICEP, the boresight dk_0 and focal plane θ angles increase in *opposite* directions. The $\pi/2$ offset is needed because θ is referenced to the line perpendicular to the local meridian. Rotate the (x, y, z) coordinates in elevation (about the y

axis, towards $+x$) and then in azimuth:

$$
\begin{pmatrix}
\cos(\mathrm{az}_0) & \sin(\mathrm{az}_0) & 0 \\
-\sin(\mathrm{az}_0) & \cos(\mathrm{az}_0) & 0 \\
0 & 0 & 1
\end{pmatrix}
\begin{pmatrix}
\sin(\mathrm{el}_0) & 0 & \cos(\mathrm{el}_0) \\
0 & 1 & 0 \\
-\cos(\mathrm{el}_0) & 0 & \sin(\mathrm{el}_0)
\end{pmatrix}
\begin{pmatrix}
x \\
y \\
z
\end{pmatrix}. \tag{A.4}
$$

After applying the rotation matrices, the Cartesian coordinates are converted back into azimuth and elevation using

$$
\mathrm{az} = -\mathrm{atan}(y/x) \tag{A.5}
$$

$$
\mathrm{el} = \pi/2 - \mathrm{acos}(z/\sqrt{x^2 + y^2 + z^2}). \tag{A.6}
$$

Given boresight and pixel azimuth/elevation coordinates, the transformations can also be inverted to solve for (r, θ).

A.2   Spherical trigonometry

In this example, we solve for $(\mathrm{RA}, \mathrm{dec})$ of a detector given the following quantities:

- $(\mathrm{RA}_0, \mathrm{dec}_0, \mathrm{dk}_0, P_0)$ = right ascension, declination, rotation angle, and parallactic angle of telescope boresight

- (r, θ) = PSB focal plane coordinates

The detector declination is solved using the spherical law of cosines,

$$
\cos(\pi/2 - \mathrm{dec}) = \cos(r)\cos(\pi/2 - \mathrm{dec}_0) + \sin(r)\sin(\pi/2 - \mathrm{dec}_0)\cos(P_0 + \theta - \mathrm{dk}_0 - \pi/2),
\tag{A.7}
$$

and RA is calculated using the dec angle in a similar expression:

$$
\cos(\mathrm{RA} - \mathrm{RA}_0) = \frac{\cos(r) - \cos(\pi/2 - \mathrm{dec})\cos(\pi/2 - \mathrm{dec}_0)}{\sin(\pi/2 - \mathrm{dec})\sin(\pi/2 - \mathrm{dec}_0)}. \tag{A.8}
$$

The sign of $\cos(\theta - \mathrm{dk}_0 + P_0)$ is used to determine the sign of $\mathrm{RA} - \mathrm{RA}_0$.
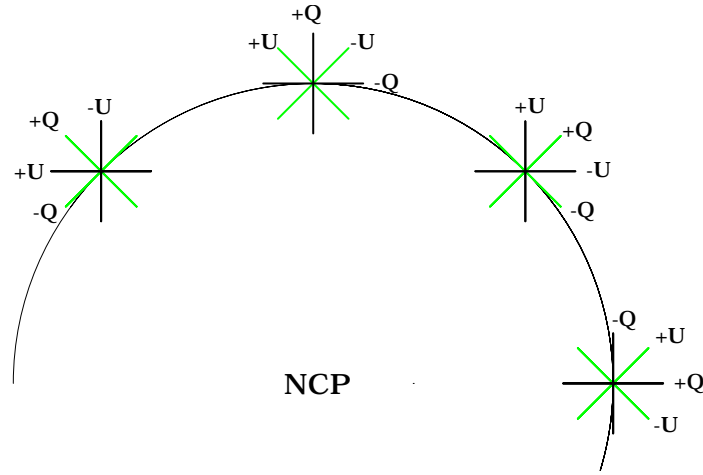
Figure A.1: International Astronomical Union definition of polarization angles on the sky. This figure is taken from reference [16].

A.3 Transforming polarization angles

In focal plane coordinates, the polarization axis of a PSB is specified by an angle χ that is referenced to the radial vector and increases counterclockwise looking at the sky. The polarization angle ψ on the sky is defined using the International Astronomical Union convention (see Figure A.1)—angles are referenced to the meridian, increasing counterclockwise looking at the sky. The angle ψ is equal to the sum of χ and an offset β,

$$\psi = \chi \pm \beta, \tag{A.9}$$

where β is calculated using the expression

$$\cos(\beta) = \frac{\cos(\pi/2 - \xi_0) - \cos(r)\cos(\pi/2 - \xi)}{\sin(r)\sin(\pi/2 - \xi)}. \tag{A.10}$$

Here ξ denotes elevation/declination for horizon/celestial coordinates. The subscript zero denotes telescope boresight coordinates; all other coordinates refer to the detector pointing. The sign of β is determined by the sign of $\cos(\theta - \mathrm{dk}_0)$ for horizon coordinates and $\cos(\theta - \mathrm{dk}_0 + P_0)$ for celestial coordinates.

Appendix B

BICEP pointing model

The BICEP pointing model contains five parameters: azimuth tilt magnitude, azimuth angle of the azimuth tilt, elevation tilt, azimuth zero, and elevation zero. These notes describe the calculations that transform the commanded telescope horizon coordinates into actual horizon coordinates using these five parameters. We start by defining the following variables:

- A_0, E_0, DK_0 = commanded azimuth, elevation, and boresight angle

- A, E, DK = actual azimuth, elevation, and boresight angle

- Θ = magnitude of azimuth tilt (distance along the meridian between zenith and tilted axis)

- Ω = azimuth of tilted azimuth axis

- Θ_E = elevation tilt

B.1 Encoder zeros

The first step is applying the encoder zeros, which is a trivial operation: $A = A_0 - \text{zero}_{\text{az}}$ and $E = E_0 - \text{zero}_{\text{el}}$. That's all.
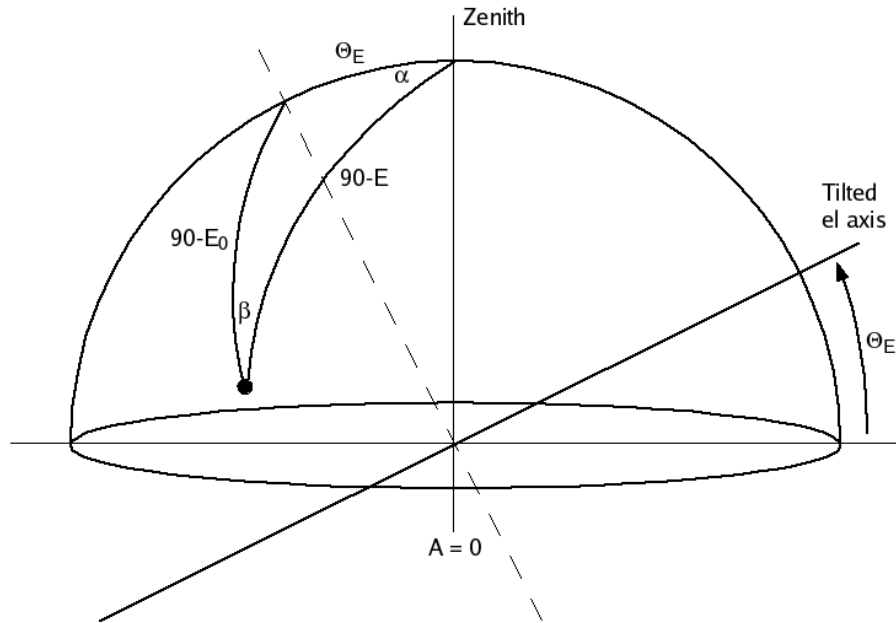
Figure B.1: Ideally, the elevation axis should lie along the east–west line in the azimuth plane. Here, the elevation axis is tilted by an angle Θ_E that increases in the direction shown (clockwise as viewed from from telescope mount out towards azimuth = 0).

B.2 Elevation axis tilt

Figure B.1 illustrates how a tilted elevation axis impacts telescope pointing. We start by solving for E using the law of cosines:

$$\cos(90° - E) = \cos(90° - E_0)\cos\Theta_E + \sin(90° - E_0)\sin\Theta_E\cos(90°)$$

$$\sin E = \sin E_0 \cos\Theta_E. \tag{B.1}$$

The actual azimuth coordinate is offset from the commanded azimuth by an amount $90° - \alpha$. To solve for α, apply the law of cosines again:

$$\cos(90° - E_0) = \cos(90° - E)\cos\Theta_E + \sin(90° - E)\sin\Theta_E\cos\alpha$$

$$\cos\alpha = \tan E \tan\Theta_E. \tag{B.2}$$

Therefore, the actual azimuth coordinate is

$$
\begin{aligned}
A & = A_0 + 90° - \alpha \\
& = A_0 + \sin^{-1}(\tan E \tan \Theta_E).
\end{aligned}
$$
(B.3)

Finally, the boresight orientation angle is offset by β, which we calculate by applying the law of sines:

$$
\sin \beta / \sin \Theta_E = \sin(90°) / \sin(90° - E)
$$
$$
\sin \beta = \sin \Theta_E / \cos E.
$$
(B.4)

The actual boresight orientation angle is thus

$$
DK = DK_0 + \sin^{-1}(\sin \Theta_E / \cos E).
$$
(B.5)

B.3   Azimuth axis tilt

The tilt of the azimuth axis is described by two parameters, a magnitude and azimuth angle, as shown in Figure B.2. The offline fitting code actually outputs x and y tilts instead, which are converted into Θ and Ω with the expressions

$$
\Omega = 0 - 180° - \tan^{-1}\left(\frac{\sin(y \cos x)}{\cos(y \cos x) \sin x}\right)
$$
(B.6)
$$
\Theta = \cos^{-1}[\cos x \cos(y \cos x)].
$$
(B.7)

Once you have Θ and Ω in your pocket, you can proceed to calculate the elevation correction. To stay consistent with notation used by CBI, we'll introduce an angle $\omega = \Omega - A_0 - 90°$. The angle α (see Figure B.2) is related to ω by $\alpha = 90° - \omega$. The spherical law of cosines is used to calculate E:

$$
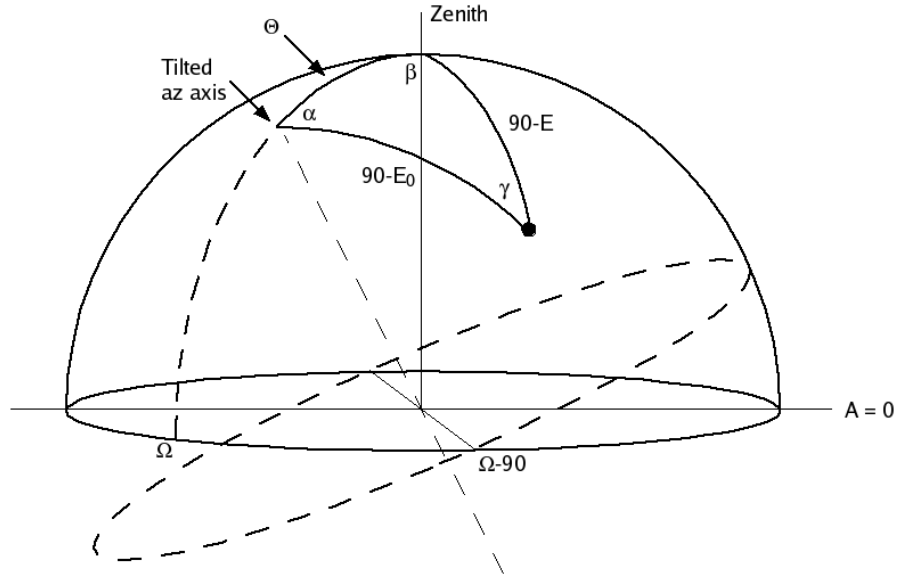\cos(90° - E) = \cos(90° - E_0) \cos \Theta + \sin(90° - E_0) \sin \Theta \cos \alpha
$$

Figure B.2: The tilt of the azimuth axis is described by two parameters: a magnitude Θ and an azimuth angle Ω.

$$\sin E = \sin E_0 \cos \Theta + \cos E_0 \sin \Theta \sin \omega. \tag{B.8}$$

The actual azimuth coordinate is expressed as an offset from Ω: $A = \Omega - \beta$. We obtain two expressions for β. The first one results from the law of cosines,

$$\cos(90° - E_0) = \cos(90° - E) \cos \Theta + \sin(90° - E) \sin \Theta \cos \beta$$
$$\cos \beta = \frac{\sin E_0 - \sin E \cos \Theta}{\cos E \sin \Theta}, \tag{B.9}$$

and the second results from the law of sines:

$$\sin \beta / \sin(90° - E_0) = \sin \alpha / \sin(90° - E)$$
$$\sin \beta = \cos E_0 \sin \alpha / \cos E. \tag{B.10}$$

Dividing the two expressions gives

$$\tan \beta = \frac{\cos E_0 \sin \alpha \sin \Theta}{\sin E_0 - \sin E \cos \Theta}$$

$$= \frac{\cos E_0 \sin \alpha \sin \Theta}{\sin E_0 - \cos \Theta (\sin E_0 \cos \Theta + \cos E_0 \sin \Theta \cos \alpha)}$$

$$= \frac{\cos E_0 \cos \omega}{\sin E_0 \sin \Theta - \cos \Theta \cos E_0 \sin \omega} \tag{B.11}$$

$$A = \Omega - \tan^{-1} \left(\frac{\cos E_0 \cos \omega}{\sin E_0 \sin \Theta - \cos \Theta \cos E_0 \sin \omega} \right). \tag{B.12}$$

The boresight angle offset γ is also calculated using two expressions from the law of cosines and sines. The first equation is

$$\cos \Theta = \cos(90° - E_0) \cos(90° - E) + \sin(90° - E_0) \sin(90° - E) \cos \gamma$$

$$\cos \gamma = \frac{\cos \Theta - \sin E_0 \sin E}{\cos E_0 \cos E}, \tag{B.13}$$

and the second equation is

$$\sin \gamma / \sin \Theta = \sin \alpha / \sin(90° - E)$$

$$\sin \gamma = \sin \Theta \sin \alpha / \cos E. \tag{B.14}$$

Combining the two equations, we obtain

$$\tan \gamma = \frac{\sin \Theta \sin \alpha \cos E_0}{\cos \Theta - \sin E_0 \sin E}$$

$$= \frac{\sin \Theta \sin \alpha \cos E_0}{\cos \Theta - \sin E_0 (\sin E_0 \cos \Theta + \cos E_0 \sin \Theta \sin \omega)}$$

$$= \frac{\sin \Theta \cos \omega}{\cos \Theta \cos E_0 - \sin E_0 \sin \Theta \sin \omega} \tag{B.15}$$

$$DK = DK_0 + \tan^{-1} \left(\frac{\sin \Theta \cos \omega}{\cos \Theta \cos E_0 - \sin E_0 \sin \Theta \sin \omega} \right). \tag{B.16}$$